SURFACE STUDIES OF THIN FILMS WITH A FOCUS ON POTENTIALLY PROTECTIVE FILMS ON VANADIUM

by

DANIEL JOHN ASUNSKIS

B.S., Truman State University, 1999

AN ABSTRACT OF A DISSERTATION

submitted in partial fulfillment of the

requirements for the degree

DOCTOR OF PHILOSOPHY

Department of Chemistry
College of Arts and Sciences

KANSAS STATE UNIVERSITY

Manhattan, Kansas

2005

ABSTRACT

Thin films can be created on the surface of a metal, protecting it from oxidation and corrosion. Phosphate films have historically been a common choice for these corrosion resistant films. In this dissertation, the oxidation of vanadium metal by water and atmosphere is studied. Also, a series of phosphate films on the surface of vanadium metal were created and are studied as potential corrosion resistant films. Lastly, an independent study identifying the oxidation state of copper in a biological sample is carried out. To characterize these thin films, X-ray Photoelectron Spectroscopy (XPS) is employed.

The reaction of vanadium metal with the atmosphere and distilled, de-ionized, water is studied. The core level and valence band results are explored and compared to calculated valence band spectra for some vanadium oxides. The etching of vanadium metal and reaction of the etched metal with a phosphoric acid solution are studied.

Synthesized vanadium phosphate compounds serve as model compounds for the analysis of a phosphate coating created on the surface of vanadium metal by the reaction of vanadium metal with phosphoric acid by a newly developed bench top method. The core level and valence band regions for the compounds and coating are discussed along with cluster and band structure calculations for interpretation. The variation in the coating on vanadium metal by biasing the metal at different potentials during reaction is also studied.

Coatings are also created on vanadium metal using different forms of phosphorus oxy-acid. An analysis of the various coatings is performed by XPS and accompanied by predictive calculations.

In an additional study, the oxidation state of copper in a biological compound is identified. The analysis makes use of satellite features commonly seen in XPS to make the determination. A discussion of the origin of these features and the energy of the shifts is given, along with the results for the other core level XPS regions for the compound.

SURFACE STUDIES OF THIN FILMS WITH A FOCUS ON POTENTIALLY PROTECTIVE FILMS ON VANADIUM

by

DANIEL JOHN ASUNSKIS

B.S., Truman State University, 1999

A DISSERTATION

submitted in partial fulfillment of the

requirements for the degree

DOCTOR OF PHILOSOPHY

Department of Chemistry
College of Arts and Sciences

KANSAS STATE UNIVERSITY

Manhattan, Kansas

2005

APPROVED BY:

Major Professor
Peter M.A. Sherwood

ABSTRACT

Thin films can be created on the surface of a metal, protecting it from oxidation and corrosion. Phosphate films have historically been a common choice for these corrosion resistant films. In this dissertation, the oxidation of vanadium metal by water and atmosphere is studied. Also, a series of phosphate films on the surface of vanadium metal were created and are studied as potential corrosion resistant films. Lastly, an independent study identifying the oxidation state of copper in a biological sample is carried out. To characterize these thin films, X-ray Photoelectron Spectroscopy (XPS) is employed.

The reaction of vanadium metal with the atmosphere and distilled, de-ionized, water is studied. The core level and valence band results are explored and compared to calculated valence band spectra for some vanadium oxides. The etching of vanadium metal and reaction of the etched metal with a phosphoric acid solution are studied.

Synthesized vanadium phosphate compounds serve as model compounds for the analysis of a phosphate coating created on the surface of vanadium metal by the reaction of vanadium metal with phosphoric acid by a newly developed bench top method. The core level and valence band regions for the compounds and coating are discussed along with cluster and band structure calculations for interpretation. The variation in the coating on vanadium metal by biasing the metal at different potentials during reaction is also studied.

Coatings are also created on vanadium metal using different forms of phosphorus oxy-acid. An analysis of the various coatings is performed by XPS and accompanied by predictive calculations.

In an additional study, the oxidation state of copper in a biological compound is identified. The analysis makes use of satellite features commonly seen in XPS to make the determination. A discussion of the origin of these features and the energy of the shifts is given, along with the results for the other core level XPS regions for the compound.

TABLE OF CONTENTS

LIST OF FIGURES

LIST OF TABLES

ACKNOWLEDGEMENTS

I would like to thank my major professor and advisor, Peter Sherwood, for the guidance he has given me. Figures 4.2 and 4.3 are reproduced from his previous work. He also contributed all multiple-scattered wave Xα calculations shown in this dissertation. I also would like to thank the Sherwood research group for help in the laboratory and in analysis. Yuqing Wang was always available whenever I called upon him and for that I am grateful. Thanks to Greg Claycomb for the CuO spectrum shown in Figure 8.3b.

DEDICATION

This work is dedicated to my family. To my mother and father, John and Linda, who are sources of constant support. To my brothers and sister-in-law, Joel, David and Heather, for always allowing me to relax and laugh. Lastly, this is dedicated to my wife, Amy, for the love and support she gave me through this work and she continues to give in all aspects of my life.

Chapter 1

Introduction

The corrosion of metals is a process that has gathered large attention due to the affect it has on our daily lives. Coatings used to make metals more corrosion resistant are an area of major interest. Phosphate conversion coatings are a common industrially used coating for corrosion resistance. The Sherwood group has shown over the last 10 years that thin, oxide-free films can be created on a metal surface, vastly different than the industrial coatings. This dissertation presents the formation of various phosphate coatings on the surface of vanadium metal. These coatings created on the vanadium metal surface are characterized by X-ray Photoelectron Spectroscopy, XPS. An additional study was performed, identifying the oxidation state of copper in a biological sample. The results of this study are also included. The layout of the dissertation is as follows:

Chapter 2 is an introduction to corrosion and to phosphate conversion coatings. The corrosion of metal has been explored from an electrochemical standpoint, using thermodynamics to outline some basic properties of corrosion. The use of coatings, specifically phosphate conversion coatings, to make metals more corrosion resistant is discussed, along with description of some of the uses of phosphate conversion coatings.

Chapter 3 introduces vanadium metal, its oxides, and phosphates. Some of the basic parameters of vanadium and its compounds are discussed. The structure of the oxides is given and an introduction to the use of vanadium phosphates for catalysis is given.

Chapter 4 is an introduction to X-ray Photoelectron Spectroscopy, XPS. The instrumental setup used in an XPS experiment is explained, with a brief description of the parts of the instrument. Next, explanation of the energy scale used in XPS is given, showing how the kinetic energy of an ejected electron relates to the atom it is ejected from. The properties that contribute to the fine structure in XPS are described, such as the spin-orbit splitting of the core regions and the various factors contributing to satellite features. This section also includes a discussion of the analysis of the spectra, specifically the use of curve-fitting to analyze overlapping features and valence band prediction by calculative methods.

Chapter 5 begins the experimental portion of the dissertation. The analysis of vanadium metal in its native state and some oxidizing conditions are explored. The reaction of vanadium metal with the atmosphere and distilled, de-ionized, water is studied. The core level and valence band results are explored and compared to calculated valence band spectra for some vanadium oxides. The etching of vanadium metal and reaction of the etched metal with a phosphoric acid solution are studied.

Chapter 6 is an analysis of three synthesized compounds. These synthesized vanadium phosphate compounds serve as model compounds for analysis of a phosphate coating created on vanadium metal by the reaction of vanadium metal with phosphoric acid by a newly developed bench top method. The core level and valence band regions for the compounds and coating are discussed along with cluster and band structure calculations for interpretation. The variation in the coating on vanadium metal by biasing the metal at different potentials during reaction is also studied.

Chapter 7 examines coatings created on vanadium metal using different forms of phosphorus oxy-acid. The different solutions create different coatings, whose XPS results are discussed. Analysis of the various coatings is performed by predictive calculation methods.

Chapter 8 is an additional study done, where the oxidation state of copper in a biological compound is identified. The analysis makes use of satellite features commonly seen in XPS to make the determination. A discussion of the origin of these features and the energy of the shifts is given, along with the results for the other core level XPS regions for the compound.

Chapter 2
Corrosion and Corrosion Protection

2.1 Introduction

Materials degrade over time. A classical view of the degradation of a material was to separate the types into two major areas, erosion and corrosion. Erosion occurs when a material is worn away by physical contact or wear. Corrosion occurs when the environment around the material causes the material to degrade by reaction.[1] The diminishing of the brake-pads in an automobile can be considered an erosion process, while the holes in a steel bumper formed by rust is an example of corrosion.

Corrosion of materials has been studied very extensively for well over a century. The affects of corrosion are seen all around us in our daily lives and because of this our government spends hundreds of billions of dollars annually for repairing corroded structures, but also for study as to the origin and prevention of these affects.[2] In 1998, the federal government posted a $8.79 trillion gross domestic product (GDP). A report predicted that $276 billion went directly for corrosion related funding. This represents 3.1% of the GDP and this number is inflated to $552 billion (6%) when indirect costs are considered. These gigantic sums of money show the big impact that corrosion has on our lives.

2.2 Types of Corrosion

Corrosion can be broken down into two main areas, chemical and electrochemical corrosion. Chemical corrosion is a thermodynamically driven reaction where no current flow is seen during reaction. In an electrochemical corrosion process an electric current is generated with the flow of electrons from the metal.[1]

Chemical corrosion can be further broken down into to types of corrosion, gaseous and non-electrolytic corrosion. Gaseous corrosion occurs readily at high temperatures, as in many metals there is an increase in the rate of corrosion. Non-electrolytic corrosion occurs when the metal is in the presence of a medium that does not support electrical current flow. Oil is a common cause for this corrosion, as it is generally seen in the oil industry in refineries and transportation devices.

Electrochemical corrosion defines most of the corrosion occurring around us today. The loss of electrons by the metal is facilitated by the ionic nature of the medium the metal is emersed in. This process of corrosion is defined from an electrochemistry standpoint.

2.3 Chemistry of Electrochemical Corrosion of Metals

The electrochemical corrosion of metals can be considered a series of localized reactions occurring at the metal's surface. Iron is a common choice for study and example as it is a commonly used metal. Iron metal in the presence of water, at pH 7, can be considered an electrochemical reaction containing anodic and cathodic reactions. An anodic reaction is where oxidation occurs and for the case of iron, the reaction at the metal surface can be defined as equation 2.1.[1]

$$Fe_{(s)} \rightarrow Fe^{2+} + 2e^{-} \qquad (2.1)$$

The cathodic reaction, where reduction occurs, is the electrons that are being released reacting with species in the environment. Equation 2.2 and 2.3 are cathodic reactions, showing the oxidation of the metal by acid or dissolved oxygen in water.

$$H^{+} + e^{-} \rightarrow \tfrac{1}{2}H_2 \qquad (2.2)$$

$$4H^{+} + O_{2(g)} + 2e\text{-} \rightarrow 2H_2O \qquad (2.3)$$

The corrosion of metallic iron in water can then be defined as a combination of equations 1 and 3.

$$Fe_{(s)} + 4H^{+} + O_2 \rightarrow Fe^{2+} + 2H_2O \qquad (2.4)$$

The cell potential, E, for equation 2.4 can be calculated using the standard reduction potentials. The potential for equation 2.1 is -0.44V and after adjusting for a pH of 7 using the Nernst equation, the potential for equation 2.2 is 0.82V. To look at the electrochemical corrosion of a metal thermodynamically, the Gibbs energy ($\Delta_r G$) for the reaction can be calculated from the cell potential found in Equation 2.4. To do this, Equation 2.5 is used.

$$\Delta_r G = -nfE \qquad (2.5)$$

Faraday's constant, f, is 96.485 kC/mol. and n is the number of electrons transferred in the redox reaction, being 2 for Equation 2.4. The cell potential is 1.26 V giving a $\Delta_r G$ of -243 kCal/mol. Similarly, the corrosion of iron at pH=0 by the reduction of H^+ is expressed by the redox reaction, Equation 2.6.

$$Fe_{(m)} + 2H^+ \rightarrow Fe^{2+} + H_2 \qquad (2.6)$$

It has a cell potential, E, of 0.44 V and a $\Delta_r G$ of -84.9 kCal/mol. The values found for the reactions in Equation 2.4 and 2.5 are negative, predicting that iron should corrode readily in water at these conditions. Iron is considered an active metal, meaning that the reaction of the metal is exothermic toward the reduction of hydrogen ion and the reduction of dissolved oxygen. Other metals called noble metals have a positive Gibbs free energy value, such as gold and platinum. Semi-noble metals have a positive Gibbs energy change with respect to the oxidation by the hydrogen ion, but a negative value with respect to the oxygen, such as silver and copper. These values are representative of specific states and any changes in temperature, pH, or dissolved gas can significantly alter the reactions and the calculated values.

2.4 Passivation of Metals

When examining the free energy changes as a metal becomes a solvated ion aluminum has a higher potential to corrode than iron as the cell potential is higher for an

aluminum corrosion process than an iron corrosion process. This is the case for the initial corrosion, but the aluminum forms an oxide layer on the surface, which is generally insoluble, and acts as a protective layer stopping further oxidation. In iron the reaction products are much more porous and allow for further attack of the metal below. The calculated potentials do not take into account any formed products. The film formed on the metal is another property that can affect the corrosion of a metal.

The oxide layer that forms naturally on aluminum is an example of a metal that is self-passivating. Passive metals are predicted thermodynamically to be active metals that would corrode, but in reality they actually exhibit slow corrosion rates. The term "passive" was first used by Schonbein over 170 years ago to describe the corrosion resistance of iron after it was treated with a concentrated nitric acid solution.[1] The concentrated solution forces the iron surface to oxize forming a stable state.

An alternative to passivating metal is the use of an inhibitive coating, known as a conversion coating. This is done by replacing the naturally forming surface layer with a new more corrosion resistant layer. Many types of conversion coatings exist and a phosphate conversion coating is one type of these coatings.

2.5 Phosphate Conversion Coatings

The use of phosphate coatings, or phosphatizing, has been around for well over one hundred years. These coatings have been primarily used in industry as a primer for metals to adhere paints, but their ability to act as a corrosion inhibitor is an added benefit.[3] More recently, phosphate coatings have made their way into another application,

biomedical implantation. Here, the coatings are used to mimic materials found in the human body in order to promote biocompatibility and bioadhesion.

2.5.1 Industrial Phosphate Coatings

Conversion coatings can roughly be defined as changing the native surface of a metal or alloy into another surface to promote adhesion or corrosion inhibition. Phosphate coating is a well-known conversion coating. A wide variety of coatings exist today, but the exact components of the coating mixtures vary from company to company for proprietary reasons. Industrial phosphate coatings focus on the use of zinc, manganese, iron and calcium phosphates. They have proven to effectively coat iron, steel, aluminum and their various alloys. A particular phosphate coating is chosen to meet the needs of the application. One characteristic of these coatings that is monitored is the porosity of the metal phosphate film. Increasing the porosity will help in adhesion for another final coating such as a paint or lubricant, but it will also lead to larger sites for potential corrosion. These coatings are often relatively thick and vary with exact composition.[3] One downfall of the thick coating is that they do not have the mechanical strength and flexibility of the metal or alloy onto which they are coated. Stress in the coating can cause fractures, which will bring sites for potential corrosion of the metal or alloy.

In one industrial coating,[4] it was shown that a phosphate film could be put on an aluminum alloy (93.5 wt% Al, 4.4 wt% Cu, 1.5 wt% Mg, 0.6 wt% Mn), but there was an oxide layer between the metal and the phosphate film. The phosphate film is thick, 4000Å, and is composed primarily of Al PO_4 with the outer most layer being a hydrated

Al $PO_4.nH_2O$ ($n \leq 1$). Other components of the alloy were not detected in the oxide, as they may have existed below the limits of detection (0.1%). The procedure by which the coating is made is known as phosphoric acid anodization, PAA. In PAA, the aluminum is placed in a phosphoric acids solution (10 wt%) and anodized at +10 volts. This process grows a rough oxide, 100Å, and a porous phosphate top layer. (figure 1) The goal of this procedure is to create an oxide rough enough to promote adhesion of the porous phosphate layer. The native oxide on aluminum is thin, 30Å, but it is much too smooth for good adhesion. The Boeing Corporation pioneered this process in the early 1970's. The films are used in the aircraft industry to help in adhesion of aluminum parts in airplanes.

2.5.2 Implant Phosphate Coatings

Research has primarily focused on the use of calcium phosphate coatings on titanium and its potential for bioimplantation. Titanium and its alloys are the common choice for implants due to their strength and lightness. These implants can be patella implants, hip implants or even dental implants. On these implants a natural titanium oxide, TiO_2, exists. Work has been done which shows that a calcium phosphate layer can be grown on this oxide layer using a solution of calcium chloride and potassium dihydrogen phosphate. The calcium phosphate layer is a mixture of different phases, which over time will dissolve in the body and reform to form a hydroxyapatite layer, $Ca_{10}(PO_4)_6(OH)_2$. Hydroxyapatite is the calcium phosphate phase form that primarily makes up bone, dentin and enamel in the human body. This layer will grow around the implant and hopefully allow for direct attachment of the implant to the bone or ligaments.

One difficulty with this process is controlling the rate of dissolution of the calcium phosphate layer. It has been proposed that if the layer dissolves too fast then the adhesion of the hydroxyapatite to the titanium oxide is weakened or lost.[5] This has been seen mostly in dental implants, which is why the currently used implants are screwed or forced by pressure into the jaw bone, making adhesion less necessary.

2.5.3 Oxide-free Phosphate Coatings

The Sherwood group has worked to produce phosphate coatings, which are quite different from the phosphate coatings discussed previously.[12-15] These phosphate coatings have no metal oxide layer between the phosphate and the metal and they are much thinner, being less then 100Å. It has been shown that a phosphate coating can be put on the surface of titanium, copper, aluminum, and iron metals without the presence of oxide at the interface. The results can be divide into two experiments, those reactions have been conducted in an anaerobic cell so conditions can be controlled or those conducted "on a bench top" by a newly designed process. Figure 2.2 illustrates both methods. The processes for the formation of the phosphate layer on the metal surface begins with the cleaning of the metal surface. This means that the natural oxide layer present is removed exposing fresh metal. Then the metal is reacted with an acid solution. The reaction of the acid and the metal creates a thin film on the metal. The film is then rinsed with distilled water and analyzed.

The anaerobic cell method, 1 in Figure 2.2, uses argon-ion etching as a means to remove the native surface formed on a metal. The etched metal surface is then brought to standard pressure for reaction with the acid. The use of a nitrogen environment allows

for no oxidation of the metal before reaction with the acid. The sample can be then pumped back down UHV conditions for analysis. The entire process occurs without the entrance of any atmospheric contact with the metal of the coating.

The bench top coating method, 2 in Figure 2.2, allows for the coatings to be created in atmosphere. The metal is submerged in an acid solution and abraded with a high grit waterproof emery paper to remove the native layer. The exposed fresh metal can then react with the acid solution forming the phosphate layer.

The experiments in the controlled environments showed similar results.[6-9] The reaction of titanium metal with phosphoric acid to creates a thin oxide free film were analyzed. During the reaction with the metal, a reduction of the orthophosphate ion was seen, forming a titanium metaphosphate film on the surface of the titanium metal. This thin film was then brought into normal atmosphere. The results of analysis of this film after extended exposure to the atmosphere showed that film became more orthophosphate in nature. The metaphosphate had oxidized in the surface, but no presence of oxide was seen. The same study was carried out using copper metal and similar results were seen. The initial reaction in the controlled environment creates a film consisting of Cu(I) metaphosphate. The exposure of the surface to atmosphere oxidized the phosphate on the surface to orthophosphate similar to the titanium example; both were shown to be oxide-free. Aluminum metal also showed what copper and titanium exhibited. The only metal that showed a different result was iron, as it formed an orthophosphate on the surface initially, not a metaphosphate.

Aluminum has also had some additional studies performed on it, utilizing the newly developed bench top coating process.[10,11] The new procedure creates similar coatings

on the metal surface and has been used to create a new series of coatings on the metal surface. The orthophosphate coating created by this method creates a similar coating to the coating seen in the anaerobic cell method after the coating had been exposed to atmospheric conditions. One study,[10] showed it is possible to create coatings with different types of phosphorus oxide acids being used to coat aluminum metal. The new acids used were hypophosphorous acid (H_3PO_2) and phosphorus acid (H_3PO_3), in addition to the orthophosphoric acid (H_3PO_4). The phosphate groups in the coatings resembled the acid used for the coating.

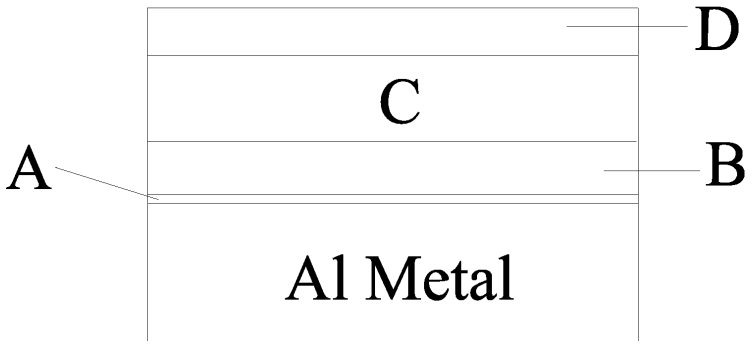

Figure 2.1 The phosphate coated aluminum sample by Boeing, showing the native oxide layer (A) the porous grown oxide(B) the phosphate film (C) and hydrated phosphate (D) layers.

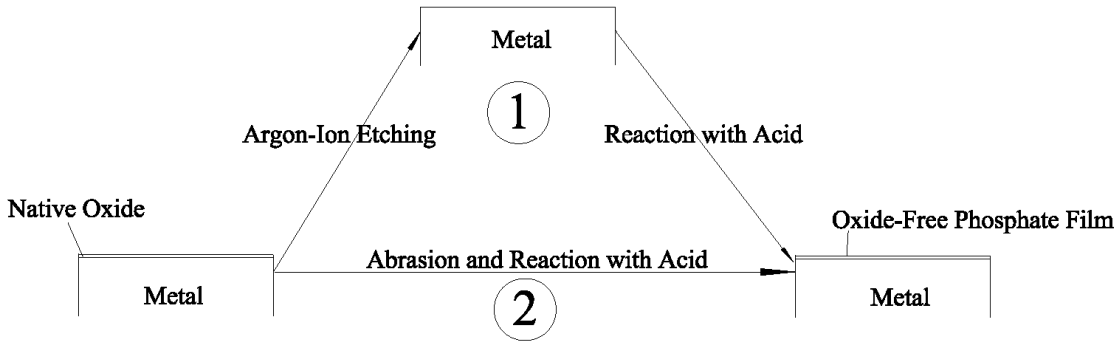

Figure 2.2 The oxide-free phosphate films formed on the metal surface by the Sherwood group.

2.6 References

1. L.L. Shreir, R.A. Jarman, G.T. Burstein. Corrosion Oxford, Boston : Butterworth-Heinemann, 1994.

2. Virmani, Y.P. Publication # FHWA-RD-01-156 U.S. Department of Transportation

3. . J.R. Van Wazer, "Phosphorus and Its Compounds, Volume 2. Technology, Biological Functions, and Applications", Interscience Publications, New York, 1961.

4. G.D. Davis, T.S. Sun, J.S. Ahearn, J.D. Venables, *Journal of Materials Chemistry*, **17**, 1807-1818, 1982.

5. C. Pritchard, *The Medical Post*, **37**, #41, Dec. 4, 2001.

6. Peter M.A. Sherwood and John A. Rotole, **United States Patent No.: 6,066,403** – Patent issued May 23, 2000

7. J.A. Rotole and Peter M.A. Sherwood, *Journal of Vacuum Science and Technology*, **A18**, 1066-1071, 2000.

8. John A. Rotole, Karen Gaskell, Alex Comte and Peter M.A. Sherwood, *Journal of*

Vacuum Science and Technology A, **19**, 1176-1181, 2001.

9. John A. Rotole and Peter M.A. Sherwood, *Chemistry of Materials*, **13**, 3933-3942, 2001.

10. K. Gaskell, M. Smith, P.M.A. Sherwood, J. Vac. Sci. Technol.A **19**, 1176 (2004).

11. Y-Q Wang and P.M.A. Sherwood, J. Vac. Sci. Technol. A, **21**, 11 (2003).

Chapter 3

Vanadium and its Compounds

3.1 Introduction

Vanadium metal was originally discovered in 1801 by Andres Manuel del Rio, in Mexico. The discovery was disregarded, as the scientists were convinced it was contaminated chromium. There was a rediscovery of vanadium in 1830 by the Swedish chemist Nils Gabriel Seftstrom. He then named the element after the Norse goddess Vanadis, representing beauty and fertility.[1] The oxides of vanadium have found their way into many uses. One general area of study, catalysis, also finds use of more vanadium compounds, namely, vanadium phosphates.

3.2 Vanadium

Vanadium has been used industrially since the early 1900's. It was first isolated in its purest metallic form by two American scientists who reduced vanadium pentoxide with calcium metal.[1] Vanadium has many properties, such as added strength in alloying, being a light-weight metal, and good corrosion resistance, which allowed it to find its way into many applications. A famous story exists involving the early years of vanadium use in the United States.

Henry Ford was one of the first enthusiasts for vanadium steel and his interest stemmed from a day at the automobile racetrack. He was observing a crash of a French automobile and he noticed that certain parts of the automobile had not broken with the

large impact, namely the crankshaft and that the alloy was lighter than normal steel. Inquiring about the nature of the material that the driveshaft was created from, Henry Ford learned from the French team of the vanadium steel used in its construction. Impressed, Ford went on to make the famous Model "T" shortly after and every crankshaft was made from vanadium steel. The interests of Ford in the applications of vanadium in steel lead to a large increase in the demand for Vanadium in the United States.[2]

Today vanadium's uses still center on steel. In a pure metallic form its uses are generally limited to the use as a cladding agent bonding titanium to steel, or as a sample holder for neutron diffraction. The neutron diffraction studies are possible because vanadium has a very low cross section for neutron diffraction. Vanadium's oxides and phosphates have found much work in the area of catalysis.[3]

Vanadium is the 22nd most abundant element in the earth's crust. China, South Africa, Russia, and Australia are the world leaders in the production of vanadium. 85% of the vanadium produced in the world is in the form of ferrovanadium, for use in the steel industry. Vanadium has two naturally occurring isotopes, ^{50}V (0.24%) and ^{51}V (99.76%). It configures itself in the body-centered cubic crystal symmetry with a cell length of 5.7448 Å. It has a high melting point of 1910ºC and its boiling point is 3407ºC.[4]

Corrosion studies of vanadium show that it has good resistance to atmospheric conditions, moisture, and even salt water damage. It forms a passive oxide layer similar to that of aluminum. The layer is formed by the chemisorption of oxidizing species from the atmosphere, such as O_2.

3.3 Vanadium Oxides

As oxygen begins incorporating itself in the vanadium surface, many stable phase of vanadium oxide are possible. Vanadium oxides have had application in many fields due to their physical and chemical properties. Some of these applications include uses in memory storage media, temperature sensors, light detectors, and catalysis.[5] VO, V_2O_3, VO_2, and V_2O_5 represent the vanadium oxides corresponding to vanadium in the II, III, IV, and V formal oxidation states. Table 3.2 lists some of the physical properties of these oxides.

3.3.1 VO

The formal V(II) state is seen in VO. This is believed to be the least stable formal oxide of vanadium. Recent studies have shown that it can decompose itself from VO to a stable V and V_2O_3.[6] The structure of VO can be represented as six octahedrally coordinated oxygen atoms around a central vanadium atom. The shortest bond length between the oxygen and vanadium is 2.09Å.[5,7]

3.3.2 V_2O_3

The vanadium sesquioxide, V_2O_3, is a metallic conductor a room termperature. It crystallizes in a rhombohedral structure. This compound has been extensively studied.[5,8] The most studied property of vanadium oxides is a insulator-to-metal phase transition that occurs in these compounds. The transition occurs at a temperature, T_c, which was seen to be much lower in the vanadium oxides than many other metal oxides. The electronic

structures of these compounds have been studied in an effort to understand the transition that occurs. Vanadium sesquioxide is perhaps the most studied of these vanadium oxides. At 168K a transition occurs shifting the compound from a monoclinic to a corundum structure, which explains the room-temperature conductivity seen in this compound.

3.3.3 VO_2

Vanadium dioxide, VO_2, also exhibits the insulator-to-metal transition. In this compound it occurs at 341 K where the monoclinic structure shifts to a rutile structure. The transition in this compound brings a drastic change in physical features. The resistance value of the compound has decreased greatly and the transmittance of infrared radiation is decreased so that the light is reflected instead of transmitted.[5,9]

3.3.4 V_2O_5

Vanadium pentoxide, V_2O_5, represents the most oxidized form of vanadium. This oxide contains a short, vanadyl type (VO), bond at 1.58Å. The color of this compound is a dark-yellow/orange color, showing drastic differences from the dioxide's deep-blue color.[5,10] Vanadium pentoxide is a very porous medium, which in combination with the multiple lower oxidation states, has brought about its applications in electrical storage. Intercalation of lithium ions in the matrix has been studied extensively and is now used as a battery source.[11]

3.3.5 Mixed Oxides

Besides the formal, II, III, IV, and V oxidation states forming compounds, a series of mixed oxides exist between the III and IV states and the IV and V states.[12] These phases are believed to contain multiple oxidation states for vanadium. This is a result of defects, primarily missing oxygen atoms, in the crystal lattice for the formal oxidation state compounds. V_6O_{13} is a well characterized phase existing between the V(IV) and V(V) formal states.[12]

3.4 Vanadium Phosphates

3.4.1 Introduction to Phosphates

The structure of phosphates is well-defined, and has been for over a hundred years.[13,14] Figure 3.1 displays some of these anions, possible by protonating (I), reducing (II) or condensing (III) the common orthophosphate ion. Protonation of the orthophosphate ion (a) gives the hydrogenphosphate ion (b) and the dihydrogenphosphate ion (c). Removal of the oxygen atoms on the phosphate ion and replacing with hydrogen (II) gives to reduced phosphates, the phosphorus ion (d) and the hypophosphorus ion (e). The last form of phosphate considered here is the pyrophosphate (f), which is a simple condensed phosphate where 2 orthophosphate ions are linked (III) by a bridging oxygen atom.

3.4.2 Vanadium Phosphates

Vanadium phosphates initially attracted attention as catalysts for the production of maleic anhydride by oxidizing of n-butane. Maleic anhydride is a precursor chemical for

many industrially used chemicals.[15] Since the initial emergence, many forms of vanadium phosphate have been isolated and the use of these compounds for the oxidation of light alkanes has been studied.[16]

The oxidation of n-butane to maleic anhydride is carried out using a vanadyl pyrophosphate catalyst, $(VO)_2P_2O_7$. It has received much attention, as it is believed to be one of the most highly selective catalysts known today. The catalyst is formed from precursors, $VOHPO_4 \cdot 1/2H_2O$ and $VOPO_4 \cdot 2H_2O$, which are stable at room temperature. The precursors, vanadyl hydrogenphosphate hemihydrate and vandyl orthophosphate dehydrate are produced by the reaction of vanadium pentoxide and phosphoric acid in different conditions.[6]

Table 3.1

Properties of Vanadium Metal

Atomic Weight	50.942 g/mol
Melting Point	1919 ºC
Boiling Point	3400 ºC
Density	6.092 g/cc
Crystal Structure	Body-Centered Cubic
Lattice Contstant	5.7448 Å

Table 3.2

Vanadium Oxides

Ox. State	Formula	Crystal Str.	Melting Pt.(°C)	V-O Bond (Å)
II	VO	Cubic	950	2.05
III	V_2O_3	Monoclinic ($<T_c$)		1.97
		Rhombohedral ($>T_c$)	1967	
IV	VO_2	Monoclinic ($<T_c$)		1.76
		Rutile ($>T_c$)	1637	
V	V_2O_5	Orthorhombic	658	1.58

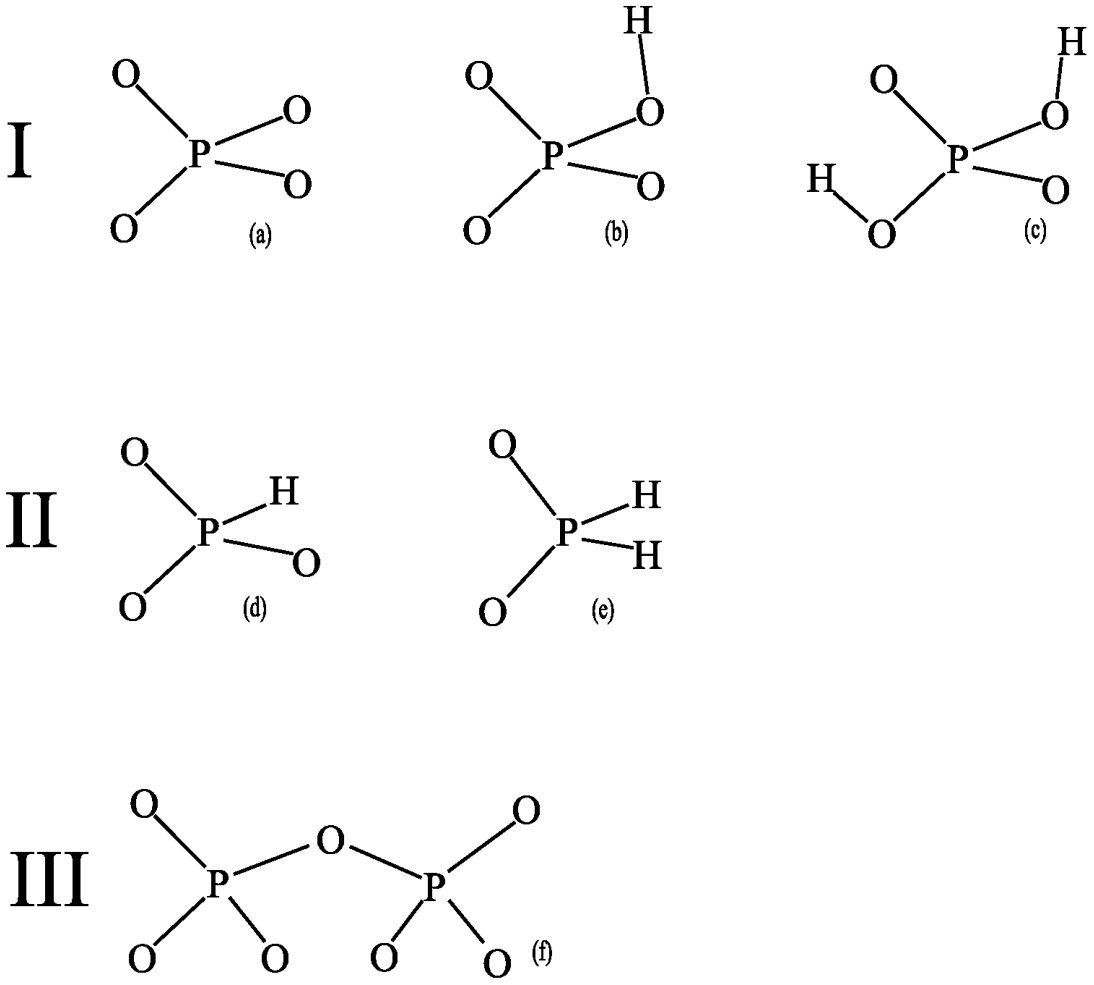

Figure 3.1 The different types of phosphate possible from the protonation (I), reduction (II), or linking (III) of the orthophosphate ion (a). The new forms are the hydrogenphosphate (b), dihydrogenphosphate (c), phosphorus (d), hypophosphorus (e), pyrophosphate (f) ions.

3.4 References

1. R. J. H. Clark: The Chemistry of Titanium and Vanadium, Elsevier, Amsterdam (1968).
2. from "Ford and The Model T" a chapter in Daniel Gross Forbes, Greatest Business Stories, , Byron Preiss Visual Publications, Inc. and Forbes Inc. **1996.**
3. R.R. Moskalyk, A.M. Alfantazi Minerals Engineering **16**, 793-805 (2003).
4. B.M. Vasyutinsky, G.H. Kartmazov, Y.M. Smirnov, V.A. Finkel, Phys. Met. Metall., 21, 134 (1966).
5. G. Kresse, S. Surnev, M.G. Ramsey, F.P. Netzer. Surface Science **492**, 329-344 (2001).
6. R.E. Loehman, C.N.R. Rao, J.M. Honig. J. Phys. Chem. **73**, 1781-1784 (1969).
7. S. Surnev, M.G. Ramsey, F.P. Netzer. Progress in Surface Science **73**, 117-165
8. C.E. Rice, W.R. Robinson. J. Solid State Chem. **21**, 145-154 (1977). (2003).
9. F. Theobald, R. Cabala, J. Bernard. J. Solid State Chem. **17**, 431-438 (1977).
10. R. Enjalbert, J. Galy Acta Cryst. C42, 1467-1469 (1986)
11. D. B. Le, S. Passerini, J. Guo, J. Ressler, B. B. Owens, W. H. Smyrl J. Electrochemical Society **143**, 2099-2105 (1996).
12. T. Schmitt, L.-C. Duda, M. Matsubara, M. Mattesini M. Klemm, A. Augustsson, J-H Guo, T. Uozumi, S. Horn, R. Ahuja, A. Kotani, and J. Nordgren Phys. Rev. B **69**, 125103 (2004).
13. John R. Van Wazer. Phosphorus and Its Compound vol. I. Interscience Publishers: New York. **1958**.

14. Thomas P. Whaley. Sodium, Potassium, Rubidium, Cesium, and Francium, Comprehensive Inorganic Chemistry, vol. 1. Pergamon Press: Oxford. **1973.**

15. G.J Hutchings, C.J. Kiely, M.T. Sananes-Schulz, A. Burrows, J-C. Volta Catalysis Today **40** 273-286 (1998).

16. J-C Volta. Surface Chemistry and Catalysis **3** 717-723 (2000).

Chapter 4

X-Ray Photoelectron Spectroscopy and Spectral Analysis

4.1 Surface Analysis

X-ray photoelectron spectroscopy, XPS, is a technique that took its modern form in the 1960's. Since then, further changes in technology has made it possible to make high resolution measurements. The spectra collected in an XPS experiment are the result of analyzing the electrons being ejected from a surface.

4.1.1 General Instrumental Setup

Figure 4.1 shows a general setup diagram for the instruments in the laboratory showing a standard setup with an achromatic X-ray source (a) or monochromatic source (b). The X-rays are generated at the source and aimed at a sample. The high energy of the X-rays impinging on the surface causes the emission of electrons form the surface. These photoelectrons are collected and analyzed above the sample by the use of a lens system and a hemispherical analyzer, which use electric fields to select a certain kinetic energy to pass through to the detector. The detector quantifies the number of electrons ejected per unit time, at the kinetic energy selected by the lens system and hemispherical analyzer.

4.1.2 X-Ray Source and Monochromatic vs. Achromatic Radiation

An excitation source is used which will produce X-rays of known intensity such as magnesium, 1253.6eV, or aluminum, 1486.6eV. Other anodes such as titanium or

silicon are sometimes used but studies here are conducted with Al. The X-ray output of the source used in XPS consists primarily of an intense energy emission, actually two energy lines, that are close in energy, known as the $K\alpha_{1,2}$ doublet. The source also emits radiation at other energies, in particular a doublet of lines that are less intense at a lower energy, which unless removed will also create photoelectrons from the surface of the sample, generating a second photoelectron spectrum shifted to lower binding energy. The features created by this secondary, or $K\alpha_{3,4}$, doublet makes the spectrum more complex with overlapping features. A monochromator can be used to remove all X-ray emission other than a single narrow emission at the $K\alpha_1$ energy. Another reason for the use of the monchromator is the removal of a weaker but still present background radiation. This background radiation is much weaker in intensity than the main features ($K\alpha_{1,2}$), or the secondary features ($K\alpha_{3,4}$), but it still adds to background seen in the spectra. This radiation is called Bremstrahlung radiation and is a continuous across all energy values being especially significant at high energy, but is removed by the use of a monochromator.

Figure 4.1(b) shows an experimental setup which uses a monochromator in conjunction with the spectrometer. The monochromator contains a specially designed quartz mirror that is actually 36 individually mounted crystals positioned to create a torroidal mirror. The mirror uses the first order diffraction of the Al $K\alpha_1$ line from the Al $K\alpha_{1,2}$ doublet on the 1010 crystal plane of quartz. The Bragg relation, equation 4.1, defines the Bragg angle,

$$n\lambda = 2d\sin\theta \qquad (4.1)$$

θ, of 78.5º for the parameters for the Al $K\alpha_1$ which means that the angle is 23º between the source and the sample with the center of the mirror at the vertex. The Bragg angle is the incidental angle to the crystal plane of interest. The monochromator creates a situation where the source, sample, and a specially designed quartz mirror are all on what is known as a Rowland circle.[2] The Rowland circle ensures that conditions are met so the radiation of the correct energy can be focused on the sample. This effectively narrows the linewidth of the excitation X-radiation and removes any unwanted secondary lines. All work here has been collected with monochromatic radiation.

4.1.3 Lens System and Hemispherical Analyzer

The lens system contains a series of cylindrical stainless steel tubes. The tubes are held at various potentials and act similarly to optical lenses, focusing the electron ejected from the surface. The electric field also retards the electrons as they pass to the analyzer.

The radius of the analyzer weighs heavily on the resolution possible at the detector.[2] The analyzer has two hemispheres separated by a small distance and the average radius of the hemispheres is determined by equation 4.2.

$$R_{avg.} = (R_{inner} + R_{outer})/2 \qquad (4.2)$$

The magnitude of voltages applied to the hemispheres, $V_{hemisphere}$, determines the kinetic energy of the electron that will travel without collision to the detector. This energy, E_{pass}

is known as the pass energy for the detector and is related to the voltage difference by equation 4.3.

$$V_{hemisphere}=E_{pass}[2(R_{avg}/R_{hemisphere})-1] \qquad (4.3)$$

The resolution of the analyzer at the detector, ΔE, is then determined by equation 4.4,

$$\Delta E= E_{pass}[(W/2R_{avg.})+(\alpha^2/4)] \qquad (4.4)$$

where W is the slit size at the detector and α is the acceptance angle of the detector. Further explanation of the equations and their derivation is available elsewhere.[2] A larger average radius of the analyzer will decrease the value of ΔE, which increases the resolution. There are two common modes of instrument operation, constant pass energy (CPE) or constant retardation ratio (CRR). In the CPE mode the analyzer is held at a constant pass energy which gives one resolution value over the whole range of kinetic energies. The CRR mode has the retardation ratio of the detector at a constant and the pass energies of the analyzer are scanned, which changes the resolution at given kinetic energies.

4.1.4 Detectors

The monochromatic instrument has a multichannel detector system equipped at the exit of the analyzer. This system allows for a further increase in resolution when compared to that of a single channel detector system. Two multichannel plates are

sandwiched together and a high potential is put across them. Placing these plates at the focal point of the analyzer allow for the detection of an array of energy to be detected. The energy range across the detector is determined as approximately 11% of the pass energy. The microchannel plates have a two-dimensional array of microscopic tunnels which collect and amplify the electrons exiting the analyzer and below the microchannel plates there are 16 gold electrodes in a row to collect the signal. This effectively gives 16 channels of information being collected simultaneously. Scanning the kinetic energy will cause each energy value to slowly pass over each channel, effectively detecting it 16 times. These abilities add speed and resolution when compared to the single channel setup.

4.1.5 Anaerobic Cell

Positioned next to the analysis chamber where the XPS spectra are collected is a specially designed chamber known as the anaerobic cell.[17] The anaerobic cell, shown in Figure 4.2, is a chamber, B, that controlled experiments are performed in. Electrochemical apparatus, E and R, can be raised or lowered from secondary chambers above, C, or below, D, the main chamber. These chambers are isolated from the anaerobic cell chamber and the main analysis chamber by a series of gate valves, g(1-4), allowing for the apparatus to be removed and the sample pumped for analysis. Positioned in the anaerobic cell is an argon-ion etcher, F, which uses argon ions accelerated toward a surface at high potentials. These ions bombard the surface, fracturing it and allowing for the removal of layers from the surface.

4.2 Obtaining Binding Energies in XPS

The emission of a photoelectron from a surface is considered a three step process. The three step model is shown in Figure 4.3. The first step in the process is the excitation of the surface by the X-rays from the source, putting an electron in a high energy, virtual state. In the next step, the electron travels through the surface, to the vacuum/surface interface, during which time it is vulnerable to electron-electron and electron-phonon interactions. These interactions can lead to inelastic scattering resulting in background signal seen in experiment. The last step is the ejection of the electron into the vacuum, where it is collected and analyzed.

To relate the kinetic energy, KE, of the ejected electron to the energy of the orbital it was removed from, binding energy, BE, is used. To convert from kinetic energy to binding energy, equation 4.5 is used. [1] In the case of aluminum, the energy of the initial excitation energy, hν, is 1486.6eV.

$$KE = h\nu - BE \tag{4.5}$$

As the electrons at certain energies are counted there is some effect of the instrument on this value due to the potential between the sample and the instrument. The instrument work function, $\Phi_{spectrometer}$, can be determined and added to equation 4.5, as seen in equation 4.6.

$$KE = h\nu - BE' - \Phi_{spectrometer} \tag{4.6}$$

The energy of the spectrometer work function is usually on the order of 4-5eV. This equation holds true for conducting samples, but non-conducting samples need more interpretation. The binding energy, BE, in equation 4.5 is with respect to the vacuum level. The vacuum level is the point at which the electron exists outside of the pull from the site it left with no potential energy gained due to an attraction. The binding energy, corrected for the spectrometer work function, becomes with respect to the Fermi level instead of the vacuum level and the term is now BE'. [7]

The sample must be grounded so that the ejected electron can be replaced stopping the sample from charging. Simply grounding the sample works well for conducting samples, but non-conducting often times require the use of a flood gun, which will spray the surface with low energy electrons to replace the ejected ones. Even with the use of a flood gun to stop surface charging, there is still some constant surface charge, S, which must be taken into account (equation 4.7). The final equation becomes:

$$KE = h\nu - BE' - \Phi_{spectrometer} - S \qquad (4.7)$$

4.3 Properties of XPS Measurement

The features seen in an XPS spectrum are subject to many physical forces that govern them. An analysis of the data collected in a experiment requires an understanding of the types of properties that affect the spectra. Some of these properties include the escape depth of an electron at the surface, the spin-orbit splitting of the core level regions, and the affects of multiplet splitting on a spectrum.

4.3.1 Escape Depth

The measurements in XPS are inherently surface sensitive. This arises by the properties of the electron as it leaves the surface. The initial excitation photon penetrates deep into the surface, but it is the exit path and any interactions of the resulting photoelectron that are of interest. Figure 4.4(a) illustrates the process of the electron leaving the surface. Path 1 is an electron which came from near the surface and leaves the surface without any interaction with the surface. These electrons contribute to the peaks of the spectrum. Path 2 represents the result of an interaction of an ejected electron with either another electron or a surface atom. This is an inelastically scattered electron, which adds to the background of the spectrum.

The maximum depth (d_1), in Figure 4.4(a), to which an electron can be expected to be ejected and contribute to the spectra, is dependent on the kinetic energy of that ejected electron. It is observed that the greater the kinetic energy of the ejected electron, the larger the expected escape depth of that electron. The escape depth is where the surface sensitivity of XPS is generated and this property can be used to probe the surface at different depths. 67% of the photoelectron peak signal comes from the depth into the sample represented by the escape depth.

To probe the surface at different depths, change the angle of the surface with respect to the detector, Figure 4.4(b), allowing for a smaller effective probe depth. This is because the escape depth of the ejected electron is constant, but the distance the photoelectron has to travel before it can escape is greater for a given depth when the take-off angle is small. At a 90 degree (or normal) take off angle the distance traveled by the

photoelectron ejected from an atom at depth d_2 below the surface will be the same as this depth. When the take off angle is smaller, the photoelectron travels a greater distance, d_1, and so will appear to be at a greater depth, and thus have a lower intensity in the photoelectron spectrum. As the take off angle get smaller, the spectrum has an increasingly larger component from the outermost surface region. This explains how angle-resolved XPS achieves more surface sensitive analysis.

4.3.2 Spin-Orbit Splitting

A discussion of the physical properties that govern the peaks seen in experiment is needed in order to explain the terms that are assigned to these features.[1,2] The various splittings and intensities seen in XPS have been explained using two common approaches, each dealing with the angular momentum, J or *j*. Spin-orbit splitting is a feature which occurs whenever the orbital angular momentum, l, of the orbital where the electron was ejected is greater than 0. (*p, d, f,* etc.) What occurs is the splitting of the peak (which is most noticeable for core peaks because such peaks are associated with particular atomic energy levels), which can be described in terms of two final states, separated in energy by spin-orbit splitting. The total angular momentum is calculated from two quantum numbers, L and S, where $L=\sum l$ and $S=\sum s$. The total angular momentum, J, is represented by integer values from $\{|L+S| \ldots |L-S|\}$. The multiplicity and relative intensity of the spin-orbit split feature would be (2J+1), so for single *p* electron, L=1, S=1/2. The values of J are 3/2 and 1/2, which have multiplicities of 4 and 2, so the $p_{3/2}$ peak versus the $p_{1/2}$ peak will have twice the intensity. Evidence of

this can be seen in the vanadium 2p region, Figure 4.5, where the features for V_2O_5 have been fit with peaks whose area is 1:2.

4.3.3 Multiplet Splitting

Multiplet Splitting is found in compounds that contain unpaired electrons. This splitting can be especially complex in compounds that contain *d* and *f* electron character. These satellite features arise because unpaired electrons cause a number of possible final state configurations in the photoionization process. Configuration interaction says that the final state can be represented as a linear combination of all possible configurations that exist for the state.[3] The same is true for the ground state. The probability of other states being populated after photoionization is increased in these compounds with the presence of the unpaired electrons in the valence level due to the destabilizing effect they have on the core-hole that is created when the photoelectron is ejected. These other configurations of the final state have been explained by examining various theories.[4]

The coupling of the spin and orbital angular momenta discussed above for spin-oribit coupling becomes more complex with the presence of unpaired electrons in the valence levels. It is appropriate to consider the Russel-saunders coupling (L-S) process to understand the multiplet satellite features.[5,6] This is done now by coupling the hole created upon photoionization with the possible configurations for the ground state, in affect, calculating the possible states for a p^5d^1 configuration to represent the effects on the p core levels in a d^1 compound when a p electron is ejected. The possible terms from the ground state, for which there is only 1 for a d^1 configuration (^2D), when coupled with the p^5 state gives rise to the formation of 6 terms (^3F, ^3D, ^3P, ^1F, ^1D, ^1P). The states

corresponding to the 6 terms are possible final states in the photoionization process. These states only take into account the effects on the spectrum from the atom of interest assuming no interaction with other atoms.

Crystal field splitting in metal compounds is another property that can be used to further explain the complex multiplet structures seen.[5] The magnetic effects of the neighboring atoms around the central metal make the ground state of the *d* level to be split according to the arrangement of atoms around central atom. This would in turn create many more terms for the final state when coupling the core-hole with the split ground state.

Another process which explains the potential for more final states is ligand-to-metal charge transfer. Here, the ionization process leads to a state which can now also be represented as a configuration in which the transfer of one electron has been made from a ligand orbital to a metal orbital. The experimental features seen that correspond to this transfer are also due to the presence of unpaired electrons in the valence level, similarly to the features for multiplet splitting. Figure 4.6 illustrates the change in energy levels during ionization with the charge transfer process occurring. The example is based of the ionization of a d^9/d^1 system such as Cu^{2+}. The ground state is shown where the electron is still on the ligand, $d^9\underline{L}$, and also as if the transfer occurred pre-ionization, $d^{10}\underline{L}$. The probability would heavily favor the $d^9\underline{L}$ configuration, due to the energy required to transfer the electron to the metal. Upon ionization, the core *p* electron is removed, the p^5d^9 configuration has a higher energy due to the electrostatic interaction between the unpaired electrons. The energy of the state corresponding to ionization and charge transfer, $p^5d^{10}\underline{L}$, has lower energy than the p^5d^9 configuration, resulting in an increase in

kinetic energy of the ejected electron from path 2. The difference in energy between the various paths gives an explanation of the distances between these features seen experimentally. Paths 3 and 4 have very small contribution as the ground state, $d^{10}\underline{L}$, is also heavily un-favored. This explanation shows the charge transfer effects on the spectra and should be considered with Russel-Saunders coupling methods and the ideas of crystal field splitting to give a fuller explanation of what is seen experimentally. This would more accurately predict the multiplet splitting seen for an ionicly bound system.

4.4 Chemical Information from XPS

The electrons that are ejected from the surface can be separated into different types, those arising from the core level, those arising from the valence level and those arising from secondary electron processes. Figure 4.7 shows a survey, or overall scan, which is a complete emission spectrum for V_2O_5. The core level is higher in binding energy, above 30eV, then the valence band region, below 30eV. Other features exist, called auger electrons, which can also be seen in figure 4.7.

4.4.1 Core Level XPS

Core level XPS is the most published type of XPS experiment. The core level retains atomic nature, where the valence electrons are involved more in bonding and are more molecular in nature. The shifts seen in the features of the core level region with differences in oxidation state or bonding environment initially led to the thought that XPS could act as an all element NMR, this in not the case. *Koopman's theorem* states that the energy to remove an electron is equal to the binding energy of level where the electron

originated, which only accounts for the ground state of the atom. When an electron is ejected it creates an excited state, which must relax to a new, low energy, state. The energy involved in this process, called relaxation energy, will affect the final state of the electron during the photoionization process. To analyze this energy the relaxation potential model is used, which is a modified version of the ground state potential model.[8] These models make the assumption that an atom can be represented by a hollow conducting sphere. A potential measured inside a hollow conducting sphere is constant and is defined as the charge of the sphere divide by the radius, q/r. The ground state potential model then states that the chemical shift, ΔE, is defined as:

$$\Delta E = q_i/r_i + \sum q_j/r_{ij} \qquad (4.8)$$

The second term, $\sum q_j/r_{ij}$, takes into account the charges on the neighboring atoms and how they affect the chemical shift. This value in an ionic solid is known as the "Madelung Potential" can be calculated using point potentials. It has been shown that its affect on the chemical shift can be similar to that of the first term. Evidence of this can be seen in the chemical shift arising from a change in orientation, such as, tetrahedral to octahedral. Taking into account the relaxation energy creates the relaxation potential model, where R is the relaxation energy of the standard or compound.

$$\Delta E = q_i/r_i + \sum q_j/r_{ij} + R_{standard} - R_{compound} \qquad (4.9)$$

4.4.2 Valence Band XPS

The Sherwood group has shown over many years that valence band XPS has the capability to distinguish subtle differences in chemical composition in situations where core XPS shows no significant difference. Valence band XPS is a probe for electrons with low binding energies (<30eV), which have a molecular rather than atomic nature. These spectra are very sensitive to small differences in surface chemistry. A good example of the abilities of valence band XPS is differentiating between solids, which have the same formula, but different structure.[9] It was shown previously that the differences between α-Al_2O_3 and γ-Al_2O_3 could be resolved in the valence band region, but were not resolvable using core level XPS. The core regions showed identical shifts as the compounds differ only slightly in crystal structure. The valence band shows a change in peak separation and a change in the shape of the peaks at lower binding energy (0-5eV) which were evidence of the slight change in orientation. The analysis of the valence band region is made understandable by the use of calculation methods predicting the difference that could be seen. In the example of the aluminum oxides, the calculated valence band showed the same changes in the lower binding energy which greatly improves the confidence in the spectra.

4.4.3 Auger Electrons

Auger electrons are the result of relaxation of an ionized atom in which another, second electron is ejected.[2] When the source energy strikes an atom, it ionizes it and leaves it in an excited state. Relaxation of this excited state occurs as an electron moves

from a higher level to the core hole. This process can proceed in two ways, it will either create energy that is released as a photon, which is X-ray fluorescence, or it will release energy that causes the emission of an additional, Auger, electron. The energy of the Auger electrons is independent of the source excitation energy so the features will have the same kinetic energy regardless of source type. These Auger electrons can be seen in an XPS overall, or survey, spectrum, Figure 4.7. The intense features for the O KLL auger features are seen at 1000eV. The analysis of Auger features will not be discussed in this text.

4.5 Analysis Methods for XPS

Analyzing and evaluating the data collected in experimentation can be accomplished by many means. The analysis of the overlapping features in the core level regions requires curve-fitting methods to identify the various contributors. Another analysis technique is the prediction of valence band XPS spectra using calculation methods. Each of these areas allow for a more complete understanding of the spectra seen.

4.5.1 Curve Fitting Methods

When quantifying features in XPS it is necessary to make sure that the analysis makes "chemical sense", as overlapping features require curve-fitting of the data. When considering complex spectra, creating synthesized peaks to represent different features in the spectra requires an understanding of the chemistry at the surface. Synthesizing peaks requires controlling of the different parameters for peak; *Peak Position, Peak Intensity, Peak Width, Gaussian/Lorentzian Mixing Ratio, Height of the Constant Tail, Slope of the Exponential Tail, and Tail Mixing Ratio.* The adjustment of these functions and the

parameters that control them must be done with the chemical state of the surface in mind. To attain the correct shapes for different chemical environments, the fitting of data from model compounds is an effective way to analyze more complex spectra. An analysis of the functions and exact methodology are given elsewhere.[10,11] The background or baseline chosen also has been studied and a variety of methods exist for accounting for the sloping intensity seen in XPS. The choice of background can greatly affect the quantative finding for a given spectrum.

4.5.2 Valence Band Prediction by Calculation Methods

As stated earlier in the aluminum oxide example, valence band spectra are interpreted using calculations which can be used to create a predicted spectrum. The predicted spectra are used to verify what is seen in the experimental data. It is a way of ensuring that the data collected is actually what it is supposed to be. In the case of α-Al_2O_3 and γ-Al_2O_3 the valence band spectra show a shift in peak separation and a change in peak shape, which was understood by comparing it to a predicted spectra.[9]

A process was developed to predict the valence band specta from a calculated density of states. Figure 4.8 shows outputs from the procedure to predict spectra showing the affect of incorporating the cross section values and the photon function. Here the process is being performed for a vanadium metal valence band spectrum. The first portion of the process is the calculation of the ground state configuration density of states. The total density of states is show in figure 4.8(a). The second part, Figure 4.8(b), of the figure shows the populated states in the metal. To create the predicted spectra, shown as Figure 4.8(c), the density of states is kept broken up into different projections

corresponding to the various atomic orbital contributions. These projections are adjusted to reflect their photoelectron cross sections as calculated by Scofield.[12] The projections are then recombined and then convoluted using a photon function that can be represented by a 50% Gaussian/Lorentzian product function (developed by our group), resulting in the spectrum in Figure 4.8(c).[13]

The calculation of the density of states for the aluminum oxide example was performed using a program called CRYSTAL.[14] That is one type of computational program, other computational programs are also employed in our work. Another example is the BNDPKG II program[15] developed to calculate metals in the body centered cubic family which was used to calculate the Vanadium metal spectrum shown in Figure 4.7. The third type of calculation is a multiple scattered-wave Xα calculation, which is performed on charged a cluster.[16] These programs calculate the valence band density of states for the species of interest. Even with differences in calculation methodology, each program outputs a calculated density of states broken down to its individual atomic orbital contributions.

Multiple scattered-wave Xα calculations were carried out by Professor P.M.A. Sherwood and are based upon charged clusters. The *Muffin-tin* model represents the atoms as charged spheres packed closely to minimize inter-sphere space with an outer sphere set to just encompass all atomic spheres. The outer sphere acts to neutralize the total charge of the inner spheres and is generally referred to as a Watson sphere. The model can be then broken down into three regions, the atomic region (inside the innerspheres), the interstitial or interatomic region (between the inner charged spheres, but inside the outer sphere) and the extramolecular region (area outside the outer sphere).

These calculations require a determination of the sphere radius of each of these charged spheres and the outer sphere. This determination is based on the bond lengths between these atoms and their neighboring atoms. Atomic potentials are calculated for the atom in the system. The molecular potential for the cluster is then constructed it by symmetrically adapting the charge densities for the various atomic spheres. A non-SCF calculation is performed and the initial set of parameters is acquired for use in the SCF calculation. The percentage atomic character that is calculated for each atomic sphere in the calculation when it has reached self-consistency can then be used to predict the valence band spectrum.

The calculations performed by CRYSTAL and BNDPKG II create a similar output to that of the multiple scattered-wave Xα calculations, but differ in the setup and approach. The position of the atoms is entered and for each elements present along with a corresponding basis set. The atoms in these systems are represented in the calculation by functions, known as Bloch functions. These Bloch functions are a linear combination of Gaussian type terms. The basis set is a list of parameters for the various shells, which are the atomic orbitals with the same values of *n* and *l*. These represent all the atomic orbitals for each of the elements existing in the calculation. The calculation creates a density of states for a three-dimensional surface, not a small cluster such as that used for the multiple scattered-wave Xa calculations.

4.6 References

1. P.M.A. Sherwood, "X-Ray Photoelectron Spectroscopy" in Handbook of Surface Imaging and Visualization, edited by A.T. Hubbard, CRC Press, Boca Raton, FL, Chapter 63, 875-887 (1995).

2. D.Briggs, M.P. Seah. *Practical Surface Analysis Second Edition – Vol. 1* , John Wiley and Sons Ltd., New York, 1990

3. G. van der Laar, C. Westra, C. Haas, G.A. Sawatzky. Phys. Rev.B, **23**, 4369 (1981).

4. Zhi-xun Shen, J.W. Allen, J.J. Yeh, J-S Kang, W. Ellis, W. Spicer, I. Lindau, M.B. Maple, Y.D. Dalichaouch, M.S. Torikachvili, J.Z. Sun, T.H. Gabelle. . Phys. Rev.B, **36**, 8414 (1987).

5. R.P. Gupta, S.K. Sen. Phys. Rev.B, **12**, 15-19 (1974).

6. R.P. Gupta, S.K. Sen. Phys. Rev.B, **10**, 71-77 (1974).

7. D. v.d. Marel, G.A. Sawatzky, J.A. Julianus J. Phys. **F14**, 281-290 (1984).

8. K. Siegbahn C. Nordling, A. Falhman, R. Nordberg, K. Hamrin, J. Hedman, G. Johanson, T. Bergmank, S.E. Karlsson, I. Lindgren *ESCA: Atomic Molecular and*

Solid State Studied by Means of Electron Spectrscopy Nova Acta Regiae Soc. Sci. Upsaliensis, Ser. IV, 20 (1967).

9. J.A. Rotole and Peter M.A. Sherwood, *Journal of Vacuum Science and Technology*, **A17**, 1122-1129 (1999).

10. P.M.A. Sherwood, *Analytical Chemistry*, **54**, 134, (1982).

11. P.M.A. Sherwood, *Journal of Vacuum Science and Technology*, **A14**, 1424-1432 (1996).

12. J.H. Scofield, *Journal of Electron Spectroscopy and Related Phenomena*, **8**, 129-137 (1972).

13. R.O. Ansel, T. Dickinson, A.F. Povey and P.M.A. Sherwood, *Journal of Electroanalytical Chemistry*, **98**, 79-89 (1979).

14. V.R. Sanders, R. Dovesi, C. Roetti, M. Causa, N.M. Harrison, R. Orlando, C.M. Zicovidh-Wilson, Crystal98, User's Manual, Version 1.0, 1999

15. N.E. Brener, J. Calaway, J.M. Tyler, *Chapter 16. BNDPKG2,* from *Modern Techniques in Computational Chemistry,* 785-803 (1990).

16. D.A.Case. *Annual Reports in Physical Chemistry*, **33**, 151 (1982).

17. Peter M.A. Sherwood and John A. Rotole, **United States Patent No.: 6,066,403** – Patent issued May 23, 2000

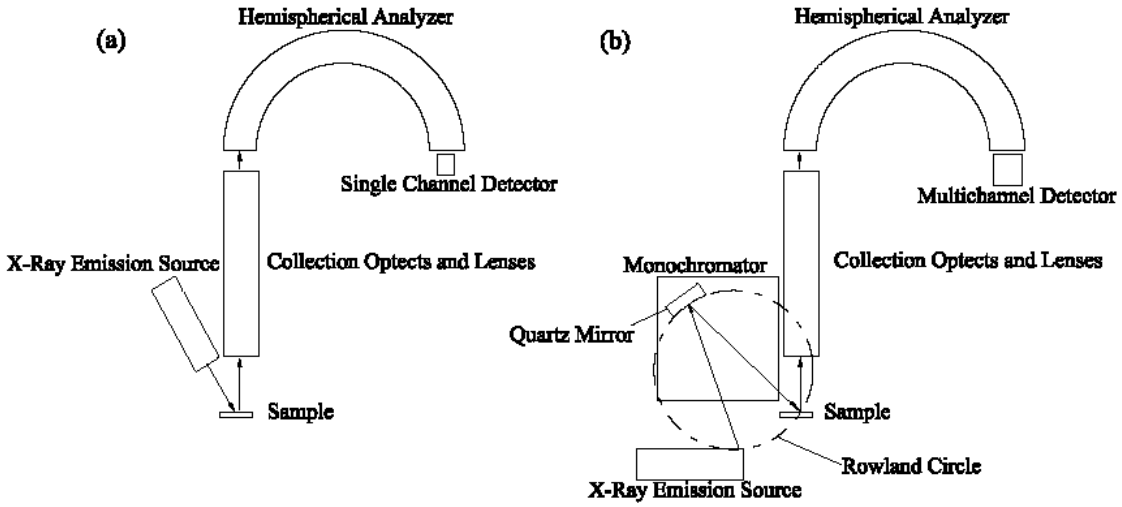

Figure 4.1 The instrumental setup for an XPS experiment, showing and achromatic source(a) and a monochromatic source(b).

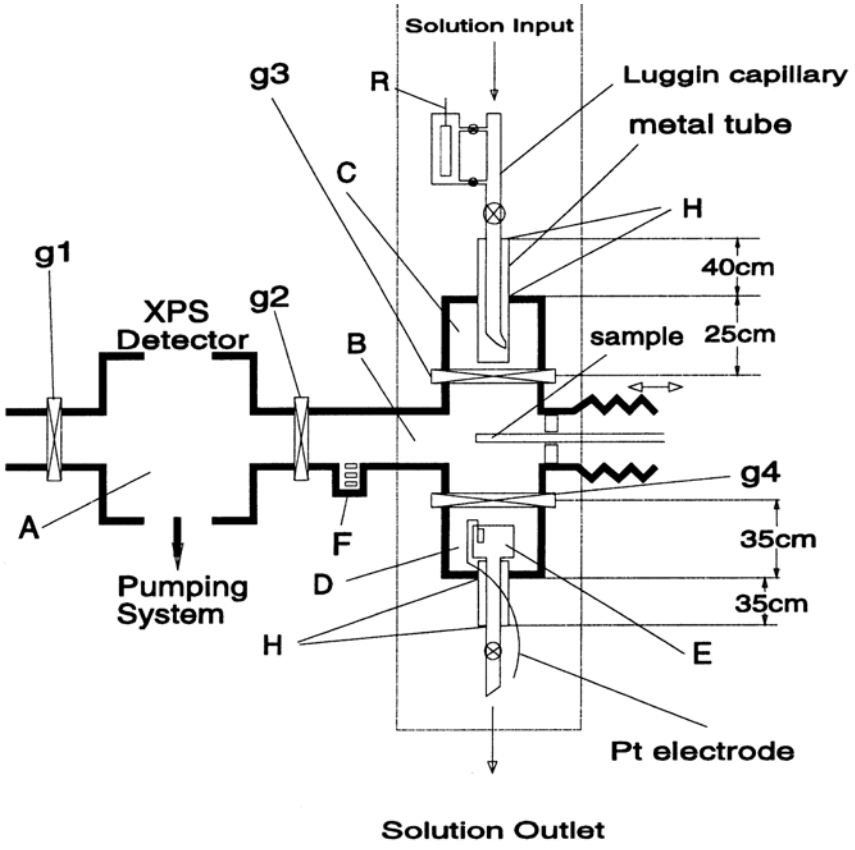

Figure 4.2 The anaerobic cell, used for carrying out controlled atmosphere reactions.

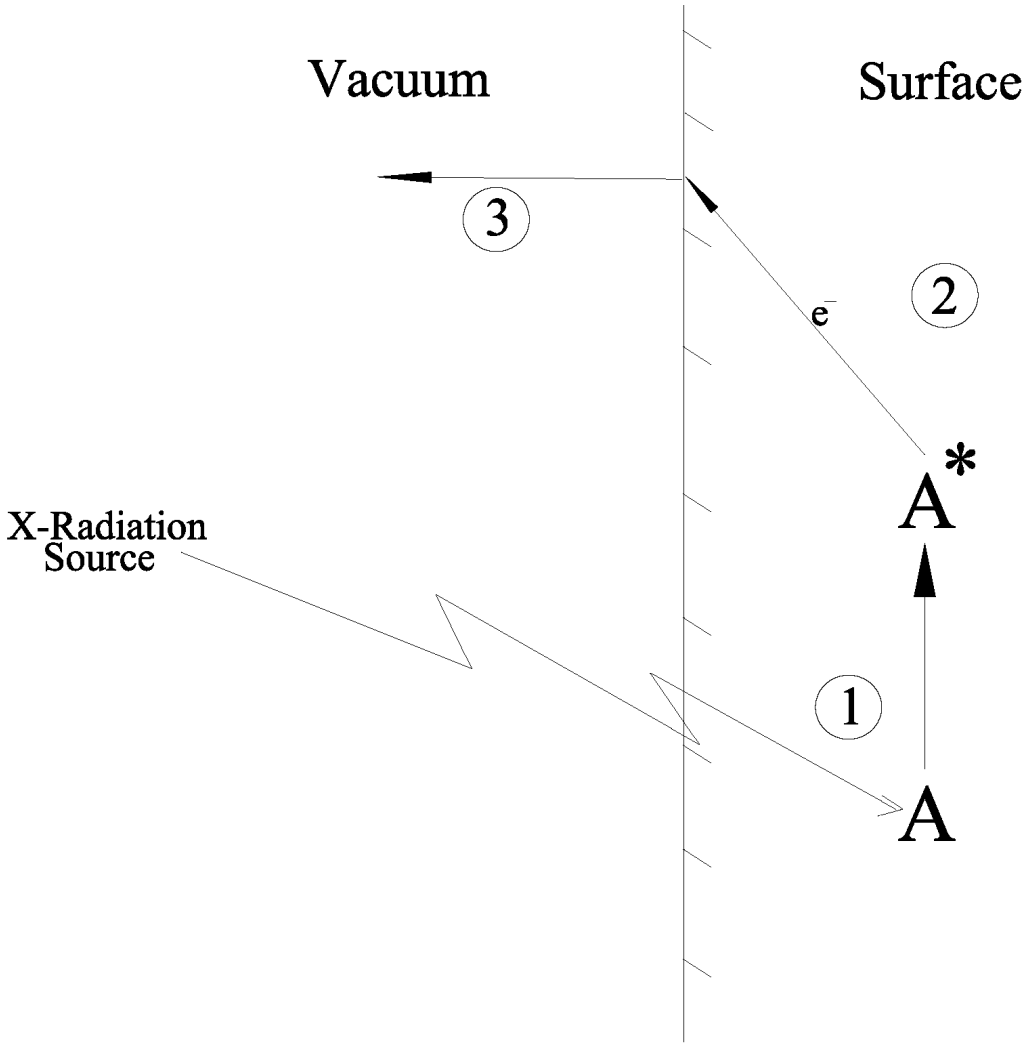

Figure 4.3 The Three-Step model showing the excitation of an atom (1), the path of the electron to the surface (2), and the ejection from the surface into the vacuum (3).

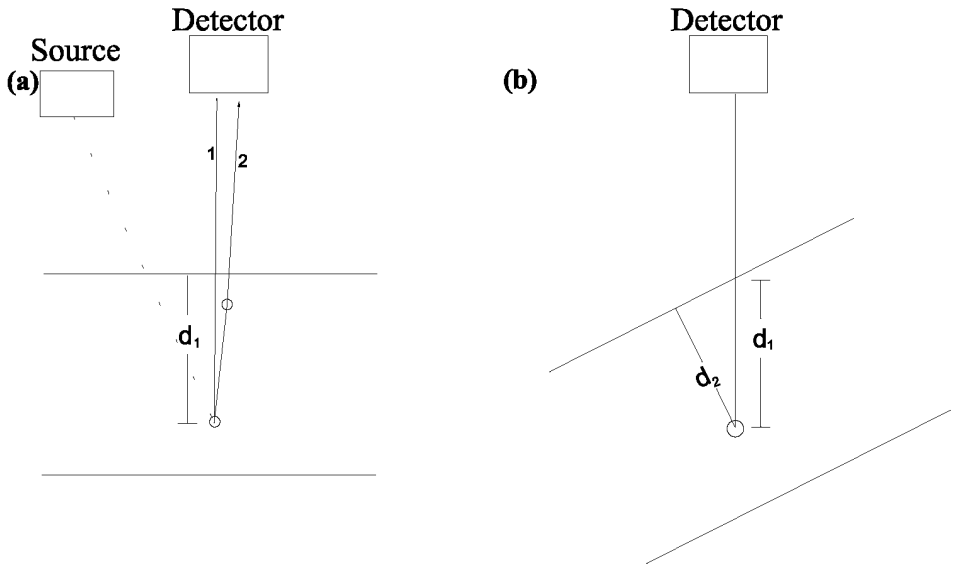

Figure 4.4 Potential interactions of ejected electrons (a) creating a finite escape depth and the use of angle-resolved XPS (b).

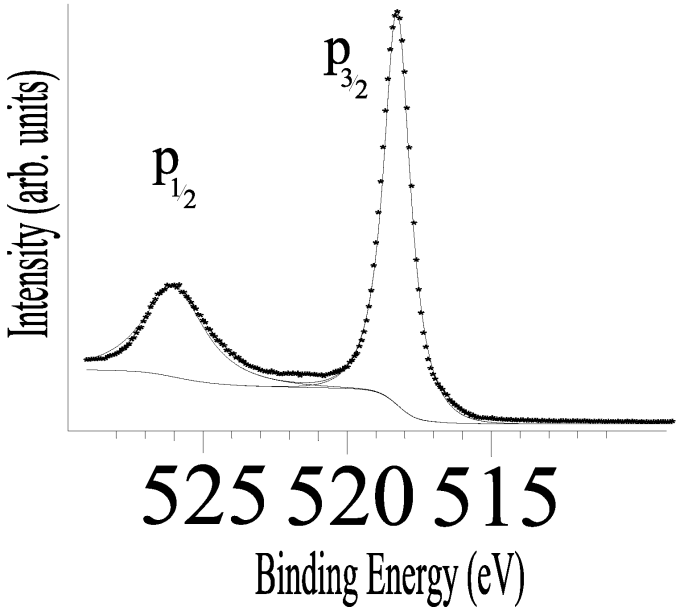

Figure 4.5 The Vanadium 2p core level region showing the spin-orbit splitting of the $p_{1/2}$ and $p_{3/2}$ features.

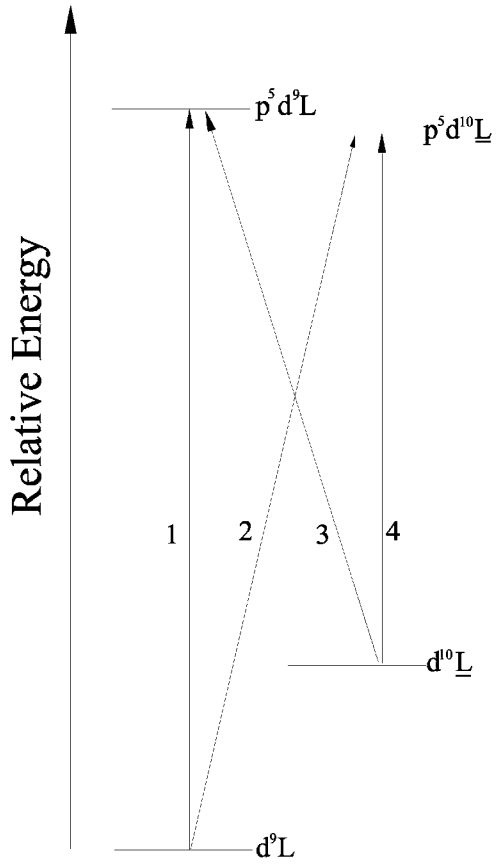

Figure 4.6 Explanation of the charge-transfer process occurring during X-ray excitation.

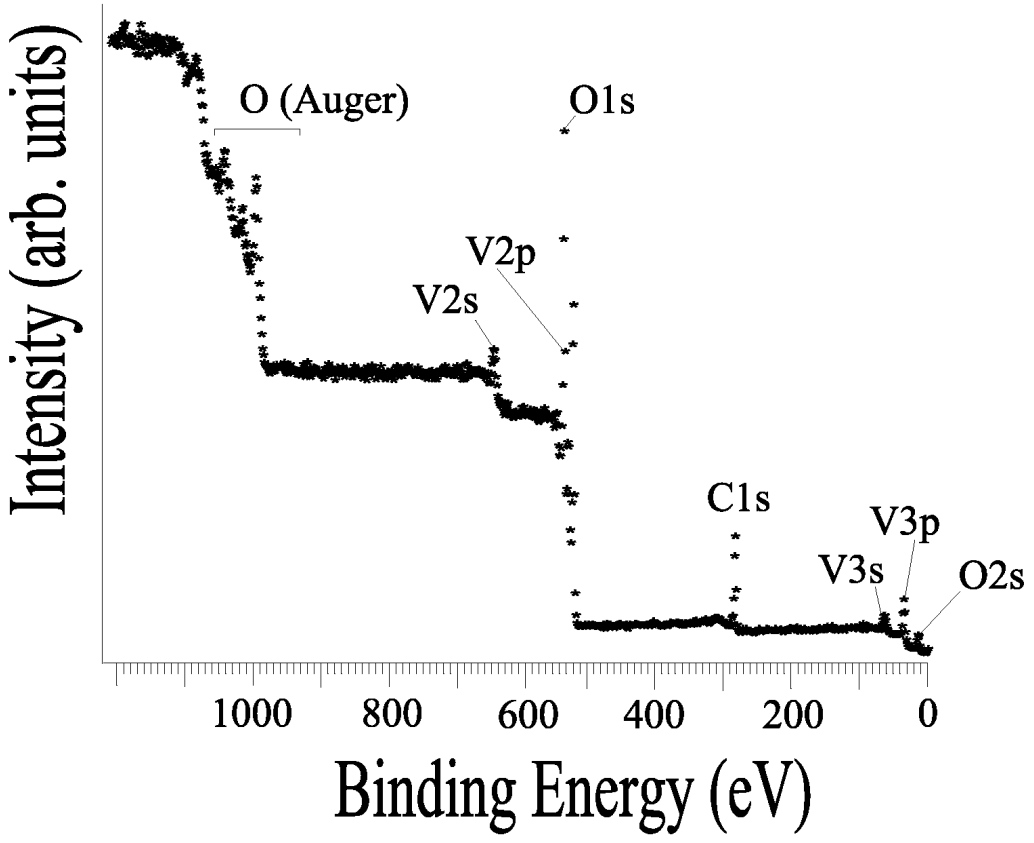

Figure 4.7 The Survey Spectrum of V2O5

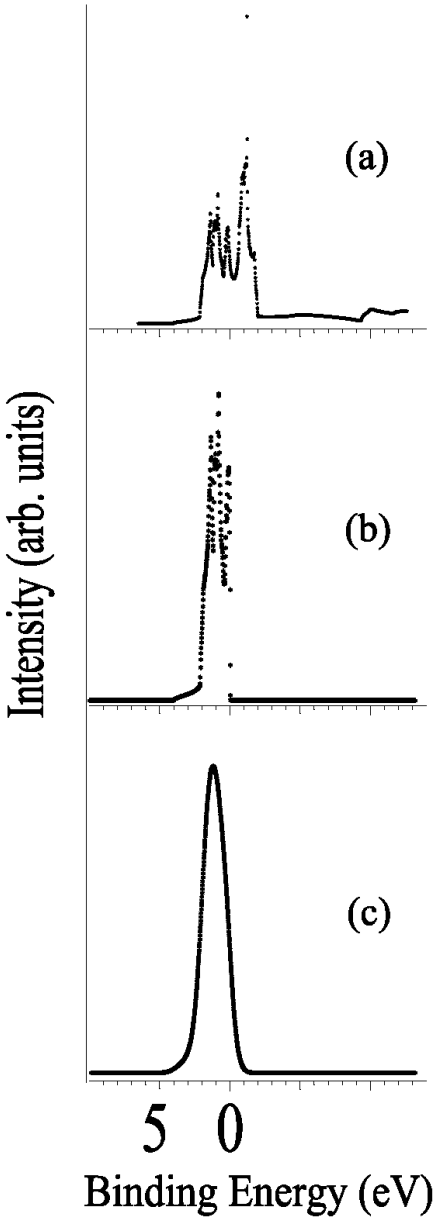

Figure 4.8 The outputs from parts of the process to predict valence band XPS spectra, showing the total density of states (a), the density of states to the Fermi level (b) and the photoelectron function, crossection adjusted, predicted spectra (c).

Chapter 5

Oxidation of Vanadium Metal and the Reaction of Vanadium Metal with 5M Phosphoric Acid in an Anaerobic Cell Studied by Core Level and Valence Band X-ray Photoelectron Spectroscopy

5.1 Introduction

Valence band X-ray photoelectron spectroscopy (XPS) has been shown to be an effective method for differentiating between the types of oxides that can form on the surfaces of metals.[1-3] Subtle changes in structure or bonding in different oxides yields changes in the valence band region, which allow for the differentiation of the oxides. A previous study showed it was possible to examine the different oxides or hydroxides on the surface of aluminum or steel using core level and valence band X-ray photoelectron spectroscopy (XPS). Here, this technique will be applied to examine the native oxide layer on vanadium metal.

In addition to long term oxidation of vanadium, the thin oxide layer that grows on clean vanadium metal and the layer that forms with the reaction of vanadium with water will be studied. These experiments tell how vanadium will naturally react with the environment under ambient conditions. Then, argon-ion etched vanadium was reacted with a 5M phosphoric acid solution in a specially designed anaerobic cell. This reaction was shown previously to create thin oxide-free phosphate layers on the surface of the metal when using copper, aluminum, iron and titanium.[4-7] Core level and valence band XPS have shown that not only can they identify different oxides, they can be used to distinguish between oxides from phosphates or other compounds that form on the surface. To aid with the analysis of the valence band region, band structure calculations have been

performed on simple vanadium oxides, which have been used to create a set of predicted spectra. These calculations have been shown to be a strong and effective way to analyze the valence band region.

5.2 Experimental

5.2.1 Materials and Preparation

Vanadium metal (99.0%) purchased from Sigma-Aldrich was analyzed, as-received, with a thick natural oxide layer covering the metal. Then, the sample was polished in air with a high grit silicon carbide emery paper to remove the majority of the oxide to examine the spectral features from the metal below.

In the second experiment, a piece of vanadium was abraded similar to the way it was polished, with the exception it was immersed in triply distilled water. The triply distilled water had been deaerated by bubbling with argon for 2 hours prior to experiment and continued bubbling throughout the abrasion process. This allows for the study of the oxidation of vanadium by water.

In the third experiment, a new piece of vanadium metal was placed in a UHV chamber and argon-ion etched for 2 hours to remove the native oxide layer. Then, in a specially designed anaerobic cell[4-7], the etched metal was allowed to react with a solution of 5M phosphoric acid without the presence of air contamination by backfilling the chamber to positive pressure with research grade argon from Matheson Tri-Gas.

5.2.2 Calculation Methods

The calculations in this chapter are either band structure calculations performed using CRYSTAL[8,9], for the oxides, or calculations performed by BNDPKG2[10], for the

metal. In each program separate densities of states for each atom in the compound are calculated. These grouped densities of states are then adjusted by their corresponding atomic photoelectron cross section values as determined by Scofield[11]. These cross section adjusted densities of states are then convoluted with a Gaussian /Lorentzian product function having a full width at half maximum of 1eV using a separate program written by one of the authors[12,13].

The band structure calculations were performed for the orthorhombic *Pmmn*[14] V_2O_5, the monoclinic *C 2/m*[15] structure of VO_2, the hexagonal *R-3c*[16] structure of V_2O_3 and the cubic *Fm3m*[17] structure of VO; all using basic STO-3G atomic orbitals. The calculation was done on the cubic *bcc*[18] structure of vanadium using the set of *s*, *p* and *d* orbital coefficients as determined by Wachters[19].

5.3 Results and Discussion

5.3.1 XPS of As-Received Vanadium Foil and Polished Vanadium Foil

The surface of vanadium was studied by means of core level and valence band XPS. These results represent the surface of vanadium metal after long term oxidation and after polishing the same surface with high grit silicon carbide sand paper. The surface of the as-received vanadium foil was found to be in the 5^+ oxidation state and was found in both the core level and the valence band region to be similar to vanadium pentoxide with small contributions from lower oxidation state vanadium oxides. To analyze the surface at the core level, the V2p and the O1s levels were chosen. Figure 5.1 shows the results of these regions for both samples. The oxygen 1s regions, Figure 5.1(a,b), shows a large change between samples. The as-received sample, Figure 5.1(a), shows a single

intense peak at a binding energy of 531.05 eV with a shoulder at 532 eV. The polished sample, Figure 5.1(b), shows its primary feature at 531.22 eV and this sample shows a more pronounced shoulder at 532 eV and a new feature at 534 eV. The reasons for this can be explained using the V2p region. This region for the as-received sample Figure 5.1(c) can be explained as primarily being $V^{(V)}$ in nature with little contribution from a V^{4+} state or lower. The large peak at 517.9 eV and the feature at 525.1 eV, corresponding to $V2p_{3/2}$ and $V2p_{1/2}$ features, are similar in position to published values for vanadium pentoxide, with the exception of the width of the peaks. The larger width here is also due to contributions from oxidation states lower than that of $V^{(V)}$. This is why the O1s region has primarily a single peak with shoulders due to oxides of lower oxidation state. The shoulders also have contribution from adsorbed species such as CO_2 or O_2. The small feature at 513 eV is the $V2p_{3/2}$ peak due to the vanadium metal below the oxide layer, the small intensity of this peak to the peak at 517.9 eV (V^{Met} vs. $V^{Ox.}$)showing that the oxide layer is thick in nature.

There are more features corresponding to chemically shifted components in the spectra of the polished vanadium sample. The O1s region, Figure 5.1(b), for the polished sample can be compared to the long term oxidized one, Figure 5.1(a). The V2p region, Figure 5.1(d), is dominated by an intense metal peak from the underlying oxide layer, together with features due to the oxidized outer layer. region are due to the metal below the oxide layer. The intense $V2p_{3/2}$ metal peak,is at 513eV and the $V2p_{1/2}$ metal peak is at 520.8 eV. The less intense features at 516.5 eV and 524.3 are due to the oxidized vanadium species present. The large intensity of the metal peak in comparison to the contributions from the oxidized species shows that this is a significantly thinner oxide

layer formed on the surface of the vanadium metal. The binding energy of the oxidized vanadium is lower in the polished sample than the as-received sample indicating the oxidation state is lower, similar to what is seen in VO_2, V_2O_3 and VO.[20-24] Here the oxide that was removed during polishing and the subsequent oxidation of the cleaned vanadium metal sample by atmospheric exposure was slow. Early experiments on vanadium by Pourbaix[25] have shown that theoretically vanadium will oxidize, but experiments he conducted showed that vanadium is more of a noble-type metal that readily adsorbs atmospheric species, agreeing with what is seen here experimentally. The O1s region provides evidence for adsorbed species which can be seen in Figure 5.1(b), as the intense features at 533.7 eV and 532 eV, due to O_2 and CO_2.

The valence band results for the two oxidized samples have been accompanied by the valence band spectra for vanadium pentoxide and a calculated spectra for vanadium metal. These spectra are shown in Figure 5.2(a-d). Figure 5.3 shows the calculated spectra for various vanadium oxides and these have been included to illustrate the expected changes in this region with a change in oxidation state. The vanadium oxides included are: V_2O_5 (a), VO_2 (b), V_2O_3 (c), and VO (d). The calculated V_2O_5 spectrum, Figure 5.3(a), is what is expected with a vanadium oxide with no *d*-electron character, with no features below 3eV. The calculated spectrum is in good agreement with the experimentally collected spectra for V_2O_5, Figure 5.2(a), and for the main features in the as-received vanadium sample, Figure 5.2(b). The main feature in each of these spectra shown between 25-30 eV is primarily O2s in character, with a small contribution from other atomic orbitals. The O2s region is very valuable in distinguishing oxides from other oxidized species such as phosphates, but is less helpful when differentiating

between oxides of the same metal. To do this, the lower region of the valence band (<25 eV) is used. This region has a substantial contribution from O2p and V3s atomic orbitals. The different oxide calculations in Fig. 5.3(a-d) give us an idea of what can be expected as the oxidation state of vanadium varies as the oxidation state changes from the formal $V^{(V)}$ (a)→ $V^{(IV)}$ (b)→$V^{(III)}$ (c)→$V^{(II)}$ (d). As the oxidation state decreases there is a broadening in the valence band below 15 eV. The valence band for vanadium pentoxide, Figure 5.2(a), is in good agreement with its corresponding band structure calculation predicted spectrum, Figure 5.3(a). As the oxidation state decreases to $V^{(IV)}$ the band structure calculation, Figure 2(b), predicts a broadening above 10eV and a broadening toward 0 eV. In experiments by Sawatzky and others, the change in oxidation state from $V^{(V)}$ to $V^{(IV)}$ does cause broadening on the higher binding energy of the O2s-V4s bonding level, but does not actually show broadening of this feature at the lower binding energy side, >3eV.[20-22] The work on these vanadium oxides having d-electron character actually exhibits a separate resolved peak around 1.5eV which is believed to be of primarily d-electron character (electron character is located primarily on the vanadium atom). These band structure calculation use basic STO-3G atomic orbitals which do not create the separation seen experimentally in the $V^{(IV)}$ state. The formal $V^{(III)}$, Figure 5.3(c), and $V^{(II)}$, Figure 5.3(d), oxidation state calculations show the separation.

The as-received sample, Figure 5.2(b), shows a peak at 1.5 eV. This is due to *d*-electron character from any oxides in the surface with oxidation state lower than 5^+ and from the metal below the oxide. This is more evident in the polished sample, Figure 5.2(c), where the feature at 0.5 eV is the most intense in the spectrum. Here the peak is primarily from the metal. This peak is in good agreement with the calculated spectrum,

Figure 5.2(d), for the valence band of the metal. The shoulder on the high binding energy side of the metal peak in the polished sample is due to the *d*-electrons in the oxide layer.

The electronic structure of vanadium has been studied by many calculation methods. The reason for this is vanadium at low temperatures or under extreme pressure has superconductive properties believed to be due to contraction of the crystal lattice. The calculation performed here on the surface of vanadium metal is based on a basis set by Wachters.[19] The band structure diagram for this calculation, Figure 5.4, shows good agreement with those found in the literature.[26-28]

5.3.2 XPS Analysis of the Oxidation of Vanadium Metal by H_2O

In order to analyze how vanadium reacts with water, vanadium was abraded while submerged in triply distilled water which exposes a clean metal surface to reaction with the water. The results from the experiment are shown in Figure 5.5 and Figure 5.6 and are compared to the polished vanadium data. The core level XPS of the O1s region in the water abraded sample, Figure 5.5(a), has shifted to 533 eV as compared to the oxide on the polished sample, Figure 5.5(b). The feature for the polished sample is at 531 eV. The V2p region for the water abraded sample, Figure 5.5(c), is very similar to the polished sample, Figure 5.5(d). The metal features at 513eV and 520.8eV indicating that the layer formed while submerged in water is thinner than the one formed in air. The shifts in the other vanadium features are also similar to the air abraded sample as the main contributions of the vanadium in the coating being from the $V^{(IV)}$ state and lower.

The valence band region for the water oxidized and polished samples are shown in Figure 5.6(a,b) respectively. The main difference here is the presence of hydroxide in

Figure 5.6(a). It is seen as a lowering of intensity at 7eV with the emergence of a more sweeping edge returning to background at 11, where the oxide returns to background at 9eV. The hydroxide characteristically does this as seen in the case of aluminum oxide and aluminum hydroxide. This is also seen in the O*2s* region, Figure 5.6(b), as the peak width has increased with a larger sweeping tail to the higher binding energy side of the peak. These features are indicative of the presence of hydroxide.

5.3.3 Analysis of the Reaction of Etched Vanadium Metal with 5M Phosphoric Acid in an Anaerobic Cell

The first step in this experiment was the argon-ion etching of vanadium metal for 2 hours. This is done in an anaerobic cell at 10^{-3} torr. The etching was done at an acceleration potential of 5 kV and operated at a 2 mA current. After the completion of the etching, the vanadium was then analyzed in the adjoining XPS chamber. The results of this are shown in Figure 5.7. The V*2p* region, Figure 5.7(c), has two peaks which are metallic in shape, at 513 eV for the V$2p_{3/2}$ and 520.5 for the V$2p_{1/2}$, this is in good agreement with the peaks seen in the polished and water abraded samples. The O1s region has two peaks, Figure 5.7(a), due to adsorbed oxygen containing species such as chemisorbed water or carbon dioxide. The low intensity is cause for the high noise in the spectrum.

The metallic shape of the V*2p*, V*3p* and V*3s* (3p and 3s not shown) regions and the low intensity of the O*1s* region give the impression that the oxide has been removed and a metal is present. Upon examining the C*1s* region and the valence band, it can be seen that this is not the case. The C*1s* region Figure 5.7(b) has two features, at 282.6 and

285.3 eV. The higher binding energy peak is due to hydrocarbon. The second peak at 282.6 eV is characteristic of carbide, which was created on the surface during the etching process. In the valence band region Figure 5.7(d) the presence of carbide, vanadium carbide, is also seen as two features at 12 eV and 5 eV. Vanadium carbide has been studied by many methods. The valence band XPS spectrum and corresponding density functional theory (DFT) calculation are reported elsewhere[29] and this work shows strong agreement between the VC spectrum and the spectrum collected for the etched metal here. The calculation and experimental work yield the two strong features at 12eV and 5eV which were of equivalent height and an addition feature at 1.5eV due to the d-electron character. The intensity of the O2s region in the etched vanadium sample at 23 eV is significantly lower then the intensity of the vanadium metal peak at 0.5 eV even thought the photoelectron cross section of the O2s orbital (0.1405) is much greater than the one for V3d (0.0309) and V4s (0.0394), according to Scofield's calculations.[11] This shows that there is a very small contribution in the lower region from oxide if any.

The reason for the lack of signal in the V2p region accounting for the vanadium carbide layer present is that vanadium carbide is metallic. The vanadium signal from the carbide, while vanadium being believed to truly contain one *d*-electron, mirrors the signal from the metal below. The core level V2p reported for VC shows a similar position to that of the metal, the only difference is a slight increase in the width of the features.[29]

The next step was the reaction of this surface to see if a phosphate layer could be grown on the surface. In a previous work it was shown on titanium metal, that the presence of carbide on the surface did not stop the formation of the phosphate layer, rather the strong acid reacted with both the metal and the carbide forming the phosphate

layer, which still contained trace amount of titanium carbide. In this experiment dissimilar results were seen. In two identical and separate experiments, each etching created a thick carbide layer and the reaction of 5M phosphoric acid did form a layer on the surface, but a significantly thinner layer. A result for one of the trial reactions is shown in Figure 5.8 and Figure 5.9.

Figure 5.8 shows the core level spectra for the reacted surface(a,c,d) and the surface of the etched vanadium in the V2p region (b) is also shown for comparison. The O1s and V2p, Figure 5.8(a), for the reacted sample shows a dramatic increase in the O1s region at 530-535 eV when compared to the etched sample. This is understood as the presence of a phosphate on the surface would contribute highly to the O1s signal. The V2p region shows broadening of the two features at 513 and 520.8 eV. This shows some oxidation of the metal surface, but only to very low oxidation state V atoms. The emergence of a weak P2p signal Figure 5.8(c) at 134.7 eV is also evidence of phosphate on the surface. The C1s region, Figure 5.8(d) shows two features almost unaltered from after the etching process, as shown in Figure 5.7(b). The only difference is a slight increase in the peak intensity at lower binding energy, corresponding to an increase in the amount of hydrocarbon on the surface. In the titanium sample the hydrocarbon was present after the etching of the metal, but only the carbide was the significant form of carbon present after the reaction with 5M H_3PO_4.

The valence band gives the same results for the surface, shown in Figure 5.9. Comparing this spectrum with the valence band of the etched sample, Figure 5.7(d), it could be said they are very similar with the exception of a large decrease in the signal from the metal at 0.5eV and an increase in the signal near 15 eV. This is because the

deposition of a new phosphate layer on top of the carbide layer. A slight increase in the signal of the O2s peak is observed, but it also shifts slightly to a lower binding energy, characteristic of a phosphate compared to an oxide or adsorbed oxygen species. The carbide features remain the dominant features in the spectrum at 12 and 4 eV, with slight decrease in the intensity of the feature at 4 eV due to a loss of metal character which has a tail that sweep to 5 eV from its maximum at 0.5 eV.

5.4 Conclusions

Core and valence band XPS is shown to be able to distinguish between the presence of different oxide on the surface of vanadium metal. These valance band spectra and the band structure calculations that support them show that these techniques can distinguish not only between different oxides, but between the presence of other components in the surface such as phosphates, hydroxides or carbides.

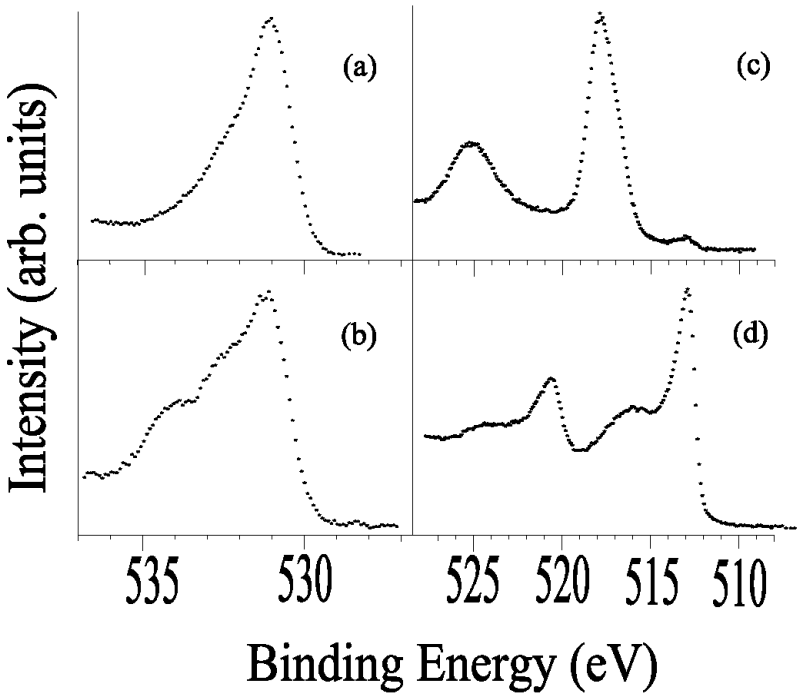

Figure 5.1 The core-level XPS spectra for the O1s (a,b) and V2p (c,d) regions for the as-received sample (a,c) and the polished metal (b,d).

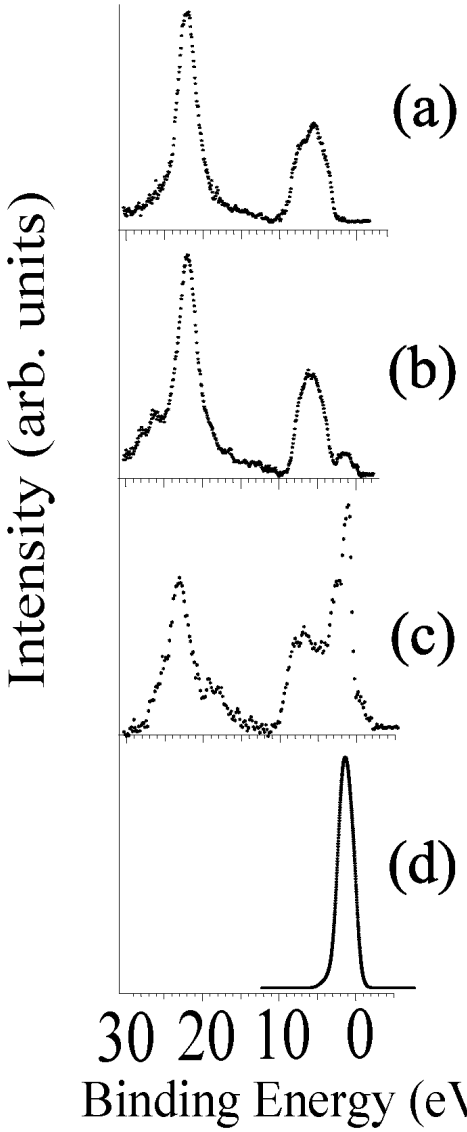

Figure 5.2 The Valence band XPS spectra for vanadium pentoxide (a), the as-received metal (b), the polished metal (c) and a calculated spectra for vanadium metal (d).

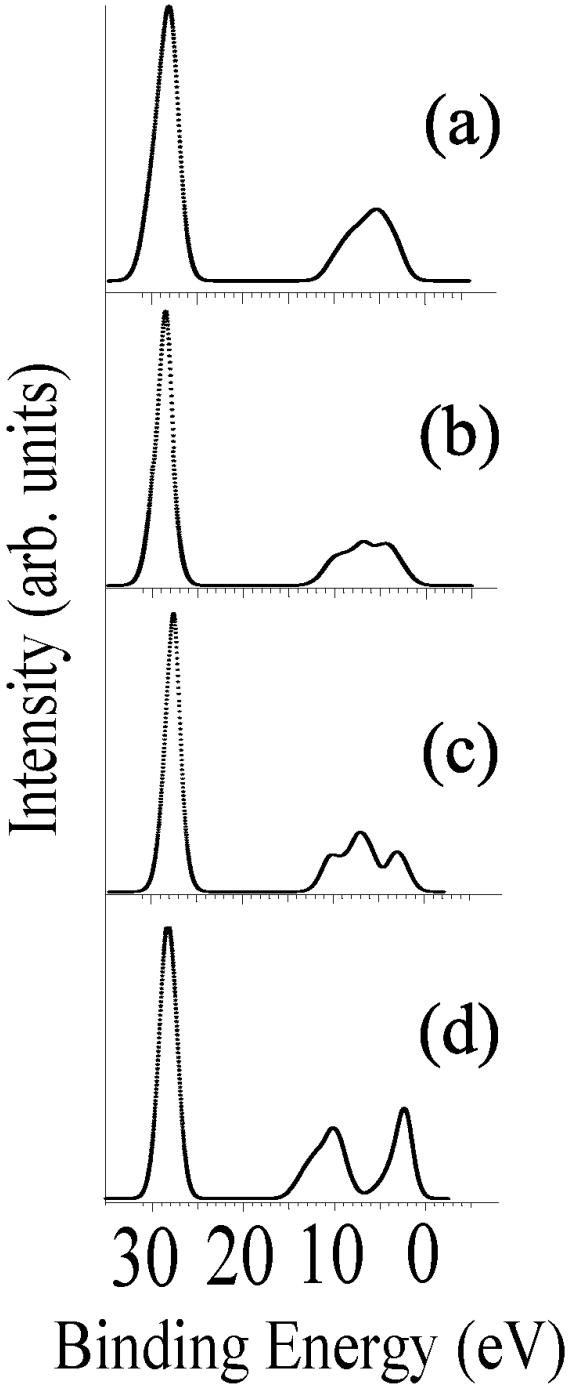

Figure 5.3 The band structure calculated valence band spectra for V_2O_5 (a), VO_2 (b), V_2O_3 (c) and VO (d).

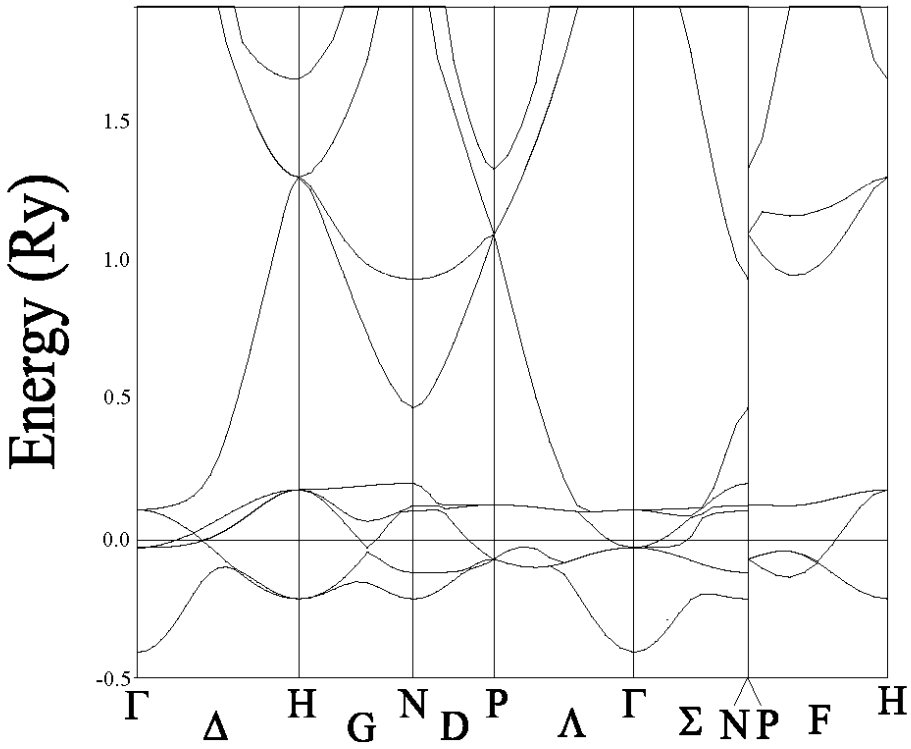

Figure 5.4 The band structure diagram for the vanadium metal calculation.

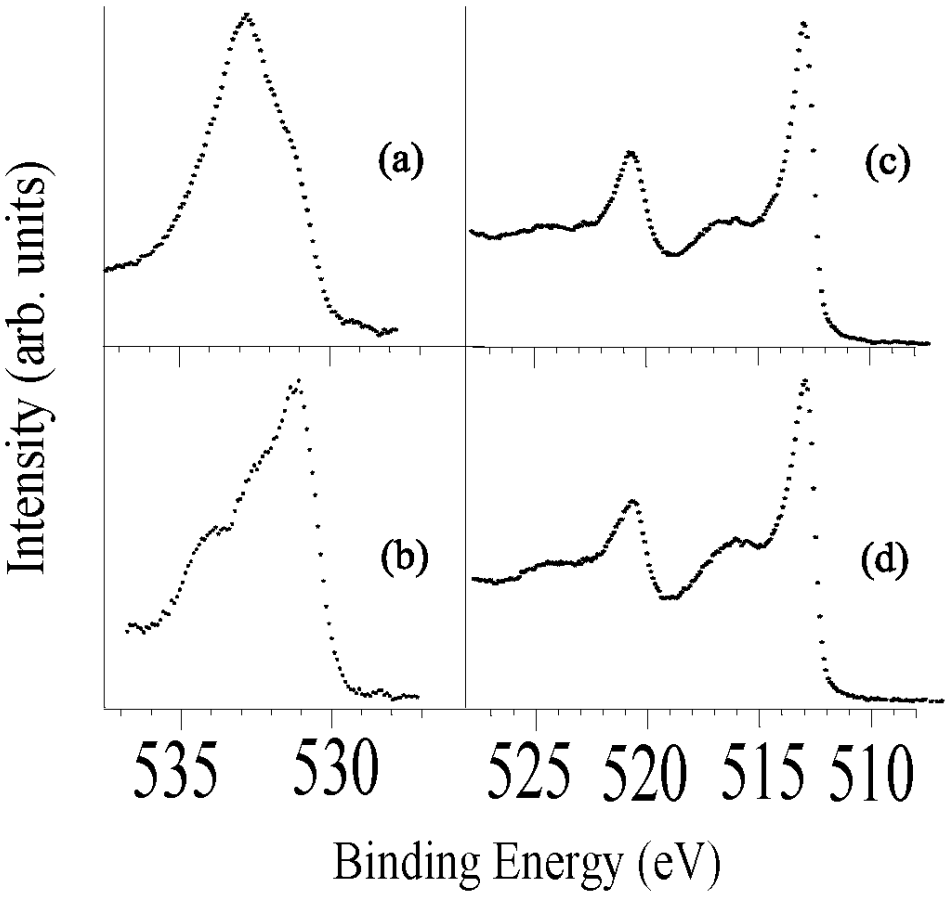

Figure 5.5 The core-level XPS results of the O1s (a,b) and V2p (c,d) regions for the water abraded sample (a,c) and the polished sample (b,d).

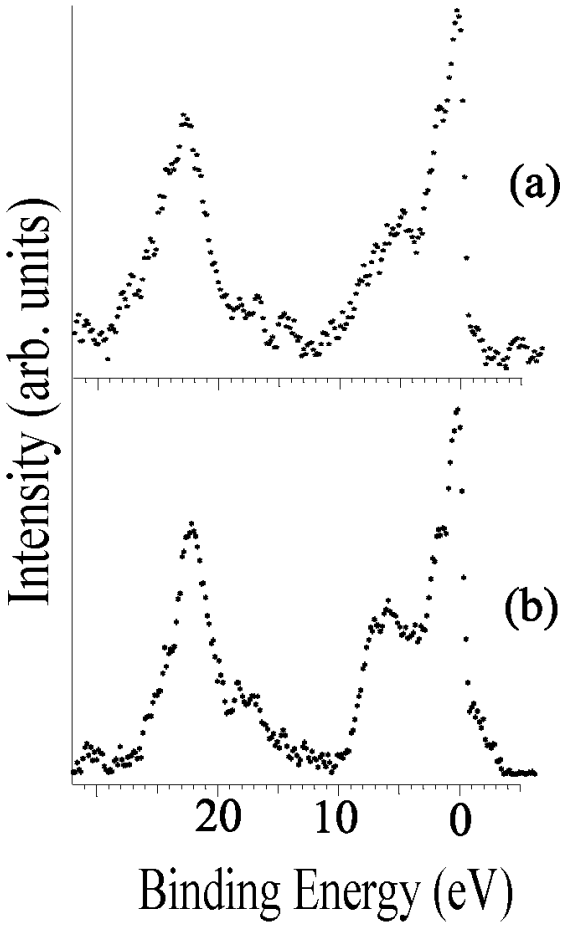

Figure 5.6 The valence band XPS regions for the water abraded sample (a) and the polished metal sample (b).

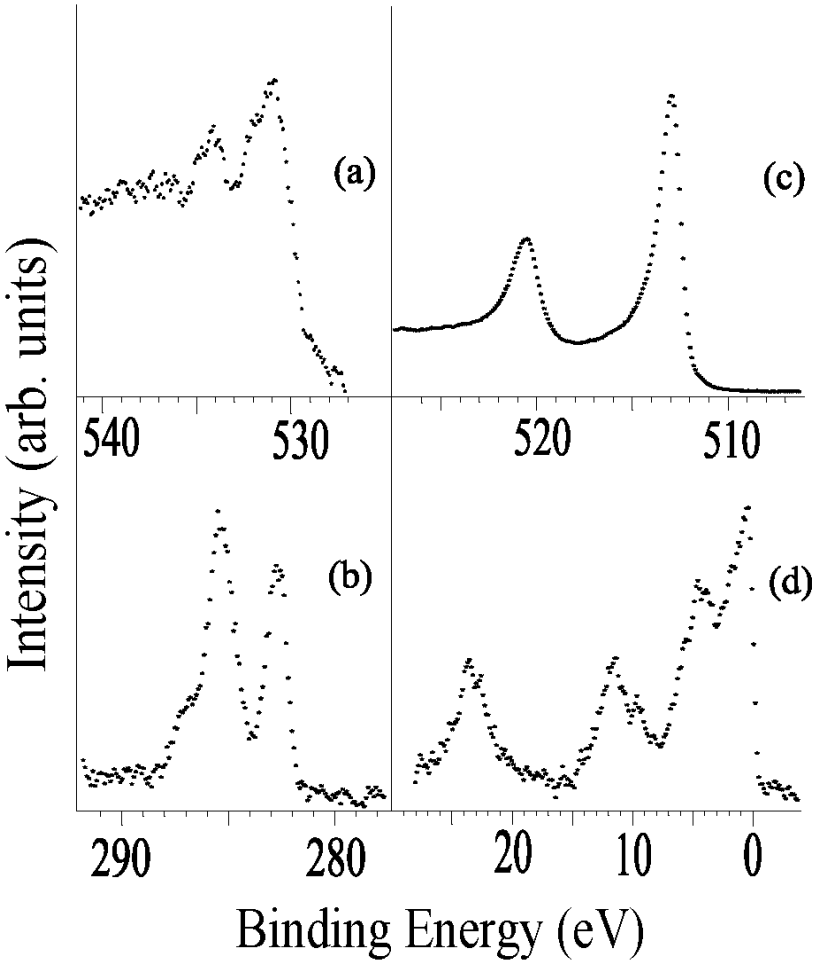

Figure 5.7 The XPS results for the etched vanadium metal, showing the O1s (a), V2p (b), C1s (c) and the valence band (d) regions.

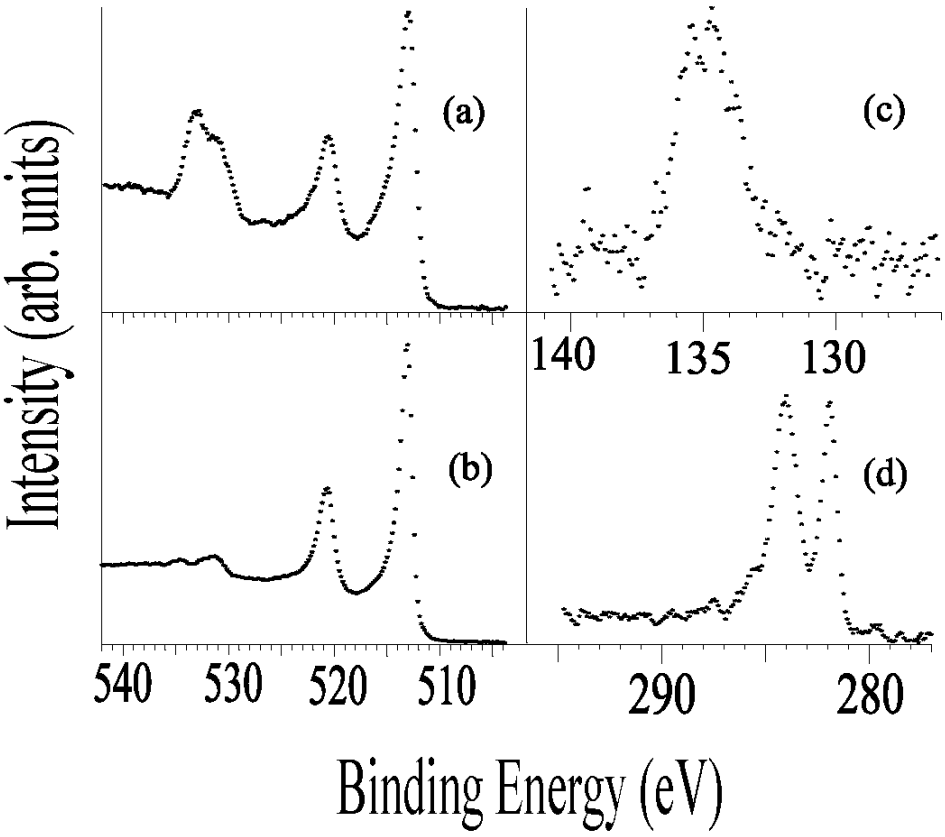

Figure 5.8 The core-level XPS results of the O1s/V2p (a,b), P2p (c), and C1s (d) regions for the anaerobic cell coating (a,c,d), etched metal sample shown for reference (b).

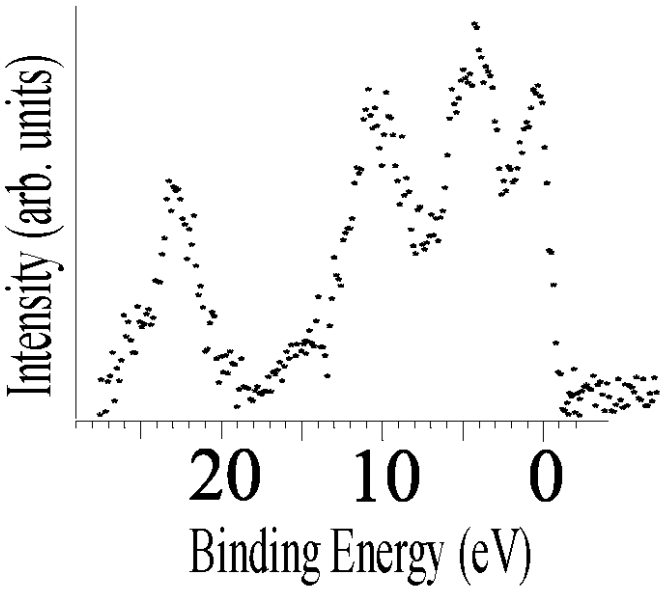

Figure 5.9 The valence band XPS spectrum for the anaerobic cell coated sample.

5.5 References

1. J.A. Rotole and P.M.A. Sherwood, Frenius J. Anl. Chem. **369**, 342-350 (2001).

2. G.D. Claycomb and P.M.A. Sherwood, J. Vac. Sci. Technol. A **20**, 1230 (2002).

3. A.A. Audi and P.M.A. Sherwood, Surf. and Inter. Anal. **33**, 274 (2002).

4. J.A. Rotole and P.M.A. Sherwood, **U.S. Patent No.: 6,066,403** "Metals having Phosphate Protective Films" - May 23, 2000

5. J.A. Rotole and P.M.A. Sherwood, Chem. Mater**. 13**, 3933 (2001).

6. J.A. Rotole and P.M.A. Sherwood, J. Vac. Sci. Technol. A **18**, 1066 (2000).

7. J.A. Rotole , K. Gaskell, A. Comte, P.M.A. Sherwood, J. Vac. Sci. Technol.A **19**, 1176 (2001).

8. C. Pisani, R. Dovesi, and C. Roetti, *Hartree-Fock Ab Initio Treatment of Crystalline systems,* Lecture Notes in Chemistry, 48 (Springer, Rerlin 1988 and QCPE 577).

9. V. R. Saunders, R. Dovesi, C. Roetti, M. Caus, N. M. Harrison, R. Orlando and C. M. Zicovidh-Wilson, *Crystal 98 User's Manual,* 1998, University of Torino, Torino.

10. N.E. Brener, J. Calaway, J.M. Tyler, *Chapter 16. BNDPKG2,* from *Modern Techniques in Computational Chemistry,* 785-803 (1990).

11. J. H. Scofield, J. Electron Spectrosc. Relat. Phenom. **8**, 129 (1976).

12. A. Proctor and P.M.A. Sherwood, Anal. Chem **54**, 13 (1982).

13. P.M.A. Sherwood, J. Vac. Sci. Technol. A, **14**, 1424 (1995).

14. R. Enjalbert, J. Galy Acta Cryst. **C42,** 1467-1469 (1986)

15. F. Theobald, R. Cabala, J. Bernard. J. Solid State Chem. **17**, 431-438 (1977).

16. C.E. Rice, W.R. Robinson. J. Solid State Chem. **21**, 145-154 (1977).

17. R.E. Loehman, C.N.R. Rao, J.M. Honig. J. Phys. Chem. **73**, 1781-1784 (1969).

18. B.M. Vasyutinsky, G.H. Kartmazov, Y.M. Smirnov, V.A. Finkel, Phys. Met. Metall., 21, 134 (1966).

19. A.J.H. Wachters, J. Chem. Phys. **52**, 1033(1970).

20. D.A. Sawatzky, D. Post, Physical Review B, **20**, 1546-1555 (1999).

21. R. Zimmerman, P. Steiner, R. Claessen, F. Reinert, S. Hufner, J. Phys. Condens.

Matter. 11 5697-5716 (1998).

22. R. Zimmerman, P. Steiner, R. Claessen, F. Reinert, S. Hufner, P. Blaha P. Dufek, J. \ Phys. Condens. Matter. 11 1657-1682 (1999).

23. E.Z. Kurmaev, V.M. Cherkashenko, Y. Yarmoshenko, S. Bartkowskii, A.V. Postnikov,

24. S. Shin, S. Suga, M. Taniguchi, M. Fujisawa, H.Kanzaki. Physical Review B, **41**, 4993-5009 (1990).

25. Pourbaix, M. Atlas of Electrochemical Equilibria in Aqueous Solutions. Oxford, New York, Pergamon Press (1966).

26. D.G. Laurent, C.S. Wang, J. Callaway,. Physical Review B, **17**, 455-461 (1978).

27. C. Nimala Louis, K. Iyakutti. Physical Review B, **67**, 1546-1555 (2003).

28. L.L. Boyer, A. Papaconstantopoulos, B.M. Klein. Physical Review B, **15**, 3685-3693 (1977).

29. S.V. Didziulis, K.D. Butcher, S.S. Perry. Inorganic Chemistry, **42**, 7766-7781(2003).

Chapter 6

The Analysis of Three Model Vanadyl Phosphate compounds and the Formation of Potentially Oxide Free Phosphate Coatings on Vanadium Metal

6.1 Introduction

We have previously shown that it is possible to form a novel phosphate layer on metals by reacting orthophosphoric acid with an oxide-free metal surface. This reaction has been shown to produce a thin (<100X) phosphate layer formed directly on the metal without an oxide layer at the interface.[1-4] Such thin, oxide-free films, are interesting because of their potential to act as corrosion inhibiting films, to be adhesion promoting films, and to act as potentially biocompatible surfaces. Phosphated films have proved valuable on metal surfaces, but such films consist of phosphate embedded in oxide films and they are normally of significant thickness (a few thousand Angstroms thick). The thin phosphate films have the benefit of mechanical stability, allowing the metal to be deformed without fracture of the films. These films have been created previously on various metals by using a specially designed anaerobic cell, which can control the environment during reaction.[5] In this work we use an alternate approach to that described in our earlier publications[1-4] which allows the reaction of an oxide-free metal surface with orthophosphoric acid using an approach "on the bench". Full details of this alternate approach have been published separately.[6]

This chapter reports a study of the application of this new approach to form oxide-free phosphate films on vanadium metal. In order to understand the X-ray photoelectron spectra used to investigate this system, we report the investigation of the core and valence

band spectra of various vanadium phosphate compounds. These vanadium phosphates have been studied extensively as catalyst precursors and impurities, but have not been studied using valence band XPS. It will be seen that the XPS valence band spectra can be effectively used to distinguish between the phosphates and oxides that could arise in this system.

6.2 Experimental

6.2.1 Materials and Preparation

6.2.1.1 Synthesis of Three Vanadyl Phosphates

Three vanadium phosphate compounds were synthesized, namely $VO(H_2PO_4)_2$, $VOHPO_4.\ 0.5H_2O$ and $VOPO_4.2H_2O$. One of the compounds, $VOPO_4A2H_2O$, is in the formal (V) oxidation state, while the two other compounds, $VO(H_2PO_4)_2$ and $VOHPO_4A1/2H_2O$, are in the formal (IV) oxidation state. The procedure for synthesizing the compounds used the procedure of Bartley et. al. [16] $VOPO_4.2H_2O$ and that of Kiely et. al.[17] for $VO(H_2PO_4)_2$ and $VOHPO_4.0.5H_2O$. The final products were verified by comparing their X-ray diffraction patterns to the reference patterns in the Powder Diffraction file database.

6.2.1.2 Treatment of vanadium metal to form an oxide-free phosphate layer

We have recently reported[1,6] that it is necessary to have an oxide-free metal in order to form a thin oxide-free phosphate film. We have used our recently reported bench approach.[6] The oxide layer was removed by abrading the as received metal while submerged in deoxygenated 5M orthophosphoric acid. Abrasion was performed using high gret waterproof emery paper. Vanadium Metal (99.0%) was purchased from

Sigma-Aldrich and orthophosphoric acid (85%) from Fischer Scientific was used for the experiment. Scratching to remove the oxide layer lasted ten minutes, which was then followed by ten minutes of reaction time to let the surface of the metal react with the solution. The surface was then rinsed using high purity water and dried in an oven at 110ºC. The 5M orthophosphoric acid solution, vanadium metal sample and emery paper were deaerated for 2 hours prior to beginning the experiment by bubbling nitrogen through the solution. The bubbling was continued throughout the experiment to minimize dissolved oxygen. To perform the polarizing experiments an XXX potentiostat was used to hold the metal a constant value of either ±0.5V versus SCE.

6.2.2 Surface Analysis

All spectra were collected on a VSW HA150 spectrometer (150mm hemispherical analyzer) operated in the FAT (fixed analyzer transmission) mode with a pass energy of 22eV, equipped with a 16 plate multichannel detector system and Al Kα X-radiation (240 W) produced from a 32 quartz crystal VSW monochromator providing an X-ray line width of better than 0.2eV. The base pressure of the instruments was 10^{-9} Torr or better. The spectrometer energy scales were calibrated[7] using an argon-ion etched copper plate. Detailed calibration information, and a discussion of the referencing issues can be found elsewhere.[8-11] Charge corrections were needed for all the phosphate compounds,[9-11] there being no charge correction needed for vanadium metal. A non-linear background was removed from the valence band spectra using the iterative method described previously[12-14]which has been found to be effective in representing the background when fitting short energy range XPS spectra.[15]

6.2.3 Calculations

The calculations in this chapter are either band structure calculations performed using the program CRYSTAL[18,19] or multiple scattered-wave Xα cluster calculations. The calculation for tetragonal *P4/ncc*[22] $VO(H_2PO_4)_2$ was performed using an optimized basis sets for the oxygen and vanadium atoms and an unrestricted Hartree-Fock model to account for the one unpaired electron. The calculations are conducted to produce separate density of states contributions for each orbital type. The density of states is then adjusted using the appropriate photoelectron cross sections of Scofield.[23] The adjusted density of state is then convoluted with a Gaussian/Lorentian product function[13,24] that represents the photon function.

The cluster calculations[25], performed using multiple scattered-wave Xα calculations, were carried out on PO_4^{3-}, HPO_4^{2-} and $H_2PO_4^{-}$. In these calculations, the charged ions are rendered neutral by placing a "Watson sphere" about the ion with a charge that exactly balances the ionic charge. The atomic positions for the ions were found from the diffraction data available for each of the three previous synthesized compounds.[21,26,27] A list of the parameters used is listed in Table 6.1. The calculated spectrum was generated by adding together the component peaks for each of the calculated energy levels, with each peak having a position corresponding to the calculated energy level and an intensity (area) corresponding to the number of electrons in the energy level multiplied by the atomic population for the level, adjusted by the appropriate atomic photoelectron cross-section using values due to Scofield.[23] Each

component in the calculated spectrum was represented by an equal full width at half-maximum (2 eV) 50% Gaussian/Lorentzian product function peak.[13,24]

The separation between the outer valence band region (0-14 eV) and the inner valence band region (around 25 eV) typically shows slight differences between theory and experiment, these differences being dependent upon the basis set used for the band structure calculation and the parameters chosen for the Xα calculation. The spectral appearance in spectra generated from Xα cluster calculations depends upon the width chosen for the component features. We choose the width of each component to be the same. It is true that better agreement could be achieved using variable widths, but we do not have a suitably accurate method of accounting theoretically for all the differences in widths which we know to occur as a result of differences in vibrational broadening and other features. "Fitting" the widths to experiment was avoided as this would give a "calculated" spectrum that was not really calculated, but rather a mixture of fitting and calculation.

6.3 Results and Discussion

6.3.1 Model Phosphate Compounds

Before discussing the formation of oxide-free phosphate films on vanadium it is useful to discuss the valence band spectrum that would be expected for vanadium phosphate. The valence band XPS spectra of three vanadium phosphates will now be discussed. These spectra provide a useful idea of how the valence band spectra of vanadium phosphates appear, and will be used for comparative purposes below. The compounds chosen vary in the formal oxidation state of vanadium, and in the type of

phosphate ion. Thus three types of phosphate, an orthophosphate, a hydrogen phosphate and a dihydrogen phosphate were examined, namely $VO(H_2PO_4)_2$ (V(IV)), $VOHPO_4.0.5H_2O$ (V(IV)) and $VOPO_4.2H_2O$ (V(V)).

6.3.1.1 Core Level XPS

Figure 6.1 shows the P2p, O1s, and V2p core level XPS data for the three phosphates. The P*2p* spectra (d-f) of all three phosphates appear similar slightly shifting to higher binding energy with increase in the number of hydrogen atoms bound to the phosphate. The O1s region (a-c) shows significant differences as does the V2p region. All of these regions will be discussed in more details below.

The O1s region, Figure 6.1(a), can be understood if one notes the differences in the different phosphate ions. $VOPO_4{\cdot}2H_2O$ can be understood in terms of a $(VO)^{3+}$ ion and a PO_4^{3-} ion. The latter ion is a tetrahedral ion with all four oxygen atoms equivalent. The O1s region shows a single peak at 531 eV, indicating that both the phosphate oxygen atoms and the $(VO)^{3+}$ oxygen atom are in equivalent environments. The P2p peak, Figure 6.1(d), for this compound also shows a single peak at 134.2eV.

$VOHPO_4.0.5H_2O$ can be understood in terms of a $(VO)^{2+}$ ion and a PO_4H^{2-} ion. The latter ion has one P-OH oxygen and three PO oxygen atoms (two having a slightly shorter bond length than the other oxygen atoms - see Table 6.I). Thus one would expect two types of oxygen environment a P-OH feature at higher binding energy, and a P-O feature at lower binding energy in the ratio 1:3. The P-O feature could be slightly split in the ratio 1:2 corresponding to the two P-O oxygen environments. The P2p peak for this compound, Figure 6.1(e), shows a single peak now shifted to 134.6eV showing the slight loss of electron character at the phosphorus due to the hydrogenation of the phosphate ion.

$VO(H_2PO_4)_2$ can be understood in terms of a $(VO)^{2+}$ ion and two $PO_4H_2^-$ ions. The latter ion has two P-OH oxygen and two PO oxygen atoms. Thus one would expect two peaks in the O1s region of equal intensity which is seen in Figure 6.1(c). The continued addition of hydrogen to the phosphate ion is also seen in the P2p region, Figure 6.1(f), as the peak has shifted to a more electro-positive 134.9eV.

The V2p region can be understood in terms of the differences in the V2p chemical shift. The formally V(V) phosphate, $VOPO_4{\cdot}2H_2O$, shows the higher binding energy $V2p_{3/2}$ feature at 518.5 eV. The formally V(IV) phosphates $VOHPO_4.0.5H_2O$ and $VO(H_2PO_4)_2$ show lower binding energy $V2p_{3/2}$ features at 517 and 516.6 eV. It can also be seen that this peak is broader for V(IV) than it is for V(V). These binding energy observations are compatible with previous studies of the core peaks in vanadium oxides.[28] Multiplet splitting is the V2p region has been studied in the various vanadium oxides. The overwhelming difficulty in making concrete determinations in this region is due to spectral overlap where the satellite features are to be seen. The satellite feature for the $V2p_{3/2}$ peak predicted by several authors occurs where the feature for the $V2p_{1/2}$ peak is and similarly, the satellite for the $V2p_{1/2}$ occurs in the region dominated by the O1s feature. These satellite features are predicted to be very weak in the V2p region which also makes their study very difficult. This is not the case for the V3p region as the multiplet splitting for these features is very strong.

The V3p peaks for the three compounds, Figure 6.2, show distinct characteristics in this region, which make this the strongest region for multiplet splitting study. The large signal observed in the satellite features is seen due to the strong 3p-3d coupling. The relatively small energy gap between these regions lends to the large intensity of the

satellite seen in comparison to the 2p region. The formal V(V) $VOPO_4 \cdot 2H_2O$ compound, Figure 6.2(a), shows a single peak centered at 42.3eV. The formal V(V) V_2O_5's V3p spectrum, Figure 6.2(b), is shown for comparison, showing agreement with the peak shape and location to that of $VOPO_4 \cdot 2H_2O$. These compounds should have a single feature as there are no electrons occupying the 3d level to couple with a core-hole state. The two formal V(IV) compounds, $VOHPO_4 \cdot 0.5H_2O$ and $VO(H_2PO_4)_2$, Figure 6.2(c,d), show strong satellite features, but each has a slightly different energy shift. The main V3p feature is present in these spectra at 41.1 and 40.6eV and the peaks to the higher binding energy are the satellite feature. The shifts seen are 2.2eV and 2.5eV for $VOHPO_4 \cdot 0.5H_2O$ and $VO(H_2PO_4)_2$, respectively. A third feature, or second satellite feature is believed to be located between 10-12eV shifted to higher energy of the main feature. The experimental results for these compounds only a slight feature in this region, perhaps due to the low intensity of the satellite feature. There has been extensive work into the multiplet splitting of vanadium oxides, trying to explain the results seen in all of the core regions of vanadium. These compounds agree with what is seen in the studies of the vanadium oxides, but there are differences due to the bonding at the vanadium atom. The various oxides have been studied to show that there is significant hybridization between the vanadium atom and its surrounding oxygen atoms. This idea is tied to the length of the bonds between the vanadium and the oxygen. In the oxides the shortest bond length between the vanadium and the closest oxygen increases as the oxidation state decreases. The formal V(V) V_2O_5 has one V-O bond length of 1.58Å and the others are greater than 2 Å. This distance is very small and covalent bonding could be expected between the oxygen and vanadium, but no valence electrons exist in the formal V(V)

oxidation state. The absence of satellite features in this oxide shows that the vanadium remains unoccupied in the valence levels. The formal V(IV) oxide, VO_2, has the valence electron, but the bond length of the shortest V-O bond is 1.71Å, much greater than in the vanadium pentoxide. The length increases in the formal V(III) oxide, V_2O_3, to a large 1.96eV. The studies on these oxides show that there is still some hybridization in these oxides, and that the amount of hybridization can be seen in the structure and shifts of the multiplet split peaks. The two formal V(IV) state compounds studied here, $VOHPO_4 \cdot 0.5H_2O$ and $VO(H_2PO_4)_2$, show a larger splitting in the V3p region than that of the oxide of the same oxidation state. This is directly related to the shorter bond length of the V-O in the vanadyl species. The V-O bond lengths are 1.60Å and 1.69Å for $VO(H_2PO_4)_2$ and $VOHPO_4 \cdot 0.5H_2O$, respectively. Both are smaller than that of VO_2, with $VOHPO_4 \cdot 0.5H_2O$ just being slightly longer, and the shift slightly larger. The vanadyl dyhydrogenphosphate is significantly shorter and the shift is then seen as a a resolvable second peak rather than a shoulder.

6.3.1.2 Valence Band XPS

6.3.1.2.1 $VOPO_4.2H_2O$: The valence band spectrum for $VOPO_4.2H_2O$ and the corresponding calculated spectrum generated from a multiple scattered wave Xα calculation for the tetrahedral orthophosphate ion are shown in Figure 6.3(a, b) respectively. The most intense feature in the experimental valence band spectrum is centered at 23.6eV and has a shoulder at 27eV. The valence band spectrum can be understood if one notes that the $(VO)^{3+}$ ion would be expected to have little contribution in the valence band region from the formally V(V) vanadium atom - which if completely ionic would have no valence electrons. The oxygen part of the $(VO)^{3+}$ ion would make a

contribution in the O2s region around 25 eV. The remainder of the spectrum can be understood by comparison with the spectrum expected for the orthophosphate ion which is shown in Figure 6.3(b). The asymmetrical nature of the region from 20 to 30 eV is well explained by the two calculated features "1" and "2" in Figure 6.3(b). Feature "1" has considerable P3s character (22% P3s and 77% O2s character) while feature "2" is largely O2s with some P3p character (10% P3p and 88% O2s character). The remaining character is represented by a small amount of O2p.

The valence band region below 15 eV binding energy shows the two characteristic features of the orthophosphate ion, a peak a 14 eV (peak "3") and a peak at 11 eV (peak "4"). Peak "3" has substantial P3s character (27%) with O2p (59%) and O2s (14%) character. Peak "4" has substantial P3p character (21%) with O2p (31%) and O2s (48%) character. The high symmetry of the phosphate ion prevents any P3p character in peak "3" and any P3s character in peak "4". The remaining peaks ("5", "6" and "7") are almost entirely of O2p character. Any small vanadium contribution would be in the region of the "5", "6" and "7" features with a binding energy below 9eV. We confirmed this by conducting a cluster calculation on the VO^{2+}, a species that has one vanadium d electron, which showed a 90% V 3d feature below 9 eV.

6.3.1.2.2 $VOHPO_4.0.5H_2O$*:* The valence band spectrum for $VOHPO_4.0.5H_2O$ and the corresponding calculated spectrum generated from a multiple scattered wave Xα calculation for the PO_4H^{2-} ion are shown in Figure 6.3(c, d), respectively. Again the most intense feature in the experimental valence band spectrum is centered at 25eV and has a shoulder at 28eV. The valence band spectrum can be understood if one notes that the $(VO)^{2+}$ ion would be expected to have little contribution in the valence band region

from the formally V(IV) vanadium atom - which if completely ionic would have one valence *d*-electron. The oxygen part of the $(VO)^{2+}$ ion would make a contribution in the O2s region around 25 eV. The remainder of the spectrum can be understood by comparison with the spectrum expected for the PO_4H^{2-} ion which is shown in Figure 6.3(c). The experimental feature (Figure 6.3(c)) centered at 25eV has a shoulder at 27eV and is represented by four component energy levels in the calculated spectrum (Figure 6.3(d)). The added width of this region in the PO_4H^{2-} ion compared with the PO_4^{3-} ion can be understood because the fall of symmetry from T_d to C_s leads to more levels so the triplet in the PO_4^{3-} ion becomes three singlets in the PO_4H^{2-} ion. P3s and P3p character and mainly O2s character are the main components of this region with the lowered symmetry leading to P3p character over all the peaks and including the high binding energy feature “1" which now shows 11.5% P3p and 4.3% P3s character. The feature at highest binding energy “1” is also predominantly associated with the P-OH oxygen atom.

The valence band region below 15 eV binding energy shows a high binding energy feature around 14.5 eV (corresponding to the singlet peak “5” of A’ symmetry) which unlike the corresponding feature (an A_1 singlet) in the orthophosphate ion (which was only P3s and O2p) contains substantial P3p character (11.6%P3p and 3.6% P3s). Thus the lowered symmetry of the PO_4H^{2-} ion causes substantial differences in the molecular orbital compositions which lead to differences in binding energy and intensity (since the latter is very dependent upon the mix of atomic orbitals with different photoelectron cross sections into the molecular orbitals). About 63% of peak “5” represents contributions from the oxygen atom in the P-O-H bond. The P-O bondlength

is 1.586Å as opposed to the three remaining shorter P-O bonds (1.491Å (x2) and 1.560 Å). The peak at 11 eV now shows some structure. This too would be expected since the T_2 feature in the orthophosphate is now replaced by singlet features at different energy (peaks "6", "7" and "8") consisting of a mixture of P3s ("6" and "8" only). The remaining features have very substantial O2p character, but the lowered symmetry leads to a significant amount of P3p character as well. Any small vanadium contribution would be in the region with a binding energy below 9eV.

6.3.1.2.3 $VO(H_2PO_4)_2$: The valence band spectrum for $VO(H_2PO_4)_2$ and the corresponding calculated spectrum generated from a multiple scattered wave Xα calculation for the PO_4H^{2-} ion is shown in Figure 6.4(b) and (c) respectively. Figure 6.4(a) shows the spectrum calculated from a band structure calculation. The most striking feature in the calculated spectrum of the PO_4H^{2-} ion is the doublet feature around 25 eV. The two peaks correspond to oxygen intensity from the POH oxygen atoms (peaks "1" and "2") and PO oxygen atoms (peaks "3" and "4"). The experimental spectrum certainly shows a broad feature in this region, though it cannot be resolved into two components. The different symmetry leads to a significantly different spectrum which agrees well with the calculated spectra. The spectrum obtained from the band structure calculation (Figure 6.4(a)) identifies a weak feature located around 0 eV which is comprised primarily of V3d character, which can be identified in the experimental spectrum (Figure 6.4(b)) around 2.5 eV. The $VOPO_4 \cdot 2H_2O$ (Figure 6.3(a)) does not show this feature as this is a V^{5+} compound which has no significant V *d*-electron contribution. In an effort to further explore these species, Xα calculations for the vanadyl species in the V^{4+} and V^{5+} state.

The predicted valence bands for the two species are shown in Figure 6.4. The V^{5+} state, Figure 6.5(a), shows three features. There is a large single peak for the O*2s* contribution at 19 eV. The two features at 4 and 6 eV are primarily due to O*2p* contribution. The vanadium as stated before has no d-electron contribution, so these results mirror what was predicted previously. The V^{4+} species, Figure 6.5(b), has three features, but is significantly different. The O*2s* region has not changed, but the lower region has. The contribution from the O*2p* orbital is centered at 4.9 eV is one single peak as compared to the two features in the V^{5+} species. The last feature, at 1.8 eV, is due to the *d*-electron contribution. This peak is predominantly V*3d* in character. In the band structure calculations for the vanadium oxides, a resolvable feature for the presence of d-electrons could not be seen until an optimized basis set for the vanadium atom was used. These calculations indicate, as was hoped, that the contribution from this species was below 9eV. This agrees with the assertions that the region between 10-16 eV will be mostly phosphate in nature, allowing for study of the structure of the phosphate to be done in this region.

6.3.2 Oxide-Free Phosphate Coating on Vanadium Metal

We applied the treatment method described above to form a thin, oxide-free phosphate layer on vanadium metal. The core level and valence band spectra are shown in Figure 6.5. The O1s region, Figure 6.6(a), shows the doublet feature seen in $VO(H_2PO_4)_2$ (Figure 6.1(c)). The V2p region shows two features, one due to the underlying metal (peaks B and D) and one due to the phosphate layer (peaks A and C). The $V2p_{3/2}$ feature corresponds to metal at 513 eV and oxidized vanadium at 518 eV.

The single P2p feature at 135.4 eV is similar in binding energy shift as that of $VO(H_2PO_4)_2$ (Figure 6.1(c)). The valence band region Figure 6.6(d) shows a spectrum that is very close to that of $VO(H_2PO_4)_2$. In an effort to better understand why there are differences between the valence of $VO(H_2PO_4)_2$ and the coating on the metal, curvefitting was performed on the V*2p* region for the coating.

Figure 6.7 shows the curvefitting of the V*2p* region for the coated metal (a), $VOPO_4{\cdot}2H_2O$ (b), $VO(H_2PO_4)_2$ (c) and the etched metal (d). There are several things to note when considering the results for the curve fitting of the coated metal. The results can not be taken as exact quantitative results as major assumptions have been made. There has been no consideration of any oxidation state lower than 4^+ which as shown in an oxidized sample can form. The etched vanadium metal region actually has carbide on it which, even though metallic, slightly broadens the peaks. Also, significant noise in the spectra makes an exact match impossible.

The $VOPO_4{\cdot}2H_2O$ (b), $VO(H_2PO_4)_2$ (c) and the etched metal (d) serve as reference, used to determine the shape of the peaks in the coated sample. The $VOPO_4{\cdot}2H_2O$ spectrum shows the vanadium in the 5^+ state, which shows reasonable agreement. The Peaks have been determined to have a coster-kronig broadening giving a 1:2 width ratio between the $V2p_{3/2}$:$V2p_{1/2}$. The $VO(H_2PO_4)_2$ shows the vanadium in the 4^+ oxidation state. Here the broadening of the vanadium peaks is 1:1.4. The broadening in the metal spectrum was 1:2, but this is made less evident because of the shape of the metal peak. To accommodate for the sweeping metallic tail, an exponential tail was added to the Gaussian/Lorentzian peak.

The coated metal spectra Figure 6.7(a) is made of a combination of these three spectra. This explains the broadening seen in the V$2p_{3/2}$ region for the coating and also explains the in decrease in the peak at 5 eV in the valence band spectrum of the coating, Figure 6.6(d). The reason for the decrease as compared to $VO(H_2PO_4)_2$ is because of the presence of a significant amount of V^{5+}, which changes the amount of phosphate counter ion, increasing the amount of phosphate. A change in oxidation state will change the basic formula from $VO(H_2PO_4)_2$ to $VO(H_2PO_4)_3$ and as shown from Xα calculation and band structure calculations increase on phosphate concentration will be seen in the peaks at 10 and 14, and the decrease will be seen in the vanadyl region at 5 eV. The relatively low height of this region also is a sign of the lack of oxide present in the coating or at the interface.

One might consider some very thin layer of oxide at the interface between the metal and the phosphate layer. We do not believe that this is the case for two reasons. The first reason is that in all our experiments on forming these oxide-free phosphate films, the presence of any oxide prevents the formation of the phosphate layer; the key aspect of the process being the interaction of the oxide-free metal with the orthophosphoric acid. The second reason is that the presence of any oxide, such as V_2O_5 in the film would change the relative intensity of the region between 20eV and 30eV and that between 0 and 20 eV whereas we find that these intensity ratios are within 95% of one another. Any oxide would also significantly change the appearance of the region between 0 and 20 eV, in particular adding significant intensity in the region between 5 and 7 eV. No such changes are seen and we conclude that there is no significant oxide in the films.

6.3.3 Effect of Polarizing the Vanadium Metal on the Reaction with Phosphoric Acid

It has been previously reported that it is possible to control the thickness of a formed oxide layer on the surface of aluminum metal by polarizing the metal at the time of reaction with a solution of nitric acid. With this in mind, the effect of polarizing the vanadium metal during reaction with H_3PO_4 was studied at polarizing potentials of +0.5V, unbiased and -0.5V. The results of this study indicate similar results to what was in the oxidation of aluminum metal. The results for the experiment are shown in figures 6.8 and 9. Figure 6.8 shows the core level XPS data for the V2p (I), O1s (II) and P2p (III) regions for the -0.5V bias, no bias and +0.5V bias samples. (a,b,c respectively) The "-" biased sample shows a similar trait to what was seen in the aluminum experiment as the coating is thinner with the negatively applied potential. The signal for the metal's $V2p_{3/2}$ (512 eV) peak for the -0.5V bias sample, I(a), is stronger than the unbiased sample, I(b), and conversely the $V2p_{3/2}$ contribution for the vanadium in the coating (518 eV) is stronger in the unbiased sample. The application of the negative bias has lessened the reactivity of the vanadium metal surface. It has also affected the oxidation state of the vanadium in the coating and lead to some interesting observations. The metal reacted to form a coating, which contains contribution from vanadium in lower oxidation states, which must have been stabilized by the application of the bias. The contribution is seen as a shift in the $V2p_{3/2}$ feature for this coating to 517.5 eV from 518.5 eV for the unbiased sample. The positively biased sample is the thinnest coating of the three, but this coating is believed to be primarily oxide due to the low intensity of the phosphorus in the spectra and by the features seen in the other regions.

The O1s and P2p regions for the samples indicate the nature of the formed phosphate film. The shift of the P2p feature and the shoulder in the O1s indicate whether the phosphate is orthophosphate or hydrogen/dihydrogenphosphate. The unbiased sample shows a P2p feature (Figure 6.8(III(b)) at 135.3 eV and an O1s at 534.1 eV. The most intense feature for the unbiased sample in the O1s region is due to the protonated oxygens, showing that the biasing caused a shift in the negatively biased sample's O1s to 532.4 eV. This indicates that the phosphate seems to be less-protonated, resembling the hydrogenphosphate in peak structure. The main O1s feature now has a small shoulder at 534 eV where the hydroxide feature is found. The shift of the P2p feature to 133.7 eV is also similar to what was seen with the three model compounds indicating a shift to a less-protonated phosphate ion. In the positively biased sample, the spectra indicate that there is little presence of phosphate and large content of vanadium oxides. The intensity of the P2p feature is very low in comparison to other coatings, which creates the noise seen in the spectrum, III(c). The weak feature at 134.3eV indicates that there does exist some phosphate in the coating and the position of the peak tells that it is most similar to in the less-protonated form. The O1s spectrum shows the presence of the oxides. The position for the most intense feature in the O1s region at 532.3eV for the positively biased sample is similar to the negatively biased sample, but there is much less intensity near 534 eV in the spectrum and a new feature exists at 531.5 eV which is characteristic of oxides. The shifting of the majority of the intensity in the spectrum to lower binding energy indicates that the coating formed is primarily oxide.

The valence band region for these samples, Figure 6.9, shows the same trend. The valence band of the negatively biased sample, Figure 6.9(a), showed an increase in

the region from 5 to 8 eV as compared to the unbiased sample. This is very similar to the shape of the vanadium hydrogenphosphate seen in Figure 6.3(c). The separation between the 2 phosphate peaks in the valence band also shows that this is similar to the vanadium hydrogenphosphate spectra. The slight decrease in separation is also characteristic of the change from the dihydrogenphophate to the hydrogenphosphate. The metal feature at 1 eV is more intense for this coating than the unbiased coating, Figure 6.9(b), showing that it is thinner. The positively biased sample, Figure 6.9(c), has the most intense feature here making it the thinnest coating, which is what was seen in the core-level V2p spectra. The position of the O2s feature at 23eV for the positive biased sample indicates the same shift as the core O1s region, further showing evidence of oxide. There is a small shoulder at 25eV corresponding to the small contribution from the phosphate trapped in the oxide layer. This shoulder is similar to the main O2s features in the unbiased and negatively biased samples, Figures 6.9(b,a).

6.4 Conclusion

This work indicates that it is possible to generate oxide-free phosphate films on vanadium metal. This is the first case where we have formed phosphate films that are "oxy-phosphate", all the films having the $(VO)^{3+}$ or $(VO)^{2+}$ species present. Core and especially valence band XPS can be seen to be able to distinguish between different phosphate species of vanadium, and between phosphates of vanadium and oxidized vanadium. The changes in the phosphate valence band that arise when the phosphate ion changes from the highly symmetrical orthophosphate to the much less symmetrical hydrogen phosphates can be understood by examining the changes in the valence band

spectra and comparing these changes with spectra generated from multiple scattered wave X cluster calculations. The valence band spectra can be effectively interpreted by spectra generated from band structure calculations proving to be an effective method for the analysis of the data.

6.5 References

1. J.A. Rotole and P.M.A. Sherwood, **U.S. Patent No.: 6,066,403** "Metals having Phosphate Protective Films" - May 23, 2000

2. J.A. Rotole and P.M.A. Sherwood, Chem. Mater. **13**, 3933 (2001).

3. J.A. Rotole and P.M.A. Sherwood, J. Vac. Sci. Technol. A **18**, 1066 (2000).

4. J.A. Rotole , K. Gaskell, A. Comte, P.M.A. Sherwood, J. Vac. Sci. Technol.A **19**, 1176 (2001).

5. Y. Liang, D. Paul, Y. Xie, and P.M.A. Sherwood, Anal. Chem. **65**, 2276 (1993).

6. Y-Q Wang and P.M.A. Sherwood, J. Vac. Sci. Technol. A, **21**, in press.

7. M.P. Seah, I.S. Gilmore, G. Beamson. Surf. Interface. Anal. **26,** 642 (1998).

8. P.M.A. Sherwood, *Surface Science Spectra*, submitted for publication.

9. D.J. Asunskis and P.M.A. Sherwood, *Surface Science Spectra*, submitted for publication.

10. D.J. Asunskis and P.M.A. Sherwood, *Surface Science Spectra*, submitted for publication.

11. D.J. Asunskis and P.M.A. Sherwood, *Surface Science Spectra*, submitted for publication.

12. R.O. Ansell, T.Dickinson, A.F.Povey and P.M.A. Sherwood , J Electroanal Chem **98**, 79 (1979).

13. P.M.A. Sherwood, in *Practical Surface Analysis by Auger and X-ray Photoelectron Spectroscopy*; Edited by D. Briggs and M.P. Seah (Wiley, New York, 1983) Appendix 3.

14. A. Proctor and P.M.A. Sherwood, Anal. Chem **54**, 13 (1982).

15. P.M.A. Sherwood, J. Vac. Sci. Technol. A, **14**, 1424 (1995).

16. J. K. Bartley, R.P.K. Wells, G.J. Hutchings, J. Catal., **195**, 423 (2000).

17. C.J. Kiely, A. Burrows, S. Sajip, G.J. Hutchings, M.T. Sananes, A. Tuel, J. Volta, J. Catal., 162, 31 (1996).

18. C. Pisani, R. Dovesi, and C. Roetti, *Hartree-Fock Ab Initio Treatment of Crystalline systems,* Lecture Notes in Chemistry, 48 (Springer, Rerlin 1988 and QCPE 577).

19. V. R. Saunders, R. Dovesi, C. Roetti, M. Caus, N. M. Harrison, R. Orlando and C. M. Zicovidh-Wilson, *Crystal 98 User's Manual,* 1998, University of Torino, Torino.

20. R. Enjalbert, J. Galy Acta Cryst**. C42,** 1467-1469 (1986).

21. W. C. Mackrodt, N.M Harrison, V.R. Saunders, N.L.Allan, M.D. Towler, E. AprB and R. Dovesi, Phil Mag A. **68**, 653 (1993).

22. S.A. Linde. Y.E. Gorbunova. A.V. Lavrov. V.G. Kuznetsov. Doklady Akademii Nauk SSSR **244**, 1411-1414 (1979)

23. J. H. Scofield, J. Electron Spectrosc. Relat. Phenom. **8**, 129 (1976).

24. R. O. Ansell, T. Dickinson, A. F. Povery, and P.M.A. Sherwood, J. Electroanal. Chem**.** 98**, 79** (1979)

25. D.A.Case. Ann Rep. Phys. Chem. **33**, 151 (1982).

26. H. R. Tietze. J. Australian Chem. **34**, 2035 (1981).

27. M. E. Leoniwicz. J.W. Johnson. J.F. Brody. H.F. Shannon. J.M. Newsam. Journal of Solid State Chemistry **56**, 370-378 (1985)

28. D.A. Sawatzky, D. Post, Phys. Rev.B, **20**, 1546 (1999)

Table 6.1 Parameters used and features of the Xα calculations

α values: phosphorus, 0.72620; hydrogen, 0.77654; oxygen, 0.74447
Maximum *l* values: Outer 4; phosphorus 4; oxygen 1; hydrogen 0 Hydrogen Sphere Radius=0.37Å

Cluster	PO_4^{3-}	PO_4H^{2-}	$PO_4H_2^-$
Symmetry	T_d	C_s	C_{2v}
P-O Bondlengths	1.56Å	1.543Å- PO(1) 1.491Å -PO(2) 1.586Å- POH	1.500Å PO(2) 1.570Å POH(2)
O-H Bondlengths	-	0.890Å	0.871Å
Xα Parameters			
Outer α value:	0.74082	0.74677	0.75102
Intersphere α value:	0.74082	0.74677	0.75102
Phosphorus sphere radius:	0.991Å	0.989Å	0.923Å
Oxygen sphere radius:	0.959Å	0.913Å PO(2) 0.959Å PO(1) 0.941Å POH	0.957Å(2) PO(2) 1.036Å(2) POH(2)
Watson sphere radius:	1.560Å	2.738Å	2.590Å
Outer sphere radius:	2.519Å	2.738Å	2.590Å
Virial Ratio	1.0018568	1.0011094	0.9990408

Convergence: When the difference in potentials at the beginning and the end of the iteration were less than 10^{-5} of the potential at the start of the iteration. This gives energy levels that differed by less than 10^{-6} Rydbergs between the last two iterations.
Core electrons: "Thawed" so that they retained atomic character while being fully included in the iterative process. P(1s), P(2s), P(2p), C(1s), and O(1s) electrons were treated as core electrons.

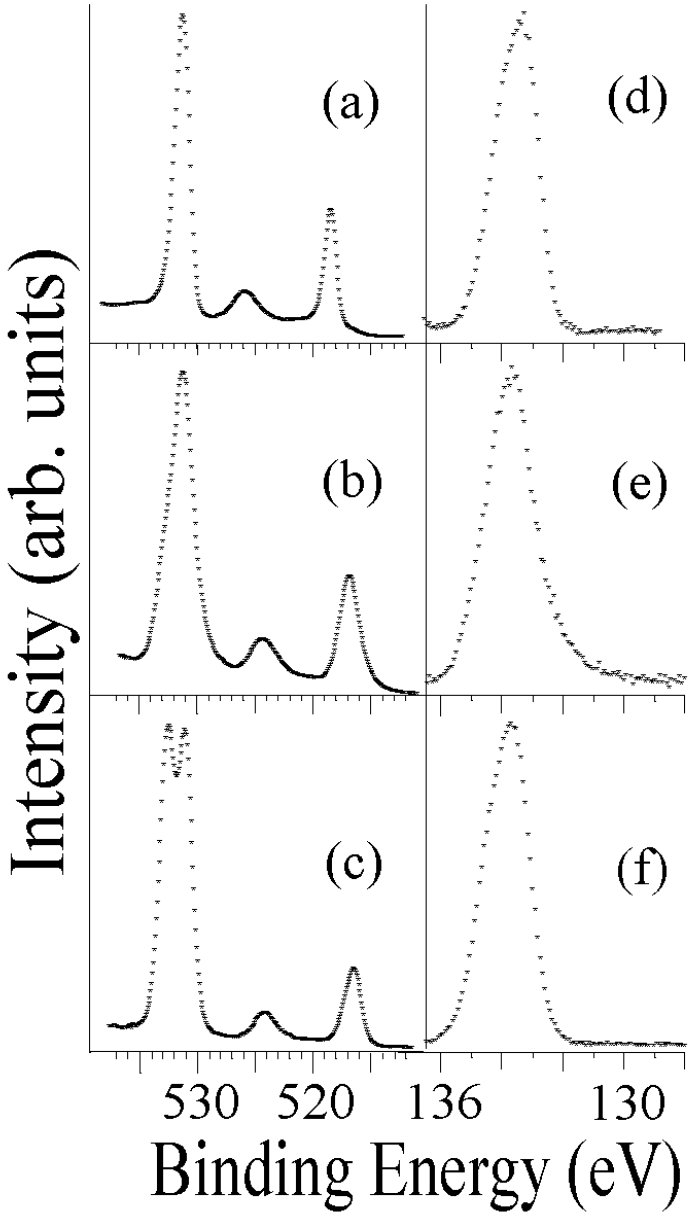

Figure 6.1 Core-level XPS spectra of the O1s/V2p (a-c) and the P2p (d-f) Region for the three compounds $VOPO_4.2H_2O$ (a, d), $VOHPO_4.0.5H_2O$ (b, e) and $VO(H_2PO_4)_2$ (c, f).

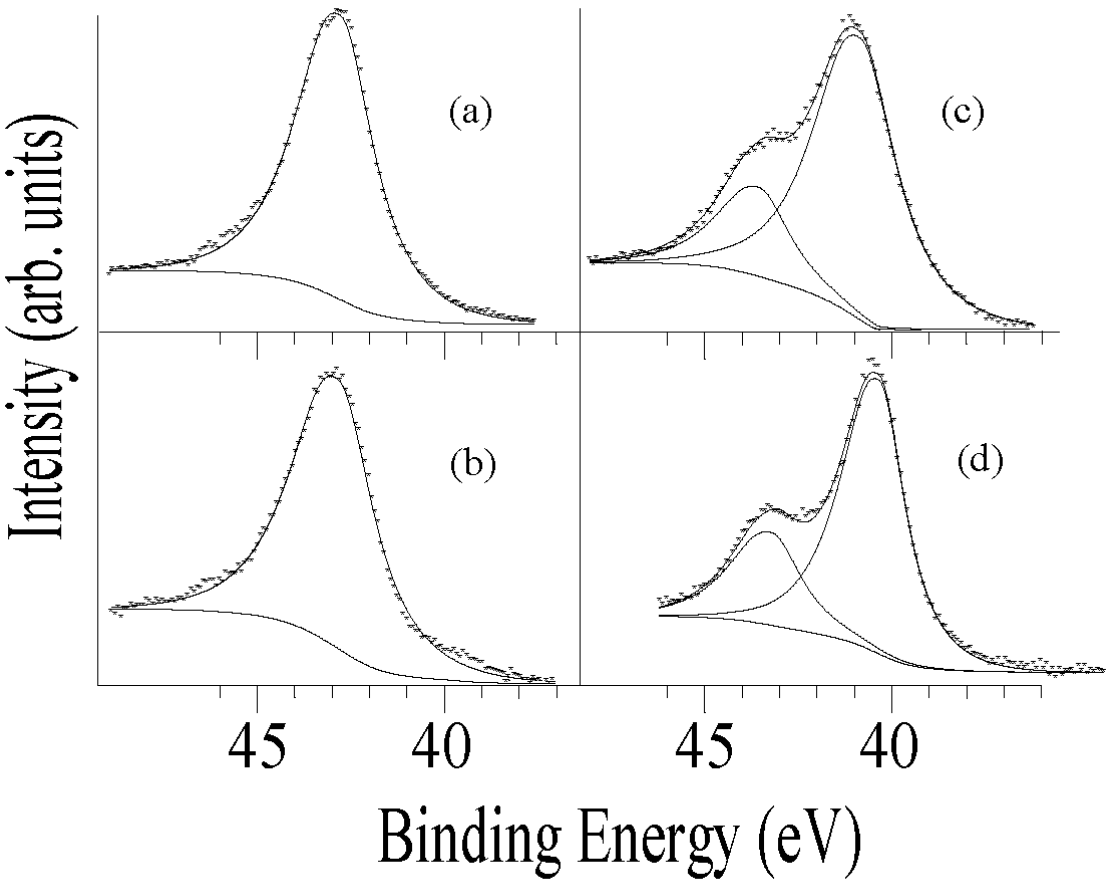

Figure 6.2 The V3p core level spectroscopy for $VOPO_4 \cdot 2H_2O$ (a), V_2O_5 (b), $VOHPO_4.0.5H_2O$ (c) and $VO(H_2PO_4)_2$ (d).

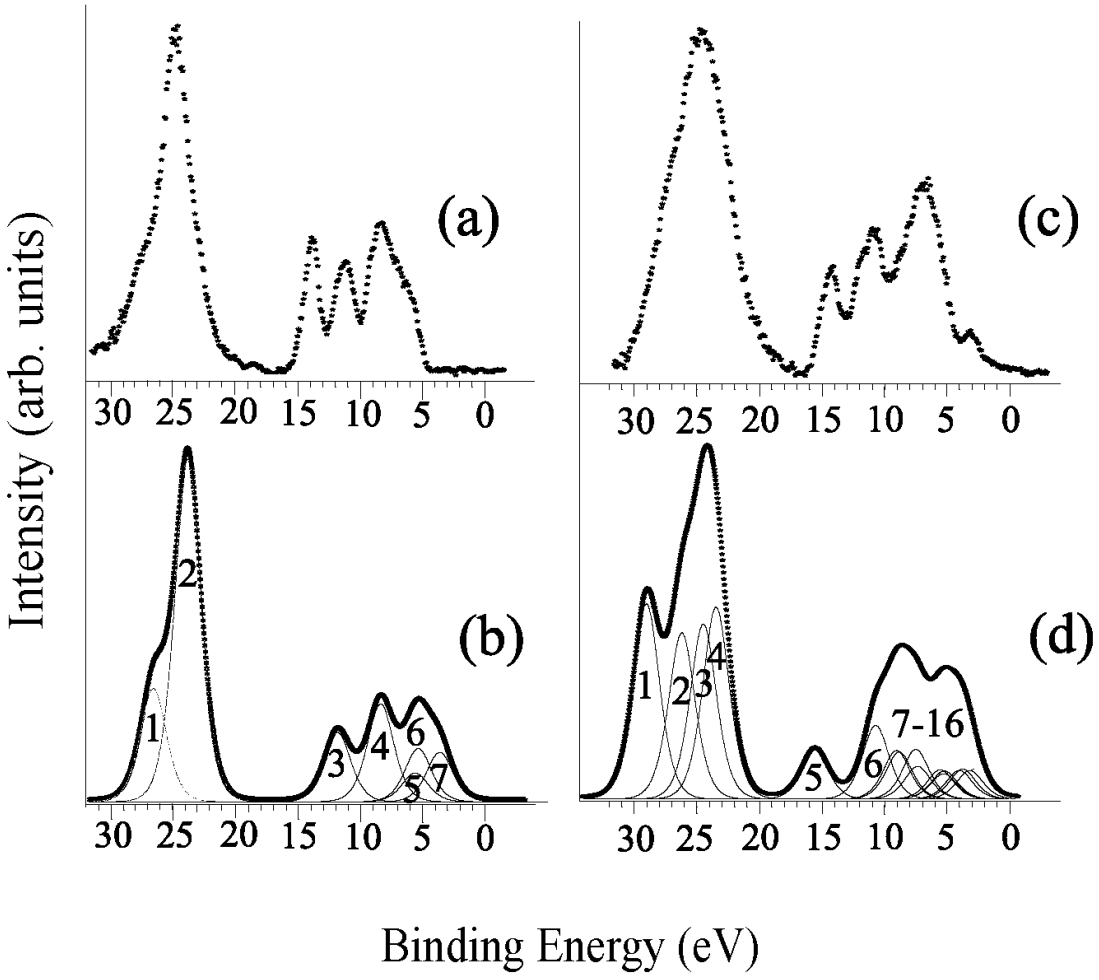

Figure 6.3 The Valence band regions for $VOPO_4 \cdot 2H_2O$ (a), $VOHPO_4.0.5H_2O$ (c) shown with corresponding calculated spectra for PO_4^{3-} (b) and HPO_4^{2-} (d).

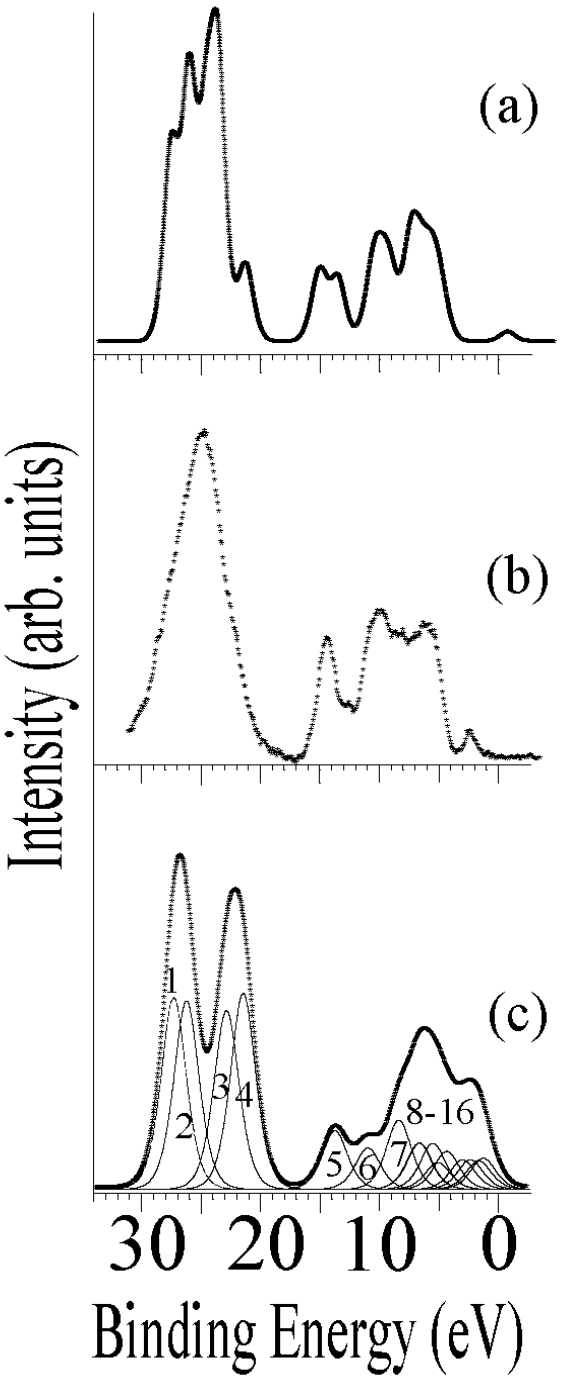

Figure 6.4 The valence band region for $VO(H_2PO_4)_2$ (b) shown with the calculated spectra for $H_2PO_4^-$ (c) and $VO(H_2PO_4)_2$ (a).

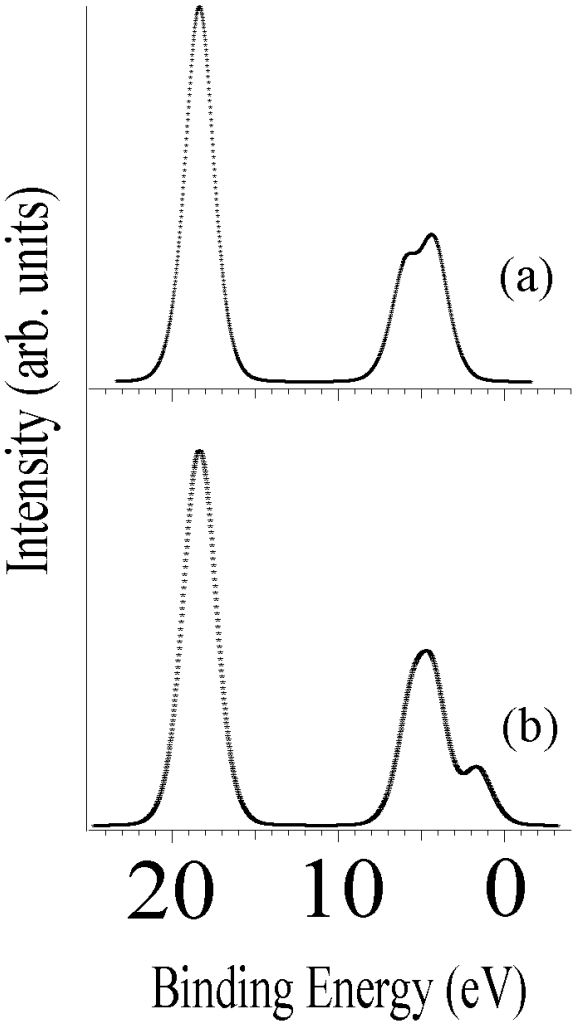

Figure 6.5 The calculated spectral contributions from the vanadyl species VO^{3+} (a) and VO^{2+} (b).

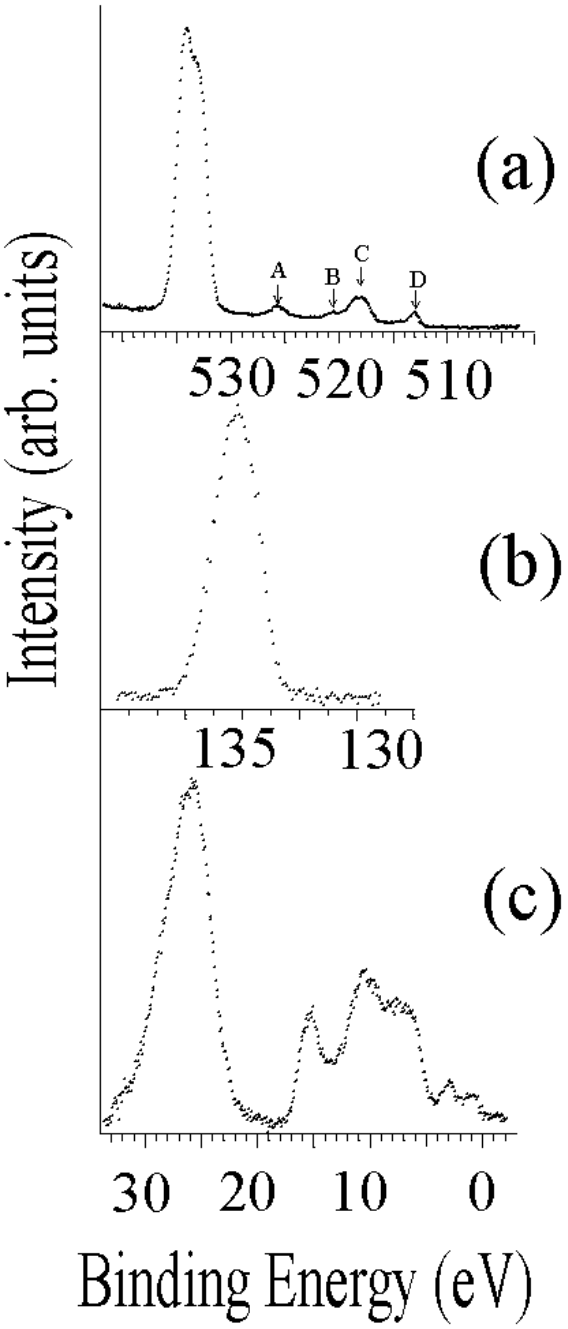

Figure 6.6 The XPS results for the 5M H_3PO_4 coating on Vanadium metal showing the O1s/V2p (a), P2p (b) and valence band (c) regions.

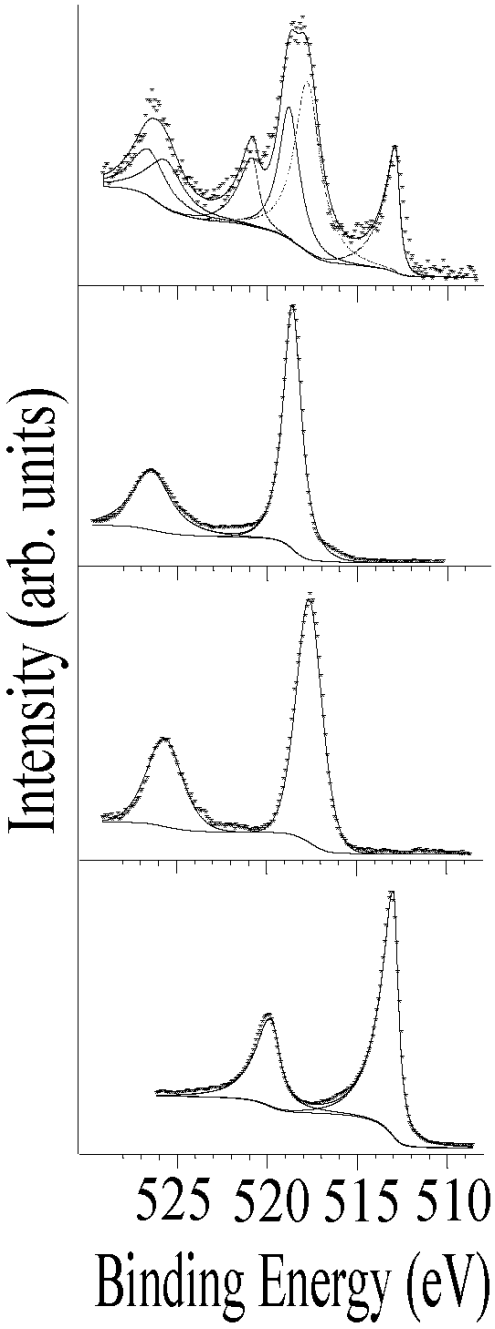

Figure 6.7 The fitted spectra of the coated vanadium metal (a), the compounds $VOPO_4 \cdot 2H_2O$ (b) and $VO(H_2PO_4)_2$ (c), and etched vanadium metal (d).

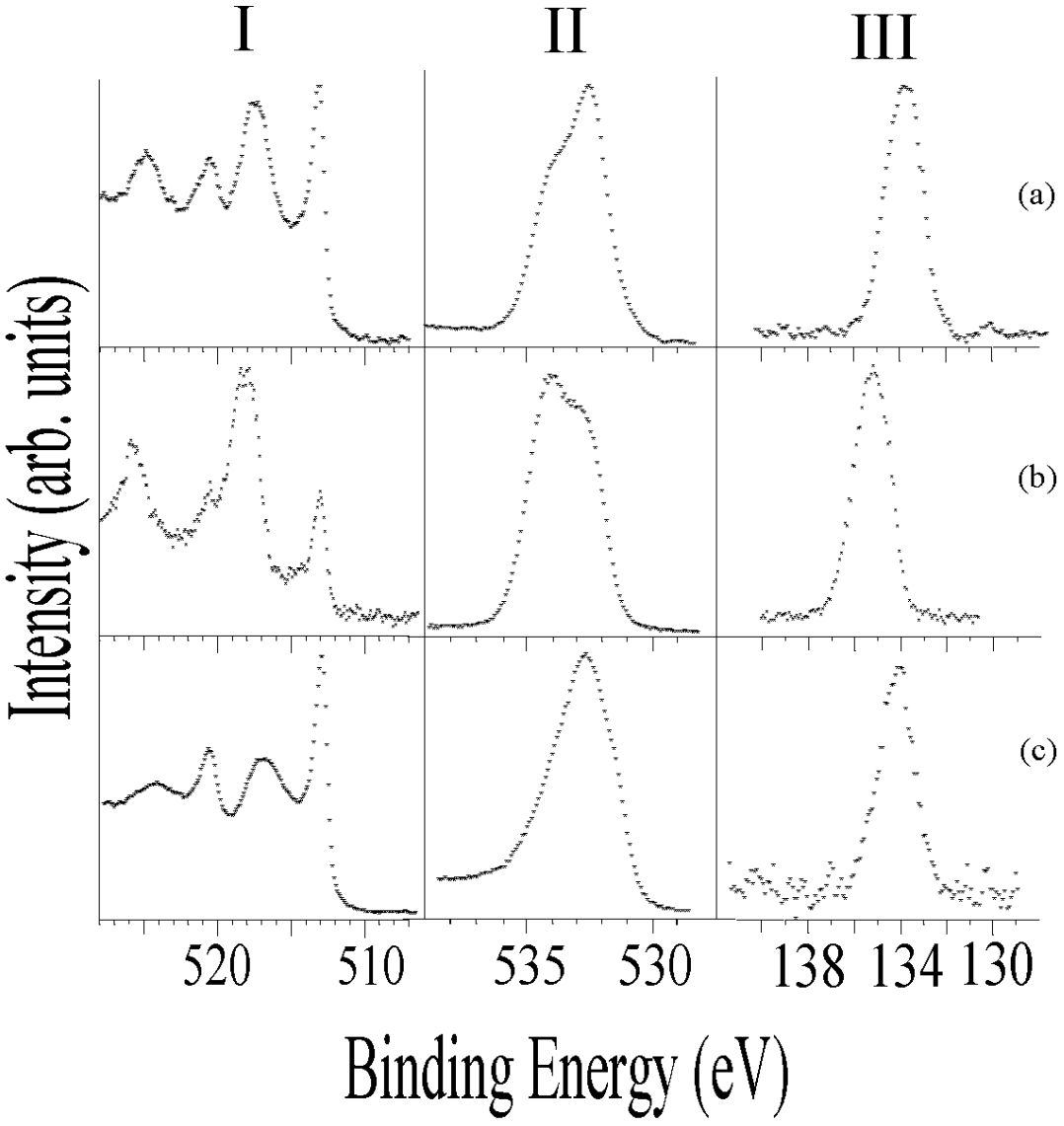

Figure 6.8 The core-level XPS results of the V2p (I), O1s (II), and P2p (III) regions for the -0.5V biased sample (a), unbiased (b) and +0.5V biased (c) samples.

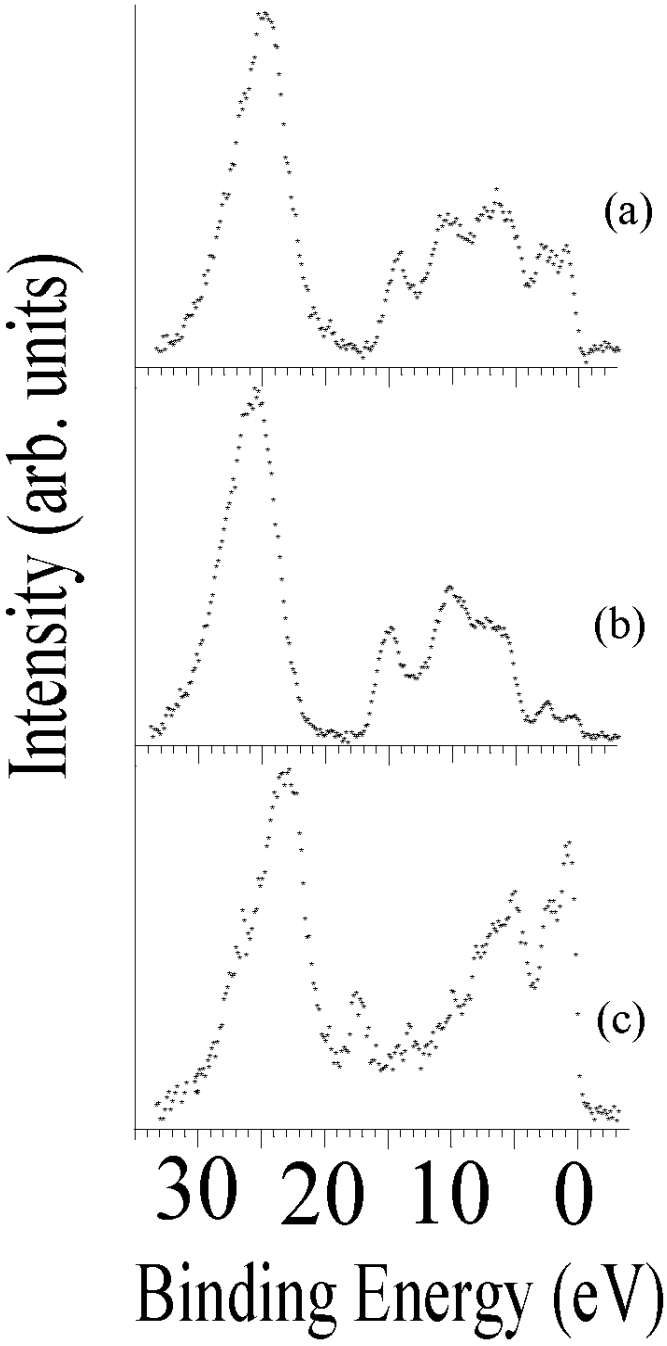

Figure 6.9 Valence band XPS results for the -0.5V biased sample (a), unbiased (b) and +0.5V biased (c) samples.

Chapter 7

The Study of Different Phosphate Films Formed on the Surface of Vanadium Metal by Valence Band X-ray Photoelectron Spectroscopy

7.1 Introduction

This chapter is concerned with using X-ray photoelectron spectroscopy (XPS) to distinguish between the differences in the bonding of different vanadyl phosphates both in the core and valence band region. It was shown that the use of valence band XPS is a strong method by which to identify between the many different types of phosphates[1,2]. In a recent study[3], the surface of aluminum was reacted with different phosphorous oxide acids so that thin (<100Å) oxide-free films can be formed directly on the metal surface. The thin films are similar in nature to the acid used. These films are present without a trace of metal oxide contamination and are very thin in nature. This chapter presents the application of these coatings to the vanadium metal surface by similar processes. Previously, the reactions of orthophosphoric acid, 5M H_3PO_4, with vanadium metal and other metals such as aluminum, copper, titanium and iron have been analyzed[4-8]. In addition to orthophosphoric acid; the reactions of phosphorus acid (H_3PO_3), hypophosphorus acid (H_3PO_2) and pyrophosphoric acid ($H_4P_2O_7$) with the vanadium metal surface will be examined in the present study.

In order to analyze the results seen in this experiment in the core and valence band region, vanadium phosphate compounds were previously synthesized[4] and interpreted by multiple scattered wave Xα calculations. These calculations gave a better

understanding to the spectral features in the valence band region, specifically, the phosphorus-oxygen bonding region, but did not account for the vanadyl ion ($VO^{2+/3+}$) contribution as they were only of the anion. Band structure calculations have been employed to examine the new coatings and to re-examine the previous compounds and the previous coating. Valence band XPS interpreted by calculation methods has been shown to effectively distinguish between different phosphates and between phosphate and oxide.

7.2 Experimental

7.2.1 Materials and Preparation

In order to create the phosphate coatings on vanadium metal without the presence of an oxide layer, research has shown that a clean, oxide free, metal surface is necessary. Recently a new process[9] has been employed where the coating is formed by removing the native oxide layer while submerged in a 5M acid solution using high grit waterproof emery paper. The experiment required orthophosphoric acid (H_3PO_4, 85%) from Fischer Scientific, phosphorus acid (H_3PO_3, 97%) from Alfa Aesar, hypophosphorous acid (H_3PO_2, 50%) and pyrophosphoric acid ($H_2P_4O_7$, 98%) from Sigma-Aldrich to create four 5M acid solutions to generate the four different coatings. The metal surface was abraded for ten minutes, to remove the oxide layer and expose the clean metal; followed by ten minutes to let the surface of the metal react with the solution. The surface was then rinsed using high purity water and dried in an oven at 110°C. The 5 M acid solutions, vanadium metal sample and emery paper were deairated, by bubbling

nitrogen through the solution for 2 hours prior to beginning the experiment. The bubbling was continued throughout the experiment to minimize dissolved oxygen.

7.2.2 Surface Analysis

All spectra were collected with a VSW HA150 spectrometer (150mm hemispherical analyzer) operated in the fixed analyzer transmission mode with a pass energy of 20 eV, equipped with a 16-plate microchannel detection system. The Al Kα X-radiation (240 Watts) generated from a 32 quartz crystal monochromator provides a linewidth of better than 0.2 eV. The base pressure of the instrument was 10^{-9} Torr or better.

The spectrometer energy scales were calibrated[10] using an argon-ion etched copper plate and calibration in this chapter was done using the peaks from the metal below the coating. This is done with the expectation that there is no charging between the metal and the coating on the metal. Biasing experiments carried out on all the new coatings show no sign of charging.

A non-linear background was removed from all valence band spectra using the iterative method described previously[11-13]which has been found to be effective in representing the background when fitting short energy range XPS spectra.[14]

7.2.3 Calculations

The band structure calculations were carried out using an extended version of the program CRYSTAL[15,16]. This program performs *ab initio* calculations of the ground state energy, electronic wave function and properties of periodic systems. One electron eigenfunctions of the Fock Hamiltonian are represented by linear combinations of Bloch

functions, which are also a linear combination of atomic orbitals. A Mulliken analysis is used to obtain orbital, atomic and total densities of states. The separate densities of states for each atom in the compound are evaluated. These groups of states are then adjusted by their corresponding atomic photoelectron cross section values as determined by Scofield[17]. These cross section adjusted densities of states are then convoluted with a Gaussian /Lorentzian product function[12,18] having a full width at half maximum of 1eV using a separately created program.

All band structure calculations are performed using STO-3G atomic orbital basis sets. The orthorhombic PNMA structure[19] of $VOPO_4$, monoclinic P21/C structure[20] for $VOHPO_4 \cdot 2H_2O$, tetrahedral P4/NCC structure[21] of $VO(H_2PO_4)_2$, tetrahedral I-42D structure[22] of $VOHPO_3 \cdot 5H_2O$ and the monoclinic C2/C structure[23] of $VO(H_2PO_2)_2 \cdot 2H_2O$ were used in the calculations.

7.3 Results and Discussion

Core and valence band X-ray photoelectron spectroscopic studies were conducted on films formed on vanadium with orthophosphoric acid (H_3PO_4), phosphorous acid (H_3PO_3), hypophosphorous acid (H_3PO_2) and pyrophosphoric acid ($H_2P_4O_7$), and the results compared with that of etched vanadium metal.

7.3.1 Core Level Spectroscopy

The overall spectra indicated the presence of the expected core regions, with all samples showing the presence of core levels assigned to oxygen, carbon and vanadium. Samples that had been treated by exposure to phosphorus acids showed the presence of phosphorus as well. .

O1s Region: The O1s region is shown in Figure 7.1(a-d). The spectra exhibit a number of overlapping features. These features would be expected to include oxide, hydroxide, features corresponding to vanadyl ions, $(VO)^{2+/3+}$, and various phosphorous-oxygen anions in the case of samples treated by exposure to phosphorus acids. The features in the O1s region of the salts of these acids has been discussed previously,[2] and our observations in this work are compatible with the earlier interpretation.

Orthophosphoric Acid: The use of orthophosphoric acid (H_3PO_4) led to film whose O1s spectrum is shown in Figure 7.1(a). The spectrum can be fitted to at least three overlapping peaks consistent with phosphate film composed of a dihydrogenphosphate anion, $(H_2PO_4)^-$, bound to a vanadyl species. If this is the case then three different types of oxygen atom would be the P-OH, P-O, and V-O bound oxygens, as shown in Figure 7.1(a). Previous data for the compound $VO(H_2PO_4)_2$, which is in the formal V(IV) oxidation state, yields an O1s spectrum resembling two overlapping identical peaks. The two peaks are believed to arise from two equal intensity peaks for the phosphate oxygen atoms (one corresponding to the P-O and the other the P-OH oxygens) and one lower intensity peak lying at a binding energy intermediate between that of the P-O and P-OH features, so contributing equally to each of the other peaks, giving the appearance of only two peaks. Here the vanadyl contribution has shifted to a higher binding energy, which we believe is due to the oxidation state of the vanadium in this coating differing from the compound $VO(H_2PO_4)_2$.

Phosphorous Acid: The use of phosphorous acid (H_3PO_3) acid led to film whose O1s spectrum is shown in Figure 7.1(b). The O1s region has an appearance similar to that

observed for phosphorous ion as previously reported,[2] with the addition of the contribution for the vanadyl ion.

Hypophosphorus Acid: The use of hypophosphorous acid (H_3PO_2) acid led to film whose O1s spectrum is shown in Figure 7.1(c). The O1s region has an appearance similar to that observed for hypophosphorous ion as previously reported.[2]

Pyrophosphorus Acid: The use of pyrophosphoric acid ($H_2P_4O_7$) acid led to film whose O1s spectrum is shown in Figure 7.1(d). The O1s region has an appearance similar to that observed for pyrophosphate ion as previously reported.[1,2]

V 2p Region: The vanadium 2p region, Figure 7.2(I), can be explained if one considers that the spectra are composed of the vanadium from the phosphate coating layer, interface region, and the vanadium from the metal below the surface. The metal below the surface gives two peaks at 513.0eV and 520.6eV, the V $2p_{3/2}$ and V $2p_{1/2}$, respectively. A spectrum for the V2p region of an etched vanadium metal sample was included, Figure 7.2(I e), for comparison. The other two main features, in the four coatings, are the contributions from the vanadium in the coating on the metal. The shift in binding energy from the metal V $2p_{3/2}$ peak to the V $2p_{3/2}$ peak in the coating can be as much as 5eV for a shift in the formal oxidation state from the $V^{(0)}$ to the $V^{(V)}$

The metal peaks are a strong internal calibration tool for the binding energy scale because tests show there is no charging between the coating and the metal. The intensity of the metal peak in relation to the intensity of the peaks for the coating gives an idea of the relative thickness of the coatings. The thickest coating is that of the orthophosphoric acid coating, Figure 7.2(I a). The next thinnest coating is the pyrophosphoric acid, Figure

7.2 (I b), then the phosphorus acid coating, Figure 7.2 (I c) and lastly the hypophosphoric acid coating, Figure 7.2(I d). The most intense metal peaks are seen in this sample.

The V2p peaks from the coating explain the oxidation state of the vanadium in the coating. In the orthophosphate coating, Figure 7.2 (I a), there is a mixture believed to be VO^{2+}/VO^{3+} in the coating (formal vanadium oxidation states IV/V). The position of the peak shows that it has a strong contribution from the $V^{(V)}$ oxidation state. The phosphorous acid coating, Figure 7.2 (b), also has a mixture of these species, but the V2p spectra is primarily composed of the $V^{(IV)}$ where the orthophosphate acid was strongly $V^{(V)}$. The hypophosphorus acid coating, Figure 7.2 (I c), shows a peak maximum which is similar to the $V^{(IV)}$ state, but has a sweeping tail to the lower binding energy. This sweeping tail is due to oxidation states lower than $V^{(IV)}$.

P2pRegion: Figure 7.2(II a-d) shows the P2p region for the 4 coatings. Shifts in the energy of the features is seen with the orthophosphoric acid coating (a) at 135.3 eV, the phosphorus acid coating (c) at 134.1 eV, the hypophosphoric acid coating at 133.1 eV and the pyrophosphate coating at 134.2 eV. To analyze the origin of the shifts in the coatings there are different factors that could contribute, such as, a change in the potential surrounding the phosphorus atom or a change in the relaxation energy during the photioization process. Changes in the relaxation energies could be attributed to corresponding to changes in the structure of the phosphate ion, but without adequate calculation the certainty of this is in question. One thing of note here is the hypophosphorus and pryophosphoric acid coated metal surfaces did not show changes when the O1s, V2p, P2p and C1s regions were rerun with an applied negative bias of 10V.

7.3.2 Valence Band Spectroscopy

5M H_3PO_4- To identify this coating, three compounds: $VOPO_4 \cdot 2H_2O$, $VOHPO_4 \cdot 1/2H_2O$ and $VO(H_2PO_4)_2$, were previously studied, with their valence band spectra, Figure 7.3(a,c,e respectively), being compared to spectra predicted by multiple scattered wave Xα calculations.[4] These calculations were done for only the anions in the system and contained no contribution from the vanadyl, $VO^{2+/3+}$ species. The calculations explained in detail what changes occur in the phosphate bonding energy levels, 10-16eV and the O2s level, 20-28eV. In the same study the $VO(H_2PO_4)_2$ valence band spectrum was compared to a predicted spectra from a band structure calculation. This calculation used optimized basis sets for the atoms in the system. New band structure calculations for the three model compound have been completed and their spectra are displayed, Figure 7.3(b,d,f). These predicted spectra help us to determine what occurs in all regions of the valence band, helping in the analysis of the coating.

When examining the model compounds and the spectra predicted by band structure calculation, several assertions can be made. First, the band structure calculations overestimate the shifts in the O2s region. These peaks do explain what happens in this region, primarily identifying how the vanadyl cation's oxygen atom and the phosphate anion's oxygen atoms differ. The experimental and calculated spectra for the $VOPO_4$, Figure 7.3(a, b), show that the main feature at 23.5 eV should have three main components. The main component predicted at 25 eV with a secondary component creating a shoulder at 26.5eV. The third component is predicted as another peak at 30 eV,

due to the vanadyl species. Experimentally, the O2s region shows agreement, as there is a main peak with a large sweeping shoulder at the higher energy side.

Several things differ between $VOPO_4 \cdot 2H_2O$ and the remaining two model compounds. The oxidation state of the vanadium in the system changes from a formal $V^{(V)}$ state to a formal $V^{(IV)}$ in $VOHPO_4 \cdot 1/2H_2O$ (Figure 7.3(c,d)) and $VO(H_2PO_4)_2$, Figure 7.3(e,f). There are also changes in the phosphate ions as the tetrahedral ion in $VOPO_4$ becomes a lower symmetry Cs in $VOHPO_4 \cdot 1/2H_2O$ and C2v in $VO(H_2PO_4)_2$. The previous work[4] showed that the changes in symmetry lead to broadening of this region, but the band structure calculation now predicts the asymmetry in the O2s region at the lower binding energy side of the two spectra. The band structure calculations show a shift in the vanadyl O2s of 9eV with the change in formal charge. Experimentally, this is seen best in the $VO(H_2PO_4)_2$, Figure 7.3(e), as a shoulder at 22eV which was previously unaccounted for by the calculation. The $VOHPO_4 \cdot 1/2H_2O$, Figure 7.3(c), does not show a distinct shoulder, as the low symmetry hydrogenphosphate ion has more shifting in this region, but the Xα calculations predicted the shifts for the P-OH bond at higher energy, leaving the vanadyl species responsible for most of the asymmetry seen at the lower binding energy side.

The second assertion is that the contribution of the vanadyl species remains primarily below 10eV in the lower valence band region. Figure 7.5(a), shows the calculation for the $VOPO_4$ (Figure 7.4(b)), but now it is broken down into contributions from the vanadyl species(c), VO^{3+}, and the orthophosphate anion(b), PO_4^{3-}. The contribution from the vanadyl species has had its intensity normalized to the same height as the phosphate ion, but its intensity is actually less than a fourth of the phosphate

counterion. The vanadyl species has very low intensity above 10eV allowing for this region to be the best for studying phosphate chemistry and the two features above 10eV can be considered primarily phosphate in nature. Thus, the changes then seen in the peaks above 10eV in the two other compounds, Figure 7.3(c, e), would be attributed to changes in the phosphate counterions. The calculated spectra for the two hydrogen phosphate compounds, Figure 7.3(d, f), show strong agreement with the experimental spectra and the previously reported Xα calculations.

The third assertion is the calculation for the contribution of the single unpaired d-electron in the valence band for the two $V^{(IV)}$ states is not fully resolved, dissimilar to what is seen experimentally. The $VOPO_4 \cdot 2H_2O$, Figure 7.3(a), compound has no such electron and the predicted spectra show no feature below 4eV. The $VOHPO_4 \cdot 1/2H_2O$, Figure 7.3(c) and $VO(H_2PO_4)_2$, Figure 7.3(e), each have a d-electron, and its contribution is seen in this region. The calculation for the $VOHPO_4 \cdot 1/2H_2O$ shows only a slight shoulder, which sweeps to 0eV. The $VO(H_2PO_4)_2$ calculation shows a more resolved shoulder, but not to the degree of what is seen experimentally. These calculations do predict the d-electron peak in $VOHPO_4 \cdot 1/2H_2O$ to be much less resolved than the $VO(H_2PO_4)_2$ d-electrons, but neither shows enough separation. This is due primarily to the basis set choice for the vanadium atom, as previous work with the optimized basis set for the $VO(H_2PO_4)_2$ calculation yielded a single peak at 1eV. Optimized basis sets were not used here as to allow for similarity in all calculated spectra and because the primary area of focus is the two phosphate peaks and the O2s feature.

The analysis of the coating on vanadium metal, Figure 7.3(g), brings up another feature at 0eV, which should be addressed as it is seen in all the coating valence band

spectra, the presence of the metal. The metal signal here is small as the coating is thick, but the other coatings have a large increase in this feature. The nature of the phosphate in the coating was decidedly of the dihydrogenphosphate anion as seen from the valence band being very similar in peak structure to the $VO(H_2PO_4)_2$ calculation. This agrees also with the observations in the O1s core level. The main difference between the coating and the model $VO(H_2PO_4)_2$ compound arises in the region from 0-10eV where the vanadyl species is present. These changes are due to what was described earlier, when discussing the V 2p core region, the mixture of VO^{2+} and VO^{3+} in the coating.

5M H_3PO_3, 5M H_3PO_2- The valence band for the phosphorus acid and hypophosphorous acid coatings are shown in Figure 7.5(a,c), along with band structure calculation predicted spectra of $VOHPO_3$ and $VO(H_2PO_2)_2$, Figure 7.5(b,d). The phosphorus acid treatment, Figure 7.5(a), created a coating that can be easily predicted by calculation. The metal feature at 0eV was not included in the calculation and the d-electron peak at 2eV is represented by a shoulder in the calculation at 2eV. The two phosphate peaks at 9eV and 13eV show similar peak intensities and shape to the calculation. The experimentally obtained O2s region does not show the double peak, as the calculation does, but it does display widening, with a small shoulder on the higher binding energy side similar to the small feature due to the vanadyl species. This coating was relatively thick so the metal contribution is low, giving less distortion below 5eV.

The hypophosphorus acid coating, Figure 7.5(c), is very thin and as was seen in the core region for this coating contains lower oxidation state vanadium (V^{X+}, where $X \leq 3$) unlike the other coatings. This changes the valence band in the lower region creating

overlap with the phosphate peak at 10eV. The calculation of the vanadyl(IV) hypophosphite, Figure 7.5(d), predicts less overlap in this region, but the mixture of oxidation state will account for this overlap. The decrease in intensity of the calculation predicted phosphate peak at 16eV to what is seen experimentally at 14eV is also a product of the mixture of oxidation states. The presence of oxidation state lower than V^{4+} will shift the anion:cation ratio in favor of the cation, changing the ratio of the observed phosphate peaks versus the vanadium valence band region. The O2s region in this coating is much clearer as oxidation states lower than V^{4+} will not generally form a vanadyl species, but will be present as individual metal ions. This will minimize much of the effect in the O2s region. Experimentally, the O2s region agrees quite well with the band structure calculated spectrum of this region, showing that the expected contribution from the phosphate is correct.

5M $H_4P_2O_7$- The results for the valence band region of the pyrophosphoric acid coating are shown in Figure 7.6(a), along with the spectra for two sodium phosphates, the pyrophosphate, 7.6(b) and the dihydrogen pyrophosphate, 7.6(c). When considering the state of the pyrophosphate ion it helps to use the phosphate region of the valence band. The valence band for the coating resembles the sodium pyrophosphate compounds, Figure 7.6(b,c). The two peaks at 10eV and 15eV have the correct intensity to be that of a pyrophosphate when compared to the sodium salts of the pyrophosphate, Figure 7.6(b), and the dihydrogen pyrophosphate, Figure 7.6(c). This coating contains primarily the protonated form of the pyrophosphate. The reasoning behind the assertion is that the valley in the spectra at 13eV. In the coating, the valley resembles that of the sodium

dihydrogen pyrophosphate, but the intensity seen in the valley is not a high as seen in the sodium salt of this ion. The valley's intensity differences in the two sodium salts was shown by calculation to be due to changes in the bonding when the hydrogen atoms are bound to oxygen atoms on the pyrophosphate.[1] The intensity in the valley region also can be explained as a mixture, but the major contribution is from the protonated pyrophosphate. The O2s region of the valence band spectrum also seems to be a combination of the two spectra for the sodium salts, but it more closely resembles the protonated ion.

7.4 Conclusion

This work indicates that it is possible to generate different phosphate films on vanadium metal having the $(VO)^{3+}$ or $(VO)^{2+}$ species present. Core and especially valence band XPS show the ability to distinguish between the different phosphate species of vanadium existing in the coatings. The changes in the phosphate valence band that arise from either when the phosphate ion changes from the highly symmetrical orthophosphate to the much less symmetrical hydrogen phosphates, or when oxygen atoms are replaced by hydrogen atoms or additional phosphates, can be understood by examining the changes in the valence band spectra and comparing these changes with spectra generated from band structure calculations.

7.5 References

1. A.L. Asunskis, K. Gaskell, D.J. Asunskis, P.M.A. Sherwood, J. Vac. Sci. Technol. A **21**, 1126 (2003).

2. P.M.A. Sherwood, Surf. Sci. Spectra **9**, 62 (2002)

3. K. Gaskell, M. Smith, P.M.A. Sherwood, J. Vac. Sci. Technol.A **19**, 1176 (2004).

4. D.J. Asunskis, P.M.A. Sherwood, J. Vac. Sci. Technol. A **21**, 1126 (2003)

5. J.A. Rotole and P.M.A. Sherwood, **U.S. Patent No.: 6,066,403** "Metals having Phosphate Protective Films" - May 23, 2000

6. J.A. Rotole and P.M.A. Sherwood, Chem. Mater**. 13**, 3933 (2001).

7. J.A. Rotole and P.M.A. Sherwood, J. Vac. Sci. Technol. A **18**, 1066 (2000).

8. J.A. Rotole , K. Gaskell, A. Comte, P.M.A. Sherwood, J. Vac. Sci. Technol.A **19**, 1176 (2001).

9. Y-Q Wang and P.M.A. Sherwood, J. Vac. Sci. Technol. A, **21**, 11 (2003).

10. M.P. Seah, I.S. Gilmore, G. Beamson. Surf. Interface. Anal. **26,** 642 (1998).

11. R.O. Ansell, T.Dickinson, A.F.Povey and P.M.A. Sherwood , J Electroanal Chem **98**, 79 (1979).

12. P.M.A. Sherwood, in *Practical Surface Analysis by Auger and X-ray Photoelectron Spectroscopy*; Edited by D. Briggs and M.P. Seah (Wiley, New York, 1983) Appendix 3.

13. A. Proctor and P.M.A. Sherwood, Anal. Chem **54**, 13 (1982).

14. P.M.A. Sherwood, J. Vac. Sci. Technol. A, **14**, 1424 (1995).

15. C. Pisani, R. Dovesi, and C. Roetti, *Hartree-Fock Ab Initio Treatment of Crystalline*

systems, Lecture Notes in Chemistry, 48 (Springer, Rerlin 1988 and QCPE 577).

16. V. R. Saunders, R. Dovesi, C. Roetti, M. Caus, N. M. Harrison, R. Orlando and C. M. Zicovidh-Wilson, *Crystal 98 User's Manual,* 1998, University of Torino, Torino.
17. J. H. Scofield, J. Electron Spectrosc. Relat. Phenom. **8**, 129 (1976).
18. R. O. Ansell, T. Dickinson, A. F. Povery, and P.M.A. Sherwood, J. Electroanal. Chem**.** 98**, 79** (1979)
19. R.Gopel, C. Calvo J. Solid State Chem. **5**, 432 (1972).
20. A. LeBail, G. Ferey, P. Amoros, D. Beltran-Portier Eur. J. Solid State Inorganic Chem. **26**, 419 (1989).
21. S.A. Linde. Y.E. Gorbunova. A.V. Lavrov. V.G. Kuznetsov. Doklady Akademii Nauk SSSR **244**, 1411-1414 (1979)
22. B.S. Zakharova, A.B. Ilyukhin, N.N. Chudinova
23. A. LeBail, M.D. Marcos, P.Armos Inorganic Chem. **33**, 2607 (1994).

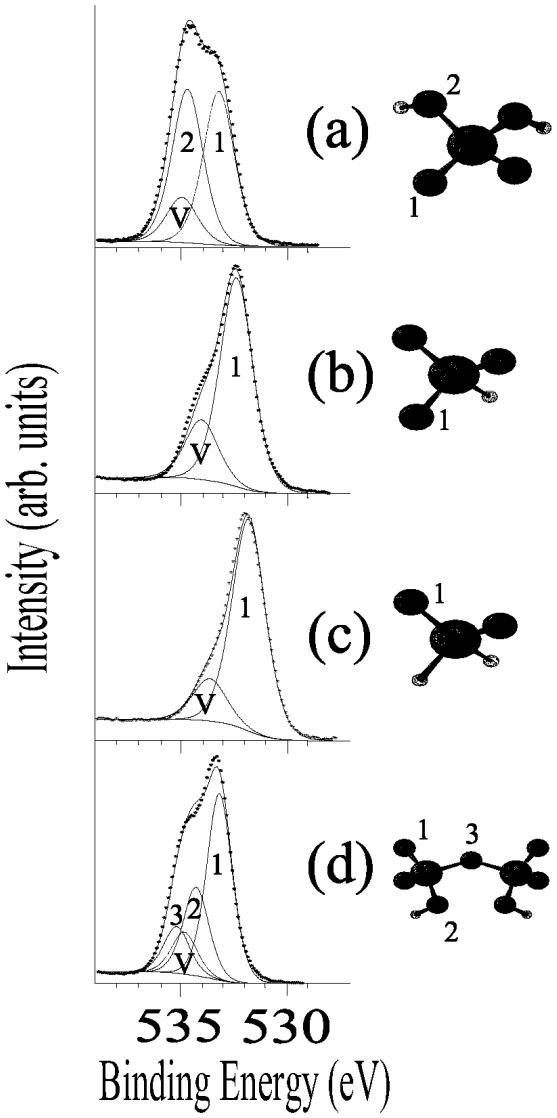

Figure 7.1 The O1s region showing the contribution to the spectrum by the oxygen in the phosphate ion (numbered) and from the vanadyl species (V).

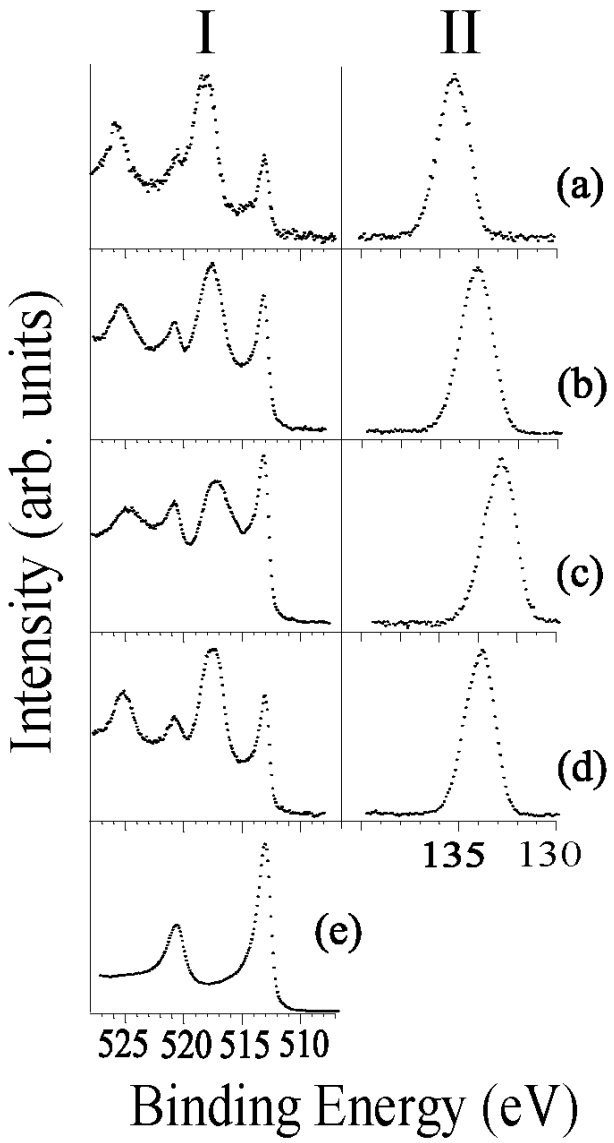

Figure 7.2 The XPS results for the V2p (I) and P2p (II) are shown for the orthophosphoric acid (H_3PO_4), phosphorus acid (H_3PO_3), hypophosphorous acid (H_3PO_2) and pyrophosphoric acid ($H_2P_4O_7$) coatings and etched vanadium metal(a-e, respectively).

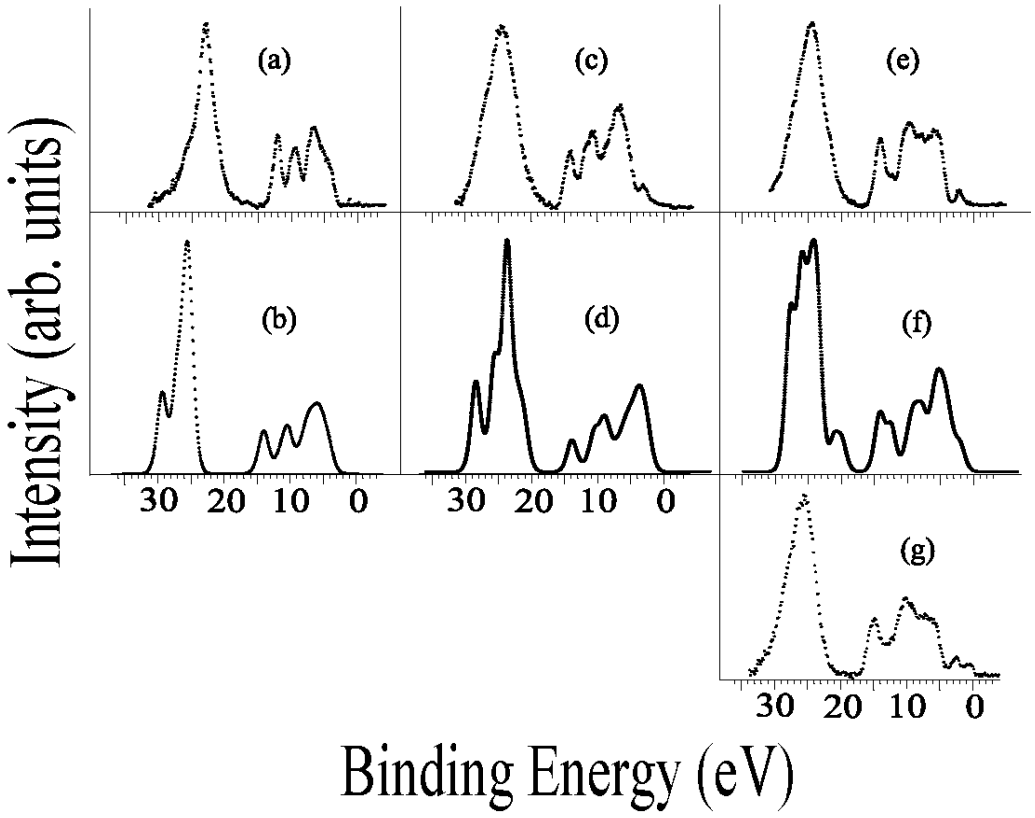

Figure 7.3 The Valance band XPS results for the model compounds $VOPO_4 \cdot 2H_2O$(a), $VOHPO_4 \cdot 1/2H_2O$(c), $VO(H_2PO_4)_2$(e), the 5M H_3PO_4 Vanadium metal coating(g) and accompanied by band structure calculations for $VOPO_4$(b), $VOHPO_4 \cdot 2H_2O$ (d) and $VO(H_2PO_4)_2$(e).

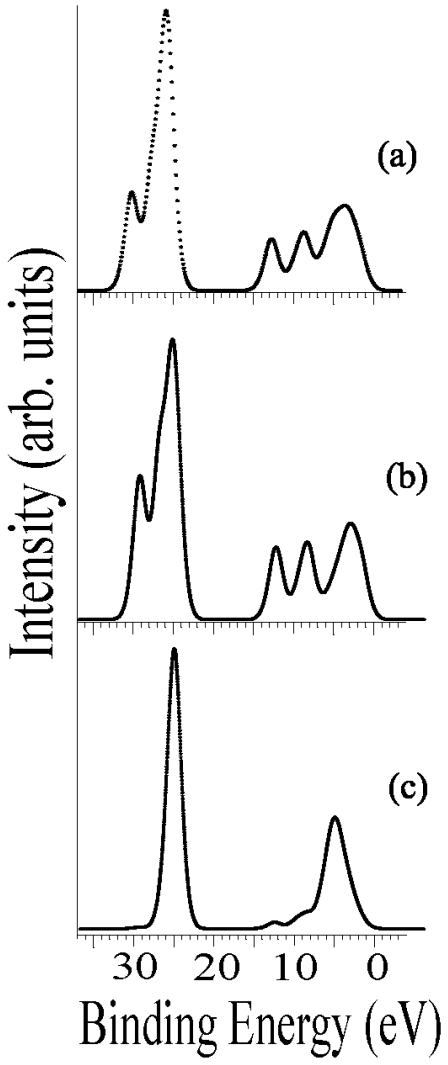

Figure 7.4 Band Structure calculation predicted Spectrum of $VOPO_4$(a), from Figure 3(b), broken down to show contributions of the orthophosphate, PO_4^{3-}, anion(b) and the Vanadyl, VO^{3+}, species(c).

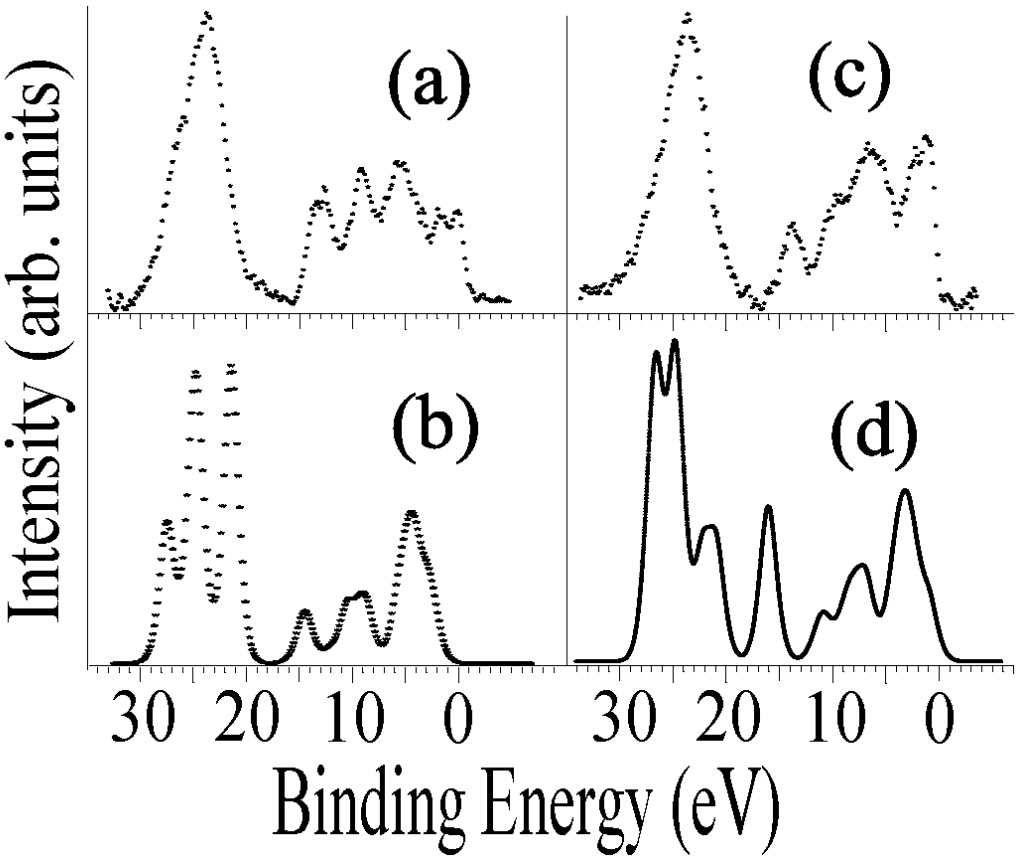

Figure 7.5 The Valence band XPS results for the phosphorus acid(a), 5M H_3PO_3, and the hypophosphorus acid(c), 5M H_3PO_2, and the band structure predicted spectra for $VOHPO_3 \cdot 5H_2O$(b) and $VO(H_2PO_2)_2 \cdot 2H_2O$(d).

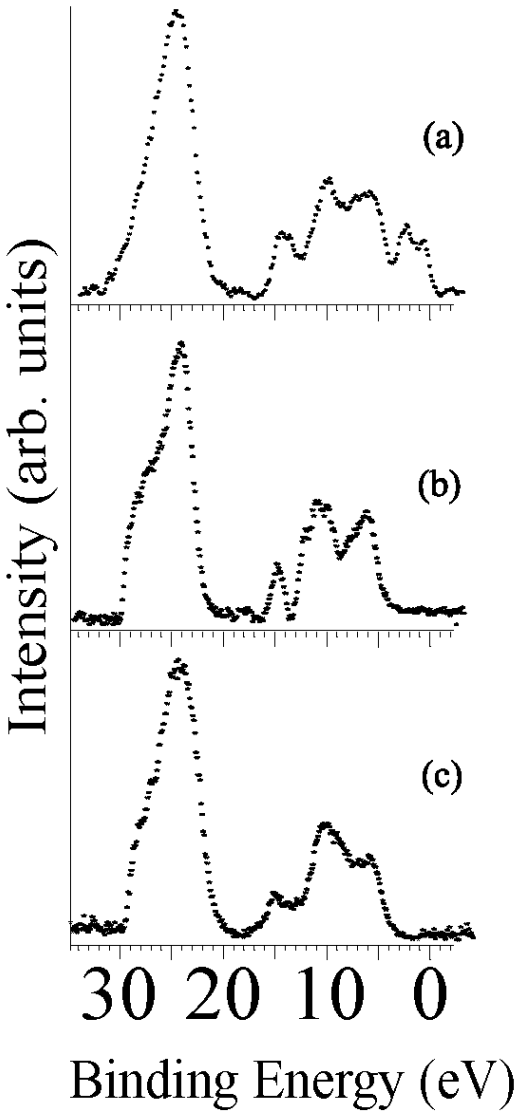

Figure 7.6 The Valence band XPS results for the pyrophosphoric acid coating(a), 5M $H_4P_2O_7$, and two sodium salts; sodium pyrophosphate(b), $Na_4P_2O_7$, and sodium dihydrogenpyrophosphate(c), $Na_2H_2P_2O_7$.(Na 2s feature removed by peak subtraction for b and c.)

Chapter 8

XPS Analysis of a Copper-Acquisition Compound from a Methane Oxidizing Bacteria

8.1 Introduction

Methanotrophic bacteria oxidize CH_4 as a source of carbon and energy. These bacteria are of great interest because rather than storing simple hydrocarbons when they absorb them, they react and oxidize them. This process helps remove unwanted hydrocarbon from the environment and is performed by enzymes in the bacteria which have metal atoms at the center. One of these bacteria, *Methylosinus trichosporium* OB3b, has been found to utilize copper in this process.[1] Compounds responsible for binding and transporting the metal atom inside the cell are of great interest and one of these compounds, methanobactin, has been isolated and purified for study. The structure and MALDI-TOF mass spectrum of the compound methanobactin, $C_{45}N_{12}O_{14}H_{62}S_5Cu$, has been previously reported.[1]

To analyze the oxidation state of the copper in biological samples EPR, electron paramagnetic resonance, has been a common choice. This technique only allows for the detection of the $Cu^{(II)}$. In order to quantify the $Cu^{(I)}$ content via EPR an indirect measurement is required, where the concentration is found by analyzing the $Cu^{(II)}$ concentration and the total copper concentration. The use of XPS allow for all existing states of copper in the sample to be detected simultaneously, making analysis more definitive.

Previous work on the oxidation state of copper in a superconductor sample[2] has been done and the calculations of the various copper states will be explored here for explanation of the features seen experimentally. The unpaired electron in the $Cu^{(II)}$ state that allows for study by EPR creates some final-state effects in the photo-ionization process, which create satellite features in the spectrum. An explanation of the charge transfer (CT) occurring in the ionization process is included. The features resulting from the CT process aid in the determination of the oxidation state of copper in the sample.

8.2 Experimental

In order to minimize sample oxidation when loading the sample, the sample was placed in an argon filled glove bag positioned at the sample introduction port on the XPS instrument. The sample was then opened and removed from the refrigerated tube and mounted on double-sided conductive tape for analysis. It has been shown previously[2] that in a standard instrument with the X-ray source position adjacent to the sample that thermal reduction of copper can be seen. The use of the monochromator on the instrument effectively removes the X-ray source from immediate contact with the sample, eliminating the possibility of reduction during analysis.

8.3 Results and Discussion

The survey spectrum, Figure 8.1, shows the elemental contributions from the sample. Contributions from the carbon and oxygen regions dominate the spectra, with only small features present from the copper region at 932.9 eV and the sulfur features

below 250 eV. Figure 8.2 shows a finer analysis of the core level XPS results for the O 1s (a), C 1s (b), S 2p (c) and the N 1s (d) regions.

The oxygen spectrum for this sample, Figure 8.2(a), and the carbon spectrum, Figure 8.2(b), shows the complex functionality existing in the compound. The oxygen shows a strong feature s at 531.6 eV with a shoulder towards the lower binding energy side at 529eV. The shoulder is expected as much of the oxygen in the sample exists in a C=O environment. The carbon region also shows similar features. The main peak in this region, at 284.6 eV, is due to the alkyl (C-C) bound carbons. The feature at 287.5 eV shows the presence of the carbonyl carbons and the shoulder at 286 eV is indicative of the alcohol bound carbons. These shifts are similar to the shifts seen in hydraquinone and benzoquinone which have similar functional groups.[3]

The sulfurs in this sample exhibit an XPS feature with a maximum at 162.8 eV, Figure 8.2(c). This feature shows a shift to what is seen a bound organic environment. An example of this is a polythiophene compound, which has the same chemical shift.[4] The S2p region is susceptible to a large change in peak position with a change in chemical environment. Published values for the negative sulfur in sulfides (S^{2-}) contains a feature located at 161eV, while the very positive sulfur in a sulfate (SO_4^{3-}) is at 168eV.[5,6] The main feature in the sample spectrum, Figure 8.2(c), has a has a strong shoulder at 164 eV. These shoulder is evidence of the spin-orbit splitting of the 2p level. The intensity of the shoulder is half the intensity of the main peak, as is predicted. The published value for the splitting in the S2p region is 1.1 eV, which is consistent with the shoulder in this region being the $S2p_{1/2}$ feature. The asymmetric slope on the lower

binding energy side of the main feature is indication that the sulfurs in the sample have slightly different chemical shifts.

The nitrogen, Figure 8.2(d), in this sample created a feature at 399.8 eV. The sharp single peak is what is expected from an aromatic amine environment, which would also fit the structure that had been given for the sample.[7]

The copper content in this sample was found to be very low in concentration in comparison the carbon and the oxygen content and there were no traces of contribution from other metals such as zinc or nickel. The sample is predominantly in the $Cu^{(I)}$ oxidation state, with some impurity due to the $Cu^{(II)}$ state. Figure 8.3 shows the copper 2p region for the sample and for a reference compound, CuO. The CuO sample has the copper in the formal oxidation state of $Cu^{(II)}$. The Cu2p region, Figure 8.3(b), has four peaks, two of which are satellites (942 eV, 944eV) and two are the $Cu2p_{1/2}$ (952.8 eV) and the $Cu2p_{3/2}$ (933.0 eV). The satellite features show up in the $Cu^{(II)}$ spectra as intense features shifted to higher binding energy of the two Cu2p peaks, the intensity of the satellites being about one-half of the intensity of the neighboring 2p feature. The satellite features to the higher binding energy of the $2p_{1/2}$ peak are not shown because this feature for the sample was not seen due to overlapping by a neighboring oxygen auger peak. This can be seen in the survey spectrum, Figure 8.1.

The sample's Cu 2p spectrum, Figure 8.3(a), includes very small content from the satellite features at 942 eV and 944 eV. The position of the main 2p feature at 933.0 eV is characteristic of the $Cu^{(I)}$ copper as the $Cu^{(II)}$ has it peak at 934.4 eV.(from CuO) An understanding the presence of the satellite feature will aid in making a solid determination of the oxidation state of the copper in the compound.

Generally, the high energy of the X-radiation will eliminate final state effects, but the Coulomb interaction between the lone unpaired electron in the valence level and the remaining 2p electron upon 2p-ionization make the probability of other final states more likely. Charge transfer (CT) of an electron from a ligand orbital to a metal orbital can be used to explain the features seen experimentally in the $Cu^{(II)}$ state. Data from a previous calculation are illustrated in Figure 8.4.

The calculation of the basic ground state and three possible states of the photoionization process for the CuO_4^{6-} and CuO_4^{5-} cluster models were performed. Figure 8.4 shows only the position of the orbital energies for the 4B1g and 3B1g molecular orbitals. The ground state was calculated and the 4B1g orbital is primarily Cu in contribution while the 3B1g orbital is mostly O2p in character. A transition from the 3B1g to the 4B1g can be considered a possible ligand-to-metal charge transition. A complete molecular orbital analysis for these calculations has been previously reported.[2]

The d^9 ground state shows the separation of these orbital at 5eV. Configuration interaction, which allows for the mixing and populating of the different final state also allows for multiple ground states. Other states are neglected here. The $2p^53d^9$, $2p^53d^{10}\underline{L}$ and $2p^53d^{9.5}L^{0.5}$ states have been calculated to explain the results of the photoionization from the $2p^63d^9$ state. $\underline{L}$ is a term that represents the removal of an electron from the ligand-type orbital. A one electron CT process gives rise to the two, $2p^53d^9$ and $2p^53d^{10}\underline{L}$, possible final states. The $Cu2p_{3/2}$ main feature that is seen experimentally is the result of a transition to the later, which shows a separation of 10.2 eV between the 4B1g and 3B1g molecular orbitals. The total energy difference between the $2p^53d^9$ and $2p^53d^{10}\underline{L}$ possible final states was calculated at 7.8 eV , which is also the separation of the levels

during what can be considered a transition state a($2p^5 3d^{9.5} L^{0.5}$) in the CT process.(Figure 8.4) This explains the separations that are seen between the main feature and the satellite features.

The processes resulting in the satellite feature in the sample spectrum, Figure 8.3(a), are the result of the presence of the $Cu^{(II)}$ state, but the very low intensity of these features indicate that the sample is primarily in the $Cu^{(I)}$ state. The CuO indicates that the intensity ratio of the main feature to the satellite feature is roughly 2:1 so the negligible amount of satellite content can also be seen in the main feature as the slight asymmetry (934.4 eV) seen in the main feature at 933.0 eV.

8.4 Conclusions

The analysis of the copper oxidation state in the compound, Methanobactin, by XPS shows the copper primarily in the $Cu^{(I)}$ state. The small satellite features existing in the spectra allowed for the determination. The other features seen in the analysis also show strong agreement with the published structure, indicating the presence of multiple functionalities. The advantages of XPS proved to be well suited for this study and the use of the satellite information and corresponding calculations aided in the analysis of the copper.

8.5 References

1. H.J Kim, D.W.Graham, A.A. DiSpirito, M.A. Alterman, N.Galeva, C.K. Larive, D.J. Asunskis, P.M.A. Sherwood. *Science* **305**, 1612 (2004).

2. S. Thomas, P.M.A. Sherwood, N.Singh, A. Al-Sarif, M.J. O'Shea. *Physical Review B.* **39**, 6640 (1989).

3. P.M.A.Sherwood. *Journal of Electron Spectroscopy*, **81**, 319-342, (1996).

4. N. Chanunpanich, A.Ulman, Y.M.Strzhemechny, S.A.Swarz, J.Dormicik, A.Janke, H.G.Braun, T. Kratzmuller. Polymeric International, **52**, 172-178 (2003).

5. H. Harker, P.M.A.Sherwood. Philosophical Magazine, **27**, 1241-1244 (1973).

6. A.A.Audi, P.M.A.Sherwood. *Surface and Interface Analysis*, **29**, 265-275 (2000).

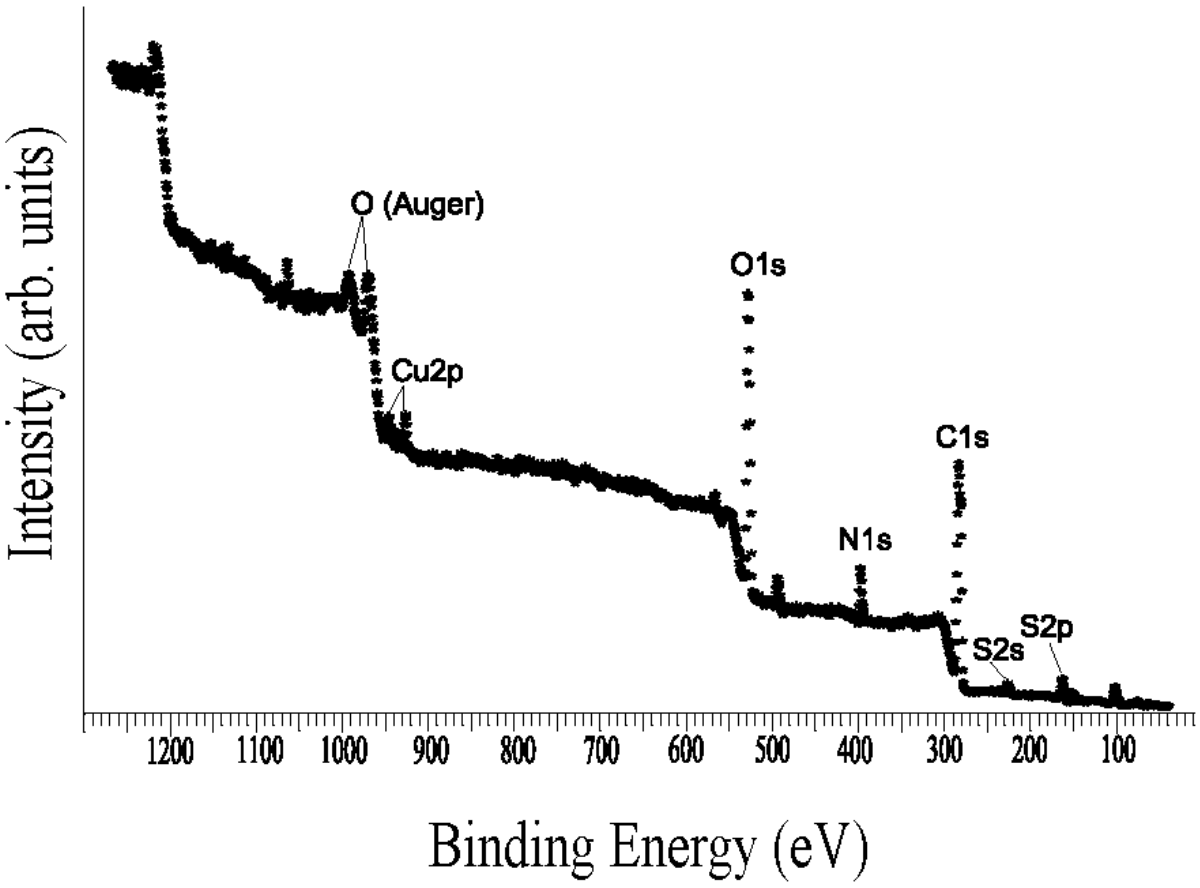

Figure 8.1 The survey scan of the copper-binding compound, methanobactin.

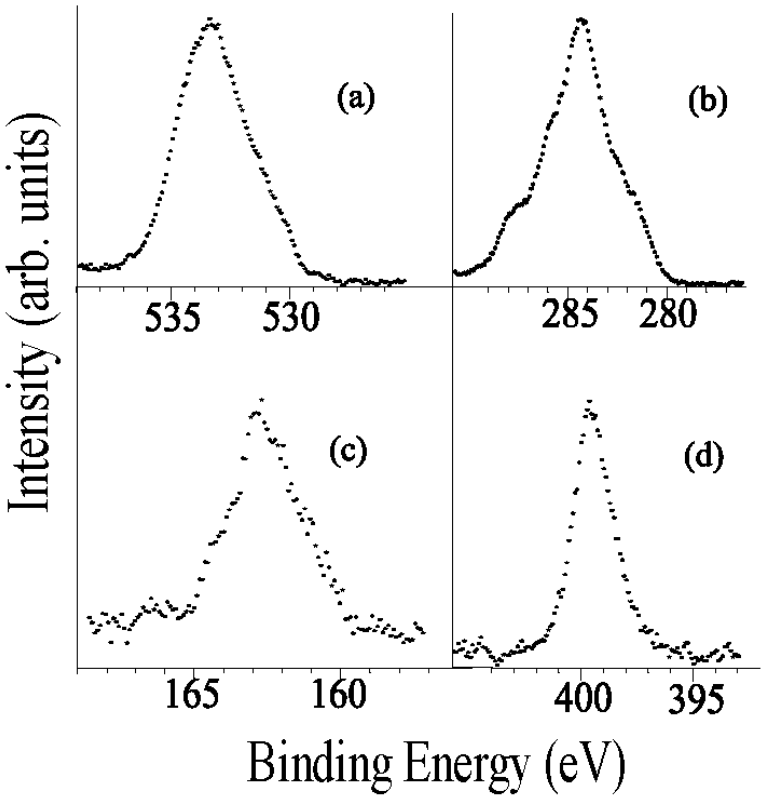

Figure 8.2 The core-level XPS results for the O1s (a), C1s (b), S2p (c) and N1s (d) regions.

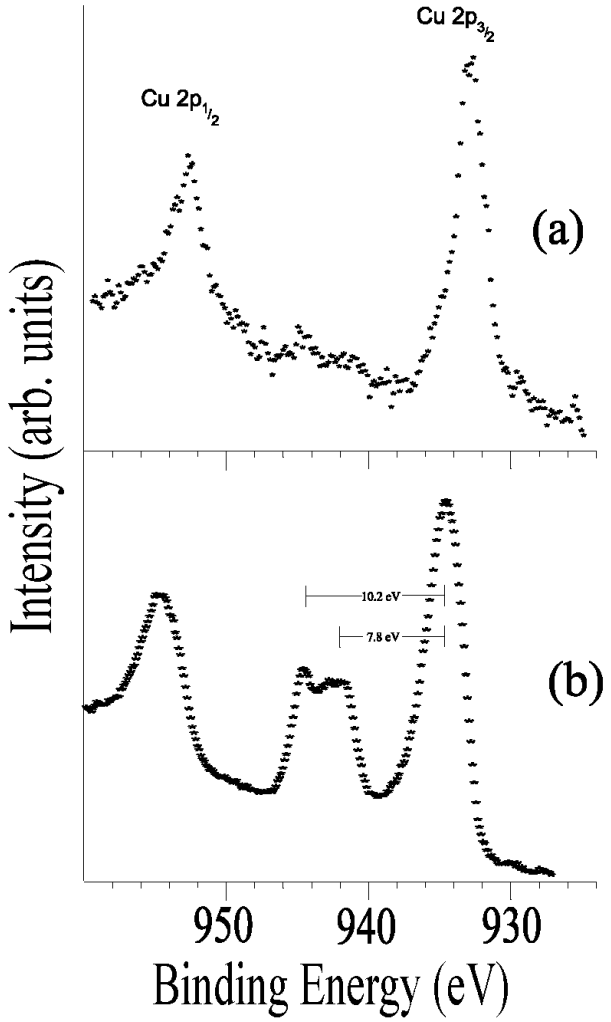

Figure 8.3 The Cu2p regions for the copper-binding compound (a) and CuO (b), exhibiting the satellite features.

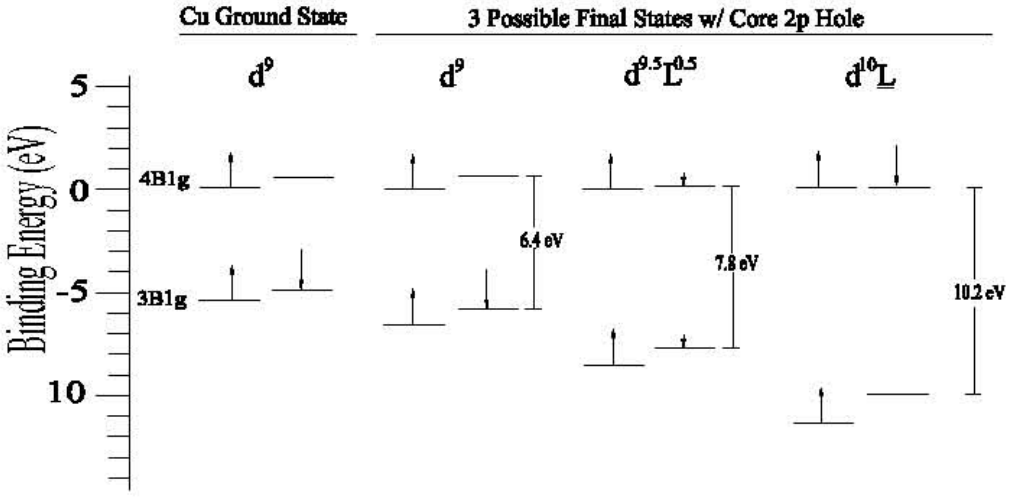

Figure 8.4 The changes in the 4B1g and 3B1g orbitals showing a potential charge-transfer process that can result in the satellite features.